

# A Study of Time-Dependent $CP$ -Violating Asymmetries and Flavor Oscillations in Neutral $B$ Decays at the $\Upsilon(4S)$

## The *BABAR* Collaboration

B. Aubert, D. Boutigny, J.-M. Gaillard, A. Hicheur, Y. Karyotakis, J. P. Lees, P. Robbe, and V. Tisserand  
*Laboratoire de Physique des Particules, F-74941 Annecy-le-Vieux, France*

A. Palano and A. Pompili  
*Università di Bari, Dipartimento di Fisica and INFN, I-70126 Bari, Italy*

G. P. Chen, J. C. Chen, N. D. Qi, G. Rong, P. Wang, and Y. S. Zhu  
*Institute of High Energy Physics, Beijing 100039, China*

G. Eigen and B. Stugu  
*University of Bergen, Inst. of Physics, N-5007 Bergen, Norway*

G. S. Abrams, A. W. Borgland, A. B. Breon, D. N. Brown, J. Button-Shafer, R. N. Cahn,  
A. R. Clark, M. S. Gill, A. V. Gritsan, Y. Groysman, R. G. Jacobsen, R. W. Kadel, J. Kadyk,  
L. T. Kerth, Yu. G. Kolomensky, J. F. Kral, C. LeClerc, M. E. Levi, G. Lynch, P. J. Oddone,  
M. Pripstein, N. A. Roe, A. Romosan, M. T. Ronan, V. G. Shelkov, A. V. Telnov, and W. A. Wenzel  
*Lawrence Berkeley National Laboratory and University of California, Berkeley, CA 94720, USA*

T. J. Harrison, C. M. Hawkes, D. J. Knowles, S. W. O'Neale, R. C. Penny, A. T. Watson, and N. K. Watson  
*University of Birmingham, Birmingham, B15 2TT, United Kingdom*

T. Deppermann, K. Goetzen, H. Koch, M. Kunze, B. Lewandowski, K. Peters, H. Schmuecker, and M. Steinke  
*Ruhr Universität Bochum, Institut für Experimentalphysik 1, D-44780 Bochum, Germany*

N. R. Barlow, W. Bhimji, N. Chevalier, P. J. Clark, W. N. Cottingham, B. Foster, C. Mackay, and F. F. Wilson  
*University of Bristol, Bristol BS8 1TL, United Kingdom*

K. Abe, C. Hearty, T. S. Mattison, J. A. McKenna, and D. Thiessen  
*University of British Columbia, Vancouver, BC, Canada V6T 1Z1*

S. Jolly and A. K. McKemey  
*Brunel University, Uxbridge, Middlesex UB8 3PH, United Kingdom*

V. E. Blinov, A. D. Bukin, D. A. Bukin, A. R. Buzykaev, V. B. Golubev, V. N. Ivanchenko, A. A. Korol,  
E. A. Kravchenko, A. P. Onuchin, S. I. Serednyakov, Yu. I. Skovpen, V. I. Telnov, and A. N. Yushkov  
*Budker Institute of Nuclear Physics, Novosibirsk 630090, Russia*

D. Best, M. Chao, D. Kirkby, A. J. Lankford, M. Mandelkern, S. McMahon, and D. P. Stoker  
*University of California at Irvine, Irvine, CA 92697, USA*

K. Arisaka, C. Buchanan, and S. Chun  
*University of California at Los Angeles, Los Angeles, CA 90024, USA*

D. B. MacFarlane, S. Prell, Sh. Rahatlou, G. Raven, and V. Sharma  
*University of California at San Diego, La Jolla, CA 92093, USA*

C. Campagnari, B. Dahmes, P. A. Hart, N. Kuznetsova, S. L. Levy,  
O. Long, A. Lu, M. A. Mazur, J. D. Richman, and W. Verkerke  
*University of California at Santa Barbara, Santa Barbara, CA 93106, USA*

J. Beringer, A. M. Eisner, M. Grothe, C. A. Heusch, W. S. Lockman, T. Pulliam, T. Schalk,  
R. E. Schmitz, B. A. Schumm, A. Seiden, M. Turri, W. Walkowiak, D. C. Williams, and M. G. Wilson  
*University of California at Santa Cruz, Institute for Particle Physics, Santa Cruz, CA 95064, USA*

E. Chen, G. P. Dubois-Felsmann, A. Dvoretiskii, D. G. Hitlin, S. Metzler,  
J. Oyang, F. C. Porter, A. Ryd, A. Samuel, M. Weaver, S. Yang, and R. Y. Zhu  
*California Institute of Technology, Pasadena, CA 91125, USA*

S. Devmal, T. L. Geld, S. Jayatilleke, G. Mancinelli, B. T. Meadows, and M. D. Sokoloff  
*University of Cincinnati, Cincinnati, OH 45221, USA*

T. Barillari, P. Bloom, M. O. Dima, W. T. Ford, U. Nauenberg,  
A. Olivas, P. Rankin, J. Roy, J. G. Smith, and W. C. van Hoek  
*University of Colorado, Boulder, CO 80309, USA*

J. Blouw, J. L. Harton, M. Krishnamurthy, A. Soffer, W. H. Toki, R. J. Wilson, and J. Zhang  
*Colorado State University, Fort Collins, CO 80523, USA*

T. Brandt, J. Brose, T. Colberg, M. Dickopp, R. S. Dubitzky, A. Hauke, E. Maly,  
R. Müller-Pfefferkorn, S. Otto, K. R. Schubert, R. Schwierz, B. Spaan, and L. Wilden  
*Technische Universität Dresden, Institut für Kern- und Teilchenphysik, D-01062 Dresden, Germany*

D. Bernard, G. R. Bonneaud, F. Brochard, J. Cohen-Tanugi,  
S. Ferrag, S. T'Jampens, Ch. Thiebaux, G. Vasileiadis, and M. Verderi  
*Ecole Polytechnique, F-91128 Palaiseau, France*

A. Anjomshoa, R. Bernet, A. Khan, D. Lavin, F. Muheim, S. Playfer, J. E. Swain, and J. Tinslay  
*University of Edinburgh, Edinburgh EH9 3JZ, United Kingdom*

M. Falbo  
*Elon University, Elon University, NC 27244-2010, USA*

C. Borean, C. Bozzi, and L. Piemontese  
*Università di Ferrara, Dipartimento di Fisica and INFN, I-44100 Ferrara, Italy*

E. Treadwell  
*Florida A&M University, Tallahassee, FL 32307, USA*

F. Anulli,\* R. Baldini-Ferrolì, A. Calcaterra, R. de Sangro, D. Falciari,  
G. Finocchiaro, P. Patteri, I. M. Peruzzi,\* M. Piccolo, Y. Xie, and A. Zallo  
*Laboratori Nazionali di Frascati dell'INFN, I-00044 Frascati, Italy*

S. Bagnasco, A. Buzzo, R. Contri, G. Crosetti, M. Lo Vetere, M. Macri, M. R. Monge,  
S. Passaggio, F. C. Pastore, C. Patrignani, M. G. Pia, E. Robutti, A. Santroni, and S. Tosi  
*Università di Genova, Dipartimento di Fisica and INFN, I-16146 Genova, Italy*

M. Morii  
*Harvard University, Cambridge, MA 02138, USA*

R. Bartoldus, R. Hamilton, and U. Mallik  
*University of Iowa, Iowa City, IA 52242, USA*

J. Cochran, H. B. Crawley, P.-A. Fischer, J. Lamsa, W. T. Meyer, and E. I. Rosenberg

*Iowa State University, Ames, IA 50011-3160, USA*

G. Grosdidier, C. Hast, A. Höcker, H. M. Lacker, S. Laplace, V. Lepeltier,  
A. M. Lutz, S. Plaszczynski, M. H. Schune, S. Trincaz-Duvoid, and G. Wormser  
*Laboratoire de l'Accélérateur Linéaire, F-91898 Orsay, France*

R. M. Bionta, V. Brigljević, D. J. Lange, M. Mugge, K. van Bibber, and D. M. Wright  
*Lawrence Livermore National Laboratory, Livermore, CA 94550, USA*

A. J. Bevan, J. R. Fry, E. Gabathuler, R. Gamet, M. George, M. Kay, D. J. Payne, R. J. Sloane, and C. Touramanis  
*University of Liverpool, Liverpool L69 3BX, United Kingdom*

M. L. Aspinwall, D. A. Bowerman, P. D. Dauncey, U. Egede, I. Eschrich,  
N. J. W. Gunawardane, J. A. Nash, P. Sanders, and D. Smith  
*University of London, Imperial College, London, SW7 2BW, United Kingdom*

D. E. Azzopardi, J. J. Back, G. Bellodi, P. Dixon, P. F. Harrison,  
R. J. L. Potter, H. W. Shorthouse, P. Strother, and P. B. Vidal  
*Queen Mary, University of London, E1 4NS, United Kingdom*

G. Cowan, S. George, M. G. Green, A. Kurup, C. E. Marker,  
P. McGrath, T. R. McMahon, S. Ricciardi, F. Salvatore, and G. Vaitsas  
*University of London, Royal Holloway and Bedford New College, Egham, Surrey TW20 0EX, United Kingdom*

D. Brown and C. L. Davis  
*University of Louisville, Louisville, KY 40292, USA*

J. Allison, R. J. Barlow, J. T. Boyd, A. C. Forti, J. Fullwood, F. Jackson,  
G. D. Lafferty, N. Savvas, J. H. Weatherall, and J. C. Williams  
*University of Manchester, Manchester M13 9PL, United Kingdom*

A. Farbin, A. Jawahery, V. Lillard, J. Olsen, D. A. Roberts, and J. R. Schieck  
*University of Maryland, College Park, MD 20742, USA*

G. Blaylock, C. Dallapiccola, K. T. Flood, S. S. Hertzbach,  
R. Kofler, V. B. Koptchev, T. B. Moore, H. Staengle, and S. Willocq  
*University of Massachusetts, Amherst, MA 01003, USA*

B. Brau, R. Cowan, G. Sciolla, F. Taylor, and R. K. Yamamoto  
*Massachusetts Institute of Technology, Laboratory for Nuclear Science, Cambridge, MA 02139, USA*

M. Milek and P. M. Patel  
*McGill University, Montréal, QC, Canada H3A 2T8*

F. Palombo  
*Università di Milano, Dipartimento di Fisica and INFN, I-20133 Milano, Italy*

J. M. Bauer, L. Cremaldi, V. Eschenburg, R. Kroeger, J. Reidy, D. A. Sanders, and D. J. Summers  
*University of Mississippi, University, MS 38677, USA*

J. Y. Nief and P. Taras  
*Université de Montréal, Laboratoire René J. A. Lévesque, Montréal, QC, Canada H3C 3J7*

H. Nicholson  
*Mount Holyoke College, South Hadley, MA 01075, USA*

C. Cartaro, N. Cavallo,<sup>†</sup> G. De Nardo, F. Fabozzi, C. Gatto, L. Lista, P. Paolucci, D. Piccolo, and C. Sciacca  
*Università di Napoli Federico II, Dipartimento di Scienze Fisiche and INFN, I-80126, Napoli, Italy*

J. M. LoSecco  
*University of Notre Dame, Notre Dame, IN 46556, USA*

J. R. G. Alsmiller and T. A. Gabriel  
*Oak Ridge National Laboratory, Oak Ridge, TN 37831, USA*

J. Brau, R. Frey, E. Grauges, M. Iwasaki, N. B. Sinev, and D. Strom  
*University of Oregon, Eugene, OR 97403, USA*

F. Colecchia, F. Dal Corso, A. Dorigo, F. Galeazzi, M. Margoni, G. Michelon,  
 M. Morandin, M. Posocco, M. Rotondo, F. Simonetto, R. Stroili, E. Torassa, and C. Voci  
*Università di Padova, Dipartimento di Fisica and INFN, I-35131 Padova, Italy*

M. Benayoun, H. Briand, J. Chauveau, P. David, Ch. de la Vaissière, L. Del  
 Buono, O. Hamon, F. Le Diberder, Ph. Leruste, J. Ocariz, L. Roos, and J. Stark  
*Universités Paris VI et VII, Lab de Physique Nucléaire H. E., F-75252 Paris, France*

P. F. Manfredi, V. Re, and V. Speziali  
*Università di Pavia, Dipartimento di Elettronica and INFN, I-27100 Pavia, Italy*

E. D. Frank, L. Gladney, Q. H. Guo, and J. Panetta  
*University of Pennsylvania, Philadelphia, PA 19104, USA*

C. Angelini, G. Batignani, S. Bettarini, M. Bondioli, F. Bucci, E. Campagna, M. Carpinelli,  
 F. Forti, M. A. Giorgi, A. Lusiani, G. Marchiori, F. Martinez-Vidal, M. Morganti, N. Neri,  
 E. Paoloni, M. Rama, G. Rizzo, F. Sandrelli, G. Simi, G. Triggiani, and J. Walsh  
*Università di Pisa, Scuola Normale Superiore and INFN, I-56010 Pisa, Italy*

M. Haire, D. Judd, K. Paick, L. Turnbull, and D. E. Wagoner  
*Prairie View A&M University, Prairie View, TX 77446, USA*

J. Albert, P. Elmer, C. Lu, V. Miftakov, S. F. Schaffner, A. J. S. Smith, A. Tumanov, and E. W. Varnes  
*Princeton University, Princeton, NJ 08544, USA*

G. Cavoto, D. del Re, F. Ferrarotto, F. Ferroni, E. Lamanna, M. A. Mazzoni,  
 S. Morganti, G. Piredda, F. Safai Tehrani, M. Serra, and C. Voena  
*Università di Roma La Sapienza, Dipartimento di Fisica and INFN, I-00185 Roma, Italy*

R. Faccini  
*University of California at San Diego, La Jolla, CA 92093, USA and*  
*Università di Roma La Sapienza, Dipartimento di Fisica and INFN, I-00185 Roma, Italy*

S. Christ and R. Waldi  
*Universität Rostock, D-18051 Rostock, Germany*

T. Adye, N. De Groot, B. Franek, N. I. Geddes, G. P. Gopal, and S. M. Xella  
*Rutherford Appleton Laboratory, Chilton, Didcot, Oxon, OX11 0QX, United Kingdom*

R. Aleksan, S. Emery, A. Gaidot, S. F. Ganzhur, P.-F. Giraud, G. Hamel de Monchenault,  
 W. Kozanecki, M. Langer, G. W. London, B. Mayer, B. Serfass, G. Vasseur, Ch. Yèche, and M. Zito  
*DAPNIA, Commissariat à l'Energie Atomique/Saclay, F-91191 Gif-sur-Yvette, France*

M. V. Purohit, H. Singh, A. W. Weidemann, and F. X. Yumiceva  
*University of South Carolina, Columbia, SC 29208, USA*

I. Adam, D. Aston, N. Berger, A. M. Boyarski, G. Calderini, M. R. Convery, D. P. Coupal, D. Dong, J. Dorfan,  
 W. Dunwoodie, R. C. Field, T. Glanzman, S. J. Gowdy, T. Haas, V. Halyo, T. Himel, T. Hryn'ova, M. E. Huffer,

W. R. Innes, C. P. Jessop, M. H. Kelsey, P. Kim, M. L. Kocian, U. Langenegger, D. W. G. S. Leith, S. Luitz, V. Luth, H. L. Lynch, H. Marsiske, S. Menke, R. Messner, D. R. Muller, C. P. O'Grady, V. E. Ozcan, A. Perazzo, M. Perl, S. Petrak, H. Quinn, B. N. Ratcliff, S. H. Robertson, A. Roodman, A. A. Salnikov, T. Schietinger, R. H. Schindler, J. Schwiening, A. Snyder, A. Soha, S. M. Spanier, J. Stelzer, D. Su, M. K. Sullivan, H. A. Tanaka, J. Va'vra, S. R. Wagner, A. J. R. Weinstein, W. J. Wisniewski, D. H. Wright, and C. C. Young  
*Stanford Linear Accelerator Center, Stanford, CA 94309, USA*

P. R. Burchat, C. H. Cheng, T. I. Meyer, and C. Roat  
*Stanford University, Stanford, CA 94305-4060, USA*

R. Henderson  
*TRIUMF, Vancouver, BC, Canada V6T 2A3*

W. Bugg and H. Cohn  
*University of Tennessee, Knoxville, TN 37996, USA*

J. M. Izen, I. Kitayama, and X. C. Lou  
*University of Texas at Dallas, Richardson, TX 75083, USA*

F. Bianchi, M. Bona, and D. Gamba  
*Università di Torino, Dipartimento di Fisica Sperimentale and INFN, I-10125 Torino, Italy*

L. Bosisio, G. Della Ricca, S. Dittongo, L. Lanceri, P. Poropat, and G. Vuagnin  
*Università di Trieste, Dipartimento di Fisica and INFN, I-34127 Trieste, Italy*

R. S. Panvini  
*Vanderbilt University, Nashville, TN 37235, USA*

C. M. Brown, P. D. Jackson, R. Kowalewski, and J. M. Roney  
*University of Victoria, Victoria, BC, Canada V8W 3P6*

H. R. Band, E. Charles, S. Dasu, A. M. Eichenbaum, H. Hu, J. R. Johnson, R. Liu, F. Di Lodovico, Y. Pan, R. Prepost, I. J. Scott, S. J. Sekula, J. H. von Wimmersperg-Toeller, S. L. Wu, and Z. Yu  
*University of Wisconsin, Madison, WI 53706, USA*

T. M. B. Kordich and H. Neal  
*Yale University, New Haven, CT 06511, USA*

(Dated: February 7, 2008)

We present a measurement of time-dependent  $CP$ -violating asymmetries in neutral  $B$  meson decays collected with the  $BABAR$  detector at the PEP-II asymmetric-energy  $B$  Factory at the Stanford Linear Accelerator Center. The data sample consists of  $29.7 \text{ fb}^{-1}$  recorded at the  $\Upsilon(4S)$  resonance and  $3.9 \text{ fb}^{-1}$  off-resonance. One of the neutral  $B$  mesons, which are produced in pairs at the  $\Upsilon(4S)$ , is fully reconstructed in the  $CP$  decay modes  $J/\psi K_S^0$ ,  $\psi(2S)K_S^0$ ,  $\chi_{c1}K_S^0$ ,  $J/\psi K^{*0}$  ( $K^{*0} \rightarrow K_S^0\pi^0$ ) and  $J/\psi K_L^0$ , or in flavor-eigenstate modes involving  $D^{(*)}\pi/\rho/a_1$  and  $J/\psi K^{*0}$  ( $K^{*0} \rightarrow K^+\pi^-$ ). The flavor of the other neutral  $B$  meson is tagged at the time of its decay, mainly with the charge of identified leptons and kaons. A neural network tagging algorithm is used to recover events without a clear lepton or kaon tag. The proper time elapsed between the decays is determined by measuring the distance between the decay vertices. Wrong-tag probabilities, the time-difference resolution function, and the  $B^0$ - $\bar{B}^0$  oscillation frequency  $\Delta m_d$  are measured with a sample of about 6350 fully-reconstructed  $B^0$  decays in hadronic flavor-eigenstate modes. A maximum-likelihood fit to this flavor eigenstate sample finds  $\Delta m_d = 0.516 \pm 0.016$  (stat)  $\pm 0.010$  (syst)  $\text{ps}^{-1}$ . The value of the asymmetry amplitude  $\sin 2\beta$  is determined from a simultaneous maximum-likelihood fit to the time-difference distribution of the flavor-eigenstate sample and about 642 tagged  $B^0$  decays in the  $CP$ -eigenstate modes. We find  $\sin 2\beta = 0.59 \pm 0.14$  (stat)  $\pm 0.05$  (syst), demonstrating that  $CP$  violation exists in the neutral  $B$  meson system. We also determine the value of the  $CP$  violation parameter  $|\lambda| = 0.93 \pm 0.09$  (stat)  $\pm 0.03$  (syst), which is consistent with the expectation of  $|\lambda| = 1$  for no direct  $CP$  violation.

PACS numbers: 13.25.Hw, 12.15.Hh, 11.30.Er

## I. INTRODUCTION

$CP$  violation has been a central concern of particle physics since its discovery in 1964 [1]. Interest was heightened by Sakharov's observation [2] in 1967 that without  $CP$  violation, a universe that began as matter–anti-matter symmetric could not have evolved into the asymmetric one we now see. An elegant explanation of the  $CP$ -violating effects in  $K_L^0$  decays is provided by the  $CP$ -violating phase of the three-generation Cabibbo-Kobayashi-Maskawa (CKM) quark-mixing matrix [3]. However, existing studies of  $CP$  violation in neutral kaon decays and the resulting experimental constraints on the parameters of the CKM matrix [4] do not provide a stringent test of whether the CKM phase describes  $CP$  violation [5]. Moreover, the Standard Model does not, through the CKM phase, incorporate enough  $CP$  violation to explain the current matter–anti-matter asymmetry [6]. Understanding  $CP$  violation thus remains a pressing challenge.

An excellent testing ground for  $CP$  violation is provided by  $B$  mesons through particle–anti-particle mixing. A particle that is purely  $B^0$  at time  $t = 0$  will oscillate between that state and  $\bar{B}^0$  with a frequency  $\Delta m_d$ , the difference between the masses of the two neutral  $B$  mass eigenstates. If decays to a  $CP$  eigenstate  $f$  are observed, any difference between the rates when starting with a  $B^0$  or with a  $\bar{B}^0$  is a manifestation of  $CP$  violation. In some circumstances, including those in the experiment described here, the fundamental parameters of  $CP$  violation in the CKM model can be measured from such time-dependent rate asymmetries, unobscured by strong interactions. For example, a state initially produced as a  $B^0$  ( $\bar{B}^0$ ) can decay to  $J/\psi K_s^0$  directly or can oscillate into a  $\bar{B}^0$  ( $B^0$ ) and then decay to  $J/\psi K_s^0$ . With little theoretical uncertainty in the Standard Model, the phase difference between these amplitudes is equal to twice the angle  $\beta = \arg[-V_{cd}V_{cb}^*/V_{td}V_{tb}^*]$  of the Unitarity Triangle. The  $CP$ -violating asymmetry can thus provide a crucial test of the Standard Model.

The unitarity of the three-generation CKM matrix can be expressed in geometric form by six triangles of equal area in the complex plane. A nonzero area [7] directly implies the existence of a  $CP$ -violating CKM phase. The most experimentally accessible of the unitarity relations, involving the two smallest elements of the CKM matrix,  $V_{ub}$  and  $V_{td}$ , has come to be known as the Unitarity Triangle. Because the lengths of the sides of the Unitarity Triangle are comparable, the angles can be large, leading to potentially large  $CP$ -violating asymmetries from relative phases between CKM matrix elements.

In  $e^+e^-$  storage rings operating at the  $\Upsilon(4S)$  resonance, a  $B^0\bar{B}^0$  pair produced in an  $\Upsilon(4S)$  decay evolves

in a coherent  $P$ -wave state. If one of the  $B$  mesons, referred to as  $B_{\text{tag}}$ , can be ascertained to decay to a state of known flavor, *i.e.*  $B^0$  or  $\bar{B}^0$ , at a certain time  $t_{\text{tag}}$ , the other  $B$ , referred to as  $B_{\text{rec}}$ , at that time must be of the opposite flavor as a consequence of Bose symmetry. Consequently, the oscillatory probabilities for observing  $B^0\bar{B}^0$ ,  $B^0B^0$  and  $\bar{B}^0\bar{B}^0$  pairs produced in  $\Upsilon(4S)$  decays are a function of  $\Delta t = t_{\text{rec}} - t_{\text{tag}}$ , allowing mixing frequencies and  $CP$  asymmetries to be determined if  $\Delta t$  is known. The charges of identified leptons and kaons are the primary indicators of the flavor of the tagging  $B$ , but other particles also carry flavor information that can be exploited with a neural network algorithm. The reconstructed neutral  $B$  is found either in a flavor eigenstate ( $B_{\text{rec}} = B_{\text{flav}}$ ) or a  $CP$  mode ( $B_{\text{rec}} = B_{CP}$ ) by full reconstruction of its observed long-lived daughters.

At the PEP-II asymmetric  $e^+e^-$  collider [8], resonant production of the  $\Upsilon(4S)$  provides a copious source of  $B^0\bar{B}^0$  pairs moving along the beam axis ( $z$  direction) with an average Lorentz boost of  $\langle\beta\gamma\rangle = 0.55$ . Therefore, the proper decay-time difference  $\Delta t$  is, to an excellent approximation, proportional to the distance  $\Delta z$  between the two  $B^0$ -decay vertices along the axis of the boost,  $\Delta t \approx \Delta z/c\langle\beta\gamma\rangle$ . The average separation between the two  $B$  decay vertices is  $\Delta z = \langle\beta\gamma\rangle c\tau_B = 260 \mu\text{m}$ , while the RMS  $\Delta z$  resolution of the detector is about  $180 \mu\text{m}$ .

### A. Measurement of $B^0$ flavor oscillations

The phenomenon of particle–anti-particle mixing in the neutral  $B$  meson system was first observed almost fifteen years ago [9, 10]. The oscillation frequency in  $B^0$ – $\bar{B}^0$  mixing has been extensively studied with both time-integrated and time-dependent techniques [11]. By interchanging  $\bar{b}d$  with  $\bar{b}d$ ,  $B^0$ – $\bar{B}^0$  mixing changes the additive bottom quantum number by two units, *i.e.*,  $|\Delta B| = 2$ . In the Standard Model, such a process is the result of ordinary  $|\Delta B| = 1$  weak interactions in second order involving the exchange of charge-2/3 quarks, with the top quark contributing the dominant amplitude. A measurement of  $\Delta m_d$  is therefore sensitive to the value of the CKM matrix element  $V_{td}$ . At present the sensitivity to  $V_{td}$  is not limited by experimental precision on  $\Delta m_d$ , but by theoretical uncertainties in the calculation, in particular the quantity  $f_B^2 B_B$ , where  $f_B$  is the  $B^0$  decay constant, and  $B_B$  is the so-called bag factor, representing the  $\Delta B = 2$  strong-interaction matrix element. There may also be contributions from interactions outside the Standard Model

Beyond these questions of fundamental interest, since the measurement of  $\Delta m_d$  incorporates all elements of the analysis for time-dependent  $CP$  asymmetries, including  $B$  reconstruction, tagging, and  $\Delta t$  determination and resolution, it is an essential test of our understanding of these aspects of the  $\sin 2\beta$  measurement.

For the measurement of  $\Delta m_d$ , one neutral  $B$  ( $B_{\text{flav}}$ ) is fully reconstructed in a flavor eigenstate [12] as

\*Also with Università di Perugia, Perugia, Italy

†Also with Università della Basilicata, Potenza, Italy

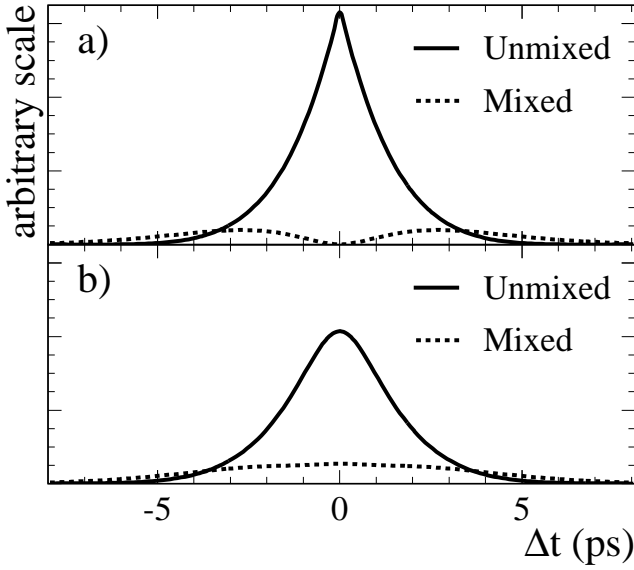


FIG. 1: Expected  $\Delta t$  distribution for mixed and unmixed events a) with perfect tagging and  $\Delta t$  resolution, and b) with typical mistag rates and  $\Delta t$  resolution.

$D^{(*)-\pi^+/\rho^+/a_1^+$  or  $J/\psi K^{*0}$  ( $K^{*0} \rightarrow K^+\pi^-$ ), while the second is tagged by its decay products. The probability for  $B^0\text{-}\bar{B}^0$  mixing is a function of  $\Delta m_d$  and the proper time difference  $\Delta t$  between the two  $B$  decays:

$$\text{Prob}(B^0\bar{B}^0 \rightarrow B^0B^0 \text{ or } \bar{B}^0\bar{B}^0, B^0\bar{B}^0) = \frac{\Gamma}{4} e^{-\Gamma|\Delta t|} (1 \mp \cos \Delta m_d \Delta t), \quad (1)$$

where  $\tau_{B^0} = 1/\Gamma$  is the  $B^0$  lifetime. The observed  $B^0\bar{B}^0$  system produced in an  $\Upsilon(4S)$  decay can be classified as *mixed* or *unmixed* depending on whether the reconstructed flavor-eigenstate  $B_{\text{rec}} = B_{\text{flav}}$  has the same or

the opposite flavor as the tagging  $B = B_{\text{tag}}$ . If the  $\Delta t$  resolution and flavor tagging were perfect, the asymmetry as a function of  $\Delta t$

$$A_{\text{mixing}}(\Delta t) = \frac{N_{\text{unmix}}(\Delta t) - N_{\text{mix}}(\Delta t)}{N_{\text{unmix}}(\Delta t) + N_{\text{mix}}(\Delta t)} \quad (2)$$

would describe a cosine function with unit amplitude. The asymmetry goes through zero near 2.1  $B^0$  proper lifetimes and the sensitivity to  $\Delta m_d$ , which is proportional to  $\Delta t^2 e^{-\Gamma|\Delta t|} \sin^2 \Delta m_d \Delta t$ , reaches a maximum in this region. If the tagging algorithm incorrectly identifies the tag with a probability  $w$ , the amplitude of the oscillation is reduced by a dilution factor  $\mathcal{D} = (1 - 2w)$ . When more than one type of flavor tag is used, each has its own mistag rate  $w_i$ .

Neglecting any background contributions, the probability density functions (PDFs) for the mixed ( $-$ ) and unmixed ( $+$ ) events,  $\mathcal{H}_{\pm}$ , can be expressed as the convolution of the underlying oscillatory physics distribution

$$h_{\pm}(\Delta t; \Gamma, \Delta m_d, w) = \frac{\Gamma}{4} e^{-\Gamma|\Delta t|} [1 \pm \mathcal{D} \cos \Delta m_d \Delta t] \quad (3)$$

with a time-difference resolution function  $\mathcal{R}(\delta_t = \Delta t - \Delta t_{\text{true}}; \hat{a})$  to give

$$\mathcal{H}_{\pm}(\Delta t; \Gamma, \Delta m_d, w, \hat{a}) = h_{\pm}(\Delta t_{\text{true}}; \Gamma, \Delta m_d, w) \otimes \mathcal{R}(\delta_t; \hat{a}), \quad (4)$$

where  $\Delta t$  and  $\Delta t_{\text{true}}$  are the measured and the true time differences, and  $\hat{a}$  are parameters of the resolution function. Figure 1 illustrates the impact of typical mistag and  $\Delta t$  resolution effects on the  $\Delta t$  distributions for mixed and unmixed events.

A full likelihood function is then constructed by summing  $\mathcal{H}_{\pm}$  over all mixed and unmixed events in a given uniquely-assigned tagging category  $i$  and over all tagging categories

$$\ln \mathcal{L}_{\text{mix}} = \sum_i^{\text{tagging}} \left[ \sum_{\text{unmixed}} \ln \mathcal{H}_+(\Delta t; \Gamma, \Delta m_d, w_i, \hat{a}_i) + \sum_{\text{mixed}} \ln \mathcal{H}_-(\Delta t; \Gamma, \Delta m_d, w_i, \hat{a}_i) \right]. \quad (5)$$

This can be maximized to extract the mistag fractions  $w_i$  and resolution parameters  $\hat{a}_i$  and, simultaneously, the mixing rate  $\Delta m_d$ . The correlation between  $w_i$  and  $\Delta m_d$  is small, because the rate of mixed events near  $\Delta t = 0$ , where the  $B^0\text{-}\bar{B}^0$  mixing probability is small, is principally governed by the mistag rate. Conversely, the sensitivity to  $\Delta m_d$  increases at larger values of  $\Delta t$ ; when  $\Delta t$  is approximately twice the  $B$  lifetime, half of the neutral  $B$  mesons will have oscillated.

## B. Measurement of $CP$ asymmetries

For the measurement of  $CP$  asymmetries, one  $B$  ( $B_{CP}$ ) is fully reconstructed in a  $CP$  eigenstate with eigenvalue  $\eta_{CP} = -1$  ( $J/\psi K_S^0$ ,  $\psi(2S)K_S^0$ , or  $\chi_{c1}K_S^0$ ) or  $+1$  ( $J/\psi K_L^0$ ), while the second is tagged with its decay products just as for the mixing measurement. The  $B_{CP}$  sample is further enlarged by including the mode  $J/\psi K^{*0}$  ( $K^{*0} \rightarrow K_S^0 \pi^0$ ). However, due to the presence of even ( $L = 0, 2$ ) and odd

( $L = 1$ ) orbital angular momenta in the  $J/\psi K^{*0}$  system, there are  $\eta_{CP} = +1$  and  $-1$  contributions to its decay rate, respectively. When the angular information in the decay is ignored, the measured  $CP$  asymmetry in  $J/\psi K^{*0}$  is reduced by a dilution factor  $D_{\perp} = 1 - 2R_{\perp}$ , where  $R_{\perp}$  is the fraction of the  $L = 1$  component. We have measured  $R_{\perp} = 0.160 \pm 0.032 \pm 0.014$  [13] which, after acceptance corrections, leads to an effective  $\eta_{CP} = +0.65 \pm 0.07$  for the  $J/\psi K^{*0}$  mode.

The expected time evolution for the tagged  $B_{CP}$  sample depends both on  $B^0$ - $\bar{B}^0$  mixing and on the decay amplitudes of  $B^0$  and  $\bar{B}^0$  to the final state  $f$  through a single complex parameter  $\lambda$ . Mixing generates a lifetime difference as well as a mass difference between the two neutral  $B$  meson mass eigenstates, but the lifetime difference is expected to be small since it is a consequence of common

final states in  $B^0$  and  $\bar{B}^0$  decays. Such common states, which include the  $CP$  eigenstates studies here, make up a very small fraction of the decay width because they are quite suppressed by CKM matrix elements. Dropping these, and thus ignoring any lifetime difference, results in a simple expression for  $\lambda$  in terms of the  $|\Delta B = 1|$  and  $|\Delta B = 2|$  interactions,

$$\lambda = - \frac{|\langle B^0 | \mathcal{H}_{\Delta B=2} | \bar{B}^0 \rangle|}{\langle B^0 | \mathcal{H}_{\Delta B=2} | B^0 \rangle} \frac{\langle f | \mathcal{H}_{\Delta B=1} | \bar{B}^0 \rangle}{\langle f | \mathcal{H}_{\Delta B=1} | B^0 \rangle}. \quad (6)$$

Redefining the states for  $B^0$  and  $\bar{B}^0$  by multiplying them by two different phases has no effect on  $\lambda$ , which is thus phase-convention independent, as every physical observable must be. The decay distributions are

$$f_{\pm}(\Delta t) = \frac{\Gamma}{4} e^{-\Gamma|\Delta t|} \left\{ 1 \pm \mathcal{D} \left[ \frac{2Im\lambda}{1+|\lambda|^2} \sin \Delta m_d \Delta t - \frac{1-|\lambda|^2}{1+|\lambda|^2} \cos \Delta m_d \Delta t \right] \right\}, \quad (7)$$

where the  $+$  or  $-$  sign indicates whether the  $B_{\text{tag}}$  is tagged as a  $B^0$  or a  $\bar{B}^0$ , respectively. The dilution factor  $\mathcal{D} = 1 - 2w$  accounts for the probability  $w$  that the flavor of the tagging  $B$  is identified incorrectly.

The distributions are much simpler when  $|\lambda| = 1$ , which is the expectation of the Standard Model for decays like  $B^0 \rightarrow J/\psi K_S^0$ . If all the mechanisms that contribute to the decay have the same weak phase then the ratio of the weak decay amplitudes in Eq. 6 is just  $\eta_{CP} e^{2i\phi_{\text{dec}}}$ , where  $\phi_{\text{dec}}$  is the weak phase for  $\bar{B}^0 \rightarrow f$ ;  $\phi_{\text{dec}}$  is convention dependent and unobservable. The remaining factor introduces a phase due to  $B^0$ - $\bar{B}^0$  mixing. The combination of these phases is convention independent and observable.

For decays such as  $B^0 \rightarrow J/\psi K_S^0$ , or more generally  $(c\bar{c})K_S^0$  and  $(c\bar{c})K_L^0$ , an explicit representation for  $\lambda$  can be found from the ratio of the amplitude for  $\bar{B}^0 \rightarrow (c\bar{c})\bar{K}^0$  to the interfering process  $\bar{B}^0 \rightarrow B^0 \rightarrow (c\bar{c})K^0 \rightarrow (c\bar{c})\bar{K}^0$ . The decay  $B^0 \rightarrow (c\bar{c})K^0$  involves a  $\bar{b} \rightarrow \bar{c}c\bar{s}$  transition with an amplitude proportional to  $[V_{cb}^* V_{cs}]$ , while  $\bar{B}^0 \rightarrow (c\bar{c})\bar{K}^0$  provides analogously a factor  $\eta_{CP} [V_{cb} V_{cs}^*]$ . Because  $\bar{B}^0 \rightarrow B^0$  mixing is dominated by the loop diagram with a  $t$  quark, it introduces a factor  $[V_{td}^* V_{tb} / V_{td} V_{tb}^*]$ , while  $K^0 \rightarrow \bar{K}^0$  mixing, being dominated by the  $c$ -quark loop, adds a factor  $[V_{cd} V_{cs}^* / V_{cd}^* V_{cs}]$ . Altogether, for transitions of the type  $b \rightarrow \bar{c}\bar{s}$ ,

$$\begin{aligned} \lambda &= \eta_{CP} \left( \frac{V_{td} V_{tb}^*}{V_{td}^* V_{tb}} \right) \left( \frac{V_{cb} V_{cs}^*}{V_{cb}^* V_{cs}} \right) \left( \frac{V_{cd}^* V_{cs}}{V_{cd} V_{cs}^*} \right) \\ &= \eta_{CP} \left( \frac{V_{cb} V_{cd}^*}{V_{tb} V_{td}^*} \right) \left( \frac{V_{tb}^* V_{td}}{V_{cb}^* V_{cd}} \right) \\ &= \eta_{CP} e^{-2i\beta}. \end{aligned} \quad (8)$$

The time-dependent rate for decay of the  $B_{CP}$  final state is then given by

$$f_{\pm}(\Delta t; \Gamma, \Delta m_d, w, \sin 2\beta) = \frac{\Gamma}{4} e^{-\Gamma|\Delta t|} [1 \mp \eta_{CP} \mathcal{D} \sin 2\beta \sin \Delta m_d \Delta t]. \quad (9)$$

In the limit of perfect determination of the flavor of the fully-reconstructed  $B$  in the  $B_{\text{flav}}$  sample, which we assume throughout, the dilution here and in the mixed and unmixed amplitudes of Eq. 3 arise solely from the  $B_{\text{tag}}$  side, allowing the values of the mistag fractions  $w_i$  to be determined by studying the time-dependent rate of  $B^0$ - $\bar{B}^0$  oscillations.

To account for the finite resolution of the detector, the time-dependent distributions  $f_{\pm}$  for  $B^0$  and  $\bar{B}^0$  tagged events (Eq. 9) must be convolved with a time resolution function  $\mathcal{R}(\delta_t = \Delta t - \Delta t_{\text{true}}; \hat{a})$  as described above for mixing,

$$\mathcal{F}_{\pm}(\Delta t; \Gamma, \Delta m_d, w, \sin 2\beta, \hat{a}) = f_{\pm}(\Delta t_{\text{true}}; \Gamma, \Delta m_d, w, \sin 2\beta) \otimes \mathcal{R}(\delta_t; \hat{a}), \quad (10)$$

where  $\hat{a}$  represents the set of parameters that describe the resolution function. In practice, events are separated into the same tagging categories as in mixing, each of which has a different mistag fraction  $w_i$ , determined individually for each category. Figure 2 illustrates the impact of typical mistag and  $\Delta t$  resolution effects on the  $\Delta t$  distributions for  $B^0$ - and  $\bar{B}^0$ -tagged  $CP$  events.

It is possible to construct a  $CP$ -violating observable

$$\mathcal{A}_{CP}(\Delta t) = \frac{\mathcal{F}_+(\Delta t) - \mathcal{F}_-(\Delta t)}{\mathcal{F}_+(\Delta t) + \mathcal{F}_-(\Delta t)}, \quad (11)$$



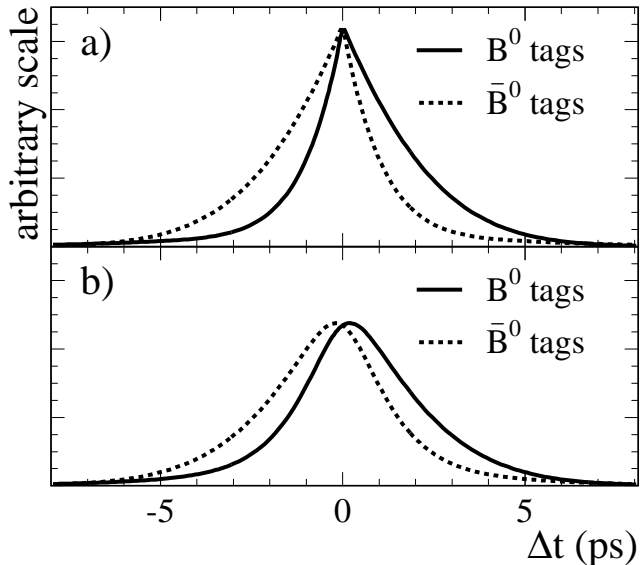


FIG. 2: Expected  $\Delta t$  distribution for  $B^0$ - and  $\bar{B}^0$ -tagged  $CP$  events a) with perfect tagging and  $\Delta t$  resolution, and b) with typical mistag rates and  $\Delta t$  resolution.

$$\ln \mathcal{L}_{CP} = \sum_i^{\text{tagging}} \left[ \sum_{B^0 \text{ tag}} \ln \mathcal{F}_+(\Delta t; \Gamma, \Delta m_d, \hat{a}, w_i, \sin 2\beta) + \sum_{\bar{B}^0 \text{ tag}} \ln \mathcal{F}_-(\Delta t; \Gamma, \Delta m_d, \hat{a}, w_i, \sin 2\beta) \right], \quad (13)$$

where the outer summation is over tagging categories  $i$  and the inner summations are over the  $B^0$  and  $\bar{B}^0$  tags within a given uniquely-assigned tagging category. In practice, the fit for  $\sin 2\beta$  is performed on the combined flavor-eigenstate and  $CP$  samples with a likelihood constructed from the sum of Eq. 5 and 13, in order to determine  $\sin 2\beta$ , the mistag fraction  $w_i$  for each tagging category, and the vertex resolution parameters  $\hat{a}_i$ . Additional terms are included in the likelihood to account for backgrounds and their time dependence.

The mistag rates can also be extracted with a time-integrated analysis as a cross check. Neglecting possible background contributions and assuming the flavor of  $B_{\text{flav}}$  is correctly identified, the observed time-integrated fraction of mixed events  $\chi_{\text{obs}}$  can be expressed as a function of the  $B^0$ - $\bar{B}^0$  mixing probability  $\chi_d$ :

$$\chi_{\text{obs}} = \chi_d + (1 - 2\chi_d)w, \quad (14)$$

where  $\chi_d = \frac{1}{2}x_d^2/(1 + x_d^2) = 0.174 \pm 0.009$  [11] and  $x_d = \Delta m_d/\Gamma$ . Taking advantage of the available decay time information, the statistical precision on  $w$  can be improved by selecting only events that fall into an optimized time interval  $|\Delta t| < t_0$ , where  $t_0$  is chosen so that

which, neglecting resolution effects, is proportional to  $\sin 2\beta$ :

$$\mathcal{A}_{CP}(\Delta t) \propto -\eta_{CP} \mathcal{D} \sin 2\beta \sin \Delta m_d \Delta t. \quad (12)$$

Since no time-integrated  $CP$  asymmetry effect is expected, an analysis of the time-dependent asymmetry is necessary. The interference between the two amplitudes, and hence the  $CP$  asymmetry, is maximal after approximately 2.1  $B^0$  proper lifetimes, when the mixing asymmetry goes through zero. However, the maximum sensitivity to  $\sin 2\beta$ , which is proportional to  $e^{-\Gamma|\Delta t|} \sin^2 \Delta m_d \Delta t$ , occurs in the region of 1.4 lifetimes.

The value of the free parameter  $\sin 2\beta$  can be extracted with the tagged  $B_{CP}$  sample by maximizing the likelihood function

the integrated number of mixed and unmixed events are equal outside this range. With the use of such an optimized  $\Delta t$  interval the time-integrated method achieves nearly the same statistical precision for the mistag rates as a full time-dependent likelihood fit.

### C. Overview of the analysis

This article provides a detailed description of our published measurement of flavor oscillations [15] and  $CP$ -violating asymmetry [16] in the neutral  $B$  meson system. These measurements have six main components:

- Selection of the  $B_{CP}$  sample of signal events for neutral  $B$  decays to  $CP$  modes  $J/\psi K_S^0$ ,  $\psi(2S)K_S^0$ ,  $\chi_{c1}K_S^0$ ,  $J/\psi K^{*0}$  ( $K^{*0} \rightarrow K_S^0 \pi^0$ ), and  $J/\psi K_L^0$ ; selection of the  $B_{\text{flav}}$  sample of signal events for neutral flavor-eigenstate decays to  $D^{(*)-} \pi^+ / \rho^+ / a_1^+$  and  $J/\psi K^{*0}$  ( $K^{*0} \rightarrow K^+ \pi^-$ ); selection of the  $B^+$  control sample in the modes  $\bar{D}^{(*)0} \pi^+$ ,  $J/\psi K^{(*)+}$ ,  $\psi(2S)K^+$ ,  $\chi_{c1}K^+$ ; and selection of a semileptonic neutral  $B$  sample in the mode  $D^{*+} \ell^- \bar{\nu}$ , as described in Section III;

- Determination of the flavor of the  $B_{\text{tag}}$ , as described in Section IV;
- Measurement of the distance  $\Delta z$  between the two  $B^0$  decay vertices along the  $\Upsilon(4S)$  boost axis, and its conversion to  $\Delta t$ , as described in Section V;
- Construction of a log-likelihood function to describe the time evolution of signal and background events in the presence of mixing and  $CP$  asymmetries, as described in Section VI;
- Measurement of the mixing rate  $\Delta m_d$ , mistag fractions  $w_i$ , and vertex resolution parameters  $\hat{a}_i$  for the different tagging categories  $i$ , with an unbinned maximum-likelihood fit to the  $B_{\text{flav}}$  sample, as described in Section VII;
- Extraction of a value of  $\sin 2\beta$ , or more generally  $Im\lambda/|\lambda|$  and  $|\lambda|$ , from the amplitude of the  $CP$  asymmetry, the mistag fractions  $w_i$ , and the vertex resolution parameters  $\hat{a}_i$  for the different tagging categories  $i$ , with an unbinned maximum-likelihood fit to the combined  $B_{\text{flav}}$  and  $B_{CP}$  samples, as described in Section VIII.

Whenever possible, we determine time and mass resolutions, efficiencies and mistag fractions from the data. The measurement of  $\Delta m_d$  is performed with a slightly reduced subset of the full  $B_{\text{flav}}$  sample, which is optimized for such a precision measurement. The  $B_{CP}$  sample is not included, since this would add additional assumptions about the resolution function without significantly improving the precision of  $\Delta m_d$ . The measurement of  $\sin 2\beta$  is performed with the full  $B_{\text{flav}}$  and  $B_{CP}$  samples, with a fixed value for  $\Delta m_d$  and the  $B^0$  lifetime. This strategy allows us to account correctly for the small correlations among the mistag rates,  $\Delta t$  resolutions parameters, and  $\sin 2\beta$ . The same  $B_{\text{flav}}$  sample and vertex separation techniques have been used to determine precision values for the charged and neutral  $B$  lifetimes [17].

## II. THE BABAR DETECTOR AND DATA SETS

The data used in this analysis were recorded with the *BABAR* detector [18] at the PEP-II collider [8] in the period October 1999–June 2001. The total integrated luminosity of the data set is equivalent to  $29.7 \text{ fb}^{-1}$  collected near the  $\Upsilon(4S)$  resonance and  $3.9 \text{ fb}^{-1}$  collected 40 MeV below the  $\Upsilon(4S)$  resonance (off-resonance data). The corresponding number of produced  $B\bar{B}$  pairs is estimated to be about 32 million. The  $\Upsilon(4S)$  sample is sometimes divided into two subsamples for comparison purposes: data recorded in 1999–2000, about  $20.7 \text{ fb}^{-1}$  and referred to as “Run 1”, and data recorded in 2001, about  $9.0 \text{ fb}^{-1}$  and referred to as “Run 2”. These subsamples differ primarily in the quality of the tracking system alignment and on the track-finding efficiency. The former requires a separate treatment of the  $\Delta t$  resolution for the two periods,

as discussed in Section V F, while the latter results in substantially improved yields in Run 2 for reconstructed  $B$  mesons.

### A. The *BABAR* detector

The *BABAR* detector is a charged and neutral spectrometer with large solid-angle coverage. For this analysis, the most important detector capabilities include charged-particle tracking, vertex reconstruction, and particle identification. Charged particles are detected and their momenta measured by a combination of a 40-layer, small-celled drift chamber (DCH) filled with a 80:20 helium:isobutane gas mixture, and a five-layer silicon vertex tracker (SVT), consisting of 340 AC-coupled double-sided silicon microstrip sensors. The cells of the DCH are organized into 10 superlayers within which the sense wires all have the same orientation, thereby allowing segment-based tracking. Both the DCH and the SVT lie inside a 1.5-T solenoidal magnetic field. Beyond the outer radius of the DCH is a detector of internally reflected Cherenkov radiation (DIRC), which is used primarily for charged-hadron identification. The device consists of 144 fused silica quartz bars in which relativistic charged particles above the Cherenkov threshold radiate photons while traversing the material. The light is transported by total internal reflection down the length of the bars to an array of 10752 photomultiplier tubes mounted on the rear of the detector, where the opening angle of the Cherenkov ring is measured. A finely segmented electromagnetic calorimeter (EMC), consisting of 6580 CsI(Tl) crystals, is used to detect photons and neutral hadrons, and also to identify electrons. The EMC is surrounded by a thin cylindrical superconducting coil and a segmented iron flux return, organized into a hexagonal barrel and two endcaps. The instrumented flux return (IFR) consists of multiple layers of resistive plate chambers (RPCs) interleaved with the flux-return iron and is used in the identification of muons and neutral hadrons.

### B. Charged particle reconstruction

Charged track finding starts with pattern recognition in the DCH, based on three different algorithms. The first uses the same fast algorithm employed by the Level-3 trigger for finding and linking superlayer-based track segments from moderate-to-high  $p_T$  tracks originating from the interaction point. Two subsequent track finders then work on superlayer segments not already attached to a reconstructed track. They are designed to find tracks with lower  $p_T$ , passing through fewer than the full ten superlayers of the chamber, or originating away from the interaction point. At the end of this process, all tracks are refit with a Kalman-filter fitter [19] that takes into account the detailed distribution of material in the detector and the non-uniformities in the detector magnetic

field. These tracks are then projected into the SVT, and silicon-strip hits are added if they are consistent within the extrapolation errors through the intervening material and field. A search is performed for tracks that are reconstructed with the remaining unused silicon clusters, again with two different algorithms. At the end of the SVT-only track finding, an attempt is made to match SVT- and DCH-only track segments, which may result when a hard scatter occurs in the support tube material between the two devices.

Charged-particle transverse momenta  $p_T$  are determined with a resolution parameterized by  $\sigma(p_T)/p_T = 0.0013(p_T/\text{GeV}/c) + 0.0045$ . The SVT, with typical single-hit resolution of  $10\ \mu\text{m}$ , provides vertex information in both the transverse plane and in  $z$ , as well as the decay angles at the interaction point. Decay vertices for  $B$  meson candidates are typically reconstructed with a resolution of  $50\ \mu\text{m}$  in  $z$  for fully reconstructed modes and about 100 to  $150\ \mu\text{m}$  for the vertex of the (unreconstructed) tagging  $B$  meson in the event. The efficiency for finding tracks in hadronic events that traverse the full DCH radius ( $p_T > 200\ \text{MeV}/c$ ) is about 90% for Run 1 and 95% for Run 2.

### C. Neutral reconstruction

EMC clusters are formed around initial seed crystals containing at least 10 MeV of deposited energy. Neighboring crystals are added to the cluster if their energy exceeds 1 MeV. If the newly added crystal has energy greater than 3 MeV, its contiguous neighbors (including corners) are also considered for inclusion in the cluster. In order to identify cases where several showers are in close proximity, such as unresolved photons from high-energy  $\pi^0$  decays, local maxima within a cluster are identified. These local maxima are defined as candidate crystals that have an energy exceeding each of its neighbors by a fraction that depends on the number of crystals in the local neighborhood. Clusters are then divided into as many “bumps” as there are local maxima. The division is based on a two-dimensional weighting scheme that assumes electromagnetic shower shapes to divide up the cluster energy. The position of each bump is calculated with a logarithmic weighting of crystal energies.

We determine whether a bump is associated with a charged or neutral particle by projecting all tracks in the event to the inner face of the calorimeter. A bump is determined to be neutral, and therefore a photon candidate, if no track intersects any of its crystals. A track intersection is determined by computing the two-dimensional distance on the face of the calorimeter from the projected track impact point to the bump centroid. A requirement is made on the difference between the measured intersection distance and the Monte Carlo expectation for different particle species based on the measured track parameters.

The energy resolution in the EMC is measured directly

with a radioactive source at low energy under ideal low-background conditions and with electrons from Bhabha scattering at high energy, from which we determine  $\sigma(E)/E = (5.0 \pm 0.8)\%$  at 6.13 MeV and  $(1.9 \pm 0.07)\%$  at 7.5 GeV. The energy resolution can also be extracted from the observed mass resolutions for  $\pi^0$  and  $\eta$  decays to two photons, which are measured to be around 7 MeV and 16 MeV, respectively. A fit to the observed resolutions obtained from the  $\pi^0$ ,  $\eta$ , and Bhabha samples gives a photon energy resolution parameterized by  $\sigma(E)/E = 0.023(E/\text{GeV})^{-1/4} \oplus 0.019$ .

### D. Particle identification

Identification of electrons, muons and kaons is an essential ingredient in both  $B$  reconstruction and flavor tagging. Particle species can be distinguished by measurements of the specific energy loss ( $dE/dx$ ) in the SVT layers and in the DCH gas along the particle trajectory, the number of Cherenkov photons and the Cherenkov angle in the DIRC, the electromagnetic shower energy in the EMC, and the particle penetration length in the IFR. Selection criteria are based on these quantities, on likelihood ratios derived from them, or on neural network algorithms combining different detector likelihoods. Typically, looser selection criteria are applied for  $B$  reconstruction than for  $B$ -flavor tagging. Efficiencies and particle misidentification probabilities are determined from data control samples with similar characteristics.

#### 1. Electron identification

Electron candidates are identified primarily by the ratio of the bump energy in the electromagnetic calorimeter to the track momentum,  $E/p$ . They also must have a measured mean  $dE/dx$  in the DCH that is consistent with the electron hypothesis. In addition, for some applications, the lateral and azimuthal shape of the EMC shower [20, 21] and the consistency of the observed and expected Cherenkov angle in the DIRC are used for identification. Four different categories of electron candidates (**VeryLoose**, **Loose**, **Tight**, and **VeryTight**) are defined with the criteria listed in Table I. Candidates that are not matched to an EMC bump are retained as **noCal** electron candidates if their measured  $dE/dx$  satisfies the same requirements as the **VeryTight** selection. Electron identification efficiencies in the momentum range  $0.5 < p < 3.0\ \text{GeV}/c$  vary between 88% and 98% for the criteria in Table I, while the pion misidentification rates are below 0.3% for the **VeryTight** selection.

#### 2. Muon identification

Muon candidates are primarily identified by the measured number of hadronic interaction lengths  $n_\lambda$  tra-

TABLE I: Criteria used for selecting the available categories of electron candidates. The difference between the measured mean  $dE/dx$  and the expectation for an electron is required to lie within the interval specified in terms of the expected  $dE/dx$  resolution  $\sigma$ .

Category	$dE/dx$	$E/p$	Cumulative additional requirements
<b>VeryLoose</b>	$[-3\sigma, 7\sigma]$	$> 0.50$	–
<b>Loose</b>	$[-3\sigma, 7\sigma]$	$> 0.65$	–
<b>Tight</b>	$[-3\sigma, 7\sigma]$	$[0.75, 1.3]$	Lateral shower shape
<b>VeryTight</b>	$[-2.2\sigma, 4\sigma]$	$[0.89, 1.2]$	Azimuthal shower shape; consistency of DIRC Cherenkov angle ( $3\sigma$ )

TABLE II: Criteria used for selecting available categories of muon candidates.

Category	$n_\lambda$	$\Delta n_\lambda$	$\bar{n}_{hits}$	$\sigma_{n_{hits}}$	$\chi_{trk}^2/n_{layers}$	$\chi_{fit}^2/n_{layers}$	$E_{EMC}$ [GeV]
<b>VeryLoose</b>	$> 2.0$	$< 2.5$	$< 10$	$< 6$	–	–	$< 0.5$
<b>Loose</b>	$> 2.0$	$< 2.0$	$< 10$	$< 6$	$< 7$	$< 4$	$< 0.5$
<b>Tight</b>	$> 2.2$	$< 1.0$	$< 8$	$< 4$	$< 5$	$< 3$	$[0.05, 0.4]$
<b>VeryTight</b>	$> 2.2$	$< 0.8$	$< 8$	$< 4$	$< 5$	$< 3$	$[0.05, 0.4]$

versed from the outside radius of the DCH through the IFR iron, and the difference  $\Delta n_\lambda$  between  $n_\lambda$  and the predicted penetration depth for a muon of the same momentum and angle. Contamination from hadronic showers is rejected by a combination of the average number  $\bar{n}_{hits}$  and the variance  $\sigma_{n_{hits}}$  of hits per RPC layer, the  $\chi^2$  for the geometric match between the track extrapolation into the IFR and the RPC hits,  $\chi_{trk}^2$ , and the  $\chi^2$  of a polynomial fit to the RPC hits,  $\chi_{fit}^2$ . In addition, for those muons within the acceptance of the EMC, we require the calorimeter bump energy  $E$  to be consistent with a minimum ionizing particle. Four different categories of muon candidates (**VeryLoose**, **Loose**, **Tight**, and **VeryTight**) are selected with the criteria listed in Table II. In the forward region, which suffers from some machine background, additional requirements are made on the fraction of RPC layers with hits. Muon identification efficiencies in the momentum range  $1.1 < p < 3.0 \text{ GeV}/c$  vary between 60% to 92% for the criteria in Table II, while pion misidentification rates are about 3% for the **Tight** selection.

### 3. Kaon identification

Kaons are distinguished from pions and protons on the basis of specific energy-loss measurements  $dE/dx$  in SVT and DCH and the number of Cherenkov photons and the Cherenkov angle in the DIRC. The difference between the measured truncated-mean  $dE/dx$  in the DCH and the expected mean for the pion, kaon and proton hypothesis, with typical resolution of 7.5%, is used to compute likelihoods  $\mathcal{L}_\pi$ ,  $\mathcal{L}_K$  and  $\mathcal{L}_p$  assuming Gaussian distributions. Similarly, the difference between the measured 60% truncated-mean  $dE/dx$  in the SVT and the expected  $dE/dx$  is described by an asymmetric Gaussian distribution. For minimum-ionizing particles the resolu-

tion on the SVT truncated mean is about 14%. In the DIRC, a likelihood is obtained for each particle hypothesis from the product of two components: the expected number of Cherenkov photons, with a Poisson distribution, and the difference between the measured average Cherenkov angle to the expected angle for a given mass hypothesis, assuming a Gaussian distribution.

For  $B$ -flavor tagging the likelihood variables from SVT, DCH and DIRC are combined as inputs to a neural network whose output is a single discriminating variable for kaon selection. The network is trained with Monte Carlo simulation of generic  $B$  decays. The average efficiency of the selection is about 85% for a pion-misidentification probability of about 2.5%. Further details are described in Section IV B.

The exclusive reconstruction of many  $B$  meson final states does not generally require explicit kaon identification. For some channels a **VeryLoose** kaon selection based on likelihood ratios is imposed to reduce backgrounds to acceptable levels. The combined likelihood uses the individual likelihoods from SVT and DCH for momenta below  $0.5 \text{ GeV}/c$ , from DCH only for momenta between  $0.5$  and  $0.6 \text{ GeV}/c$ , and from DIRC only for momenta above  $0.6 \text{ GeV}/c$ . Kaon candidates are rejected if the likelihood ratios satisfy  $\mathcal{L}_K/\mathcal{L}_\pi < r$  and  $\mathcal{L}_K/\mathcal{L}_p < r$ , where  $r = 0.1$  for  $p < 0.5 \text{ GeV}/c$  and  $r = 1$  for  $p \geq 0.5 \text{ GeV}/c$ . Tracks with no particle information are assumed to be kaons. This **VeryLoose** kaon requirement has a nearly constant kaon-identification efficiency of about 96% and a pion-misidentification probability of at most 15% for tracks in the transverse momentum range  $1$  to  $2.5 \text{ GeV}/c$ . Tighter kaon selections require  $\mathcal{L}_K/\mathcal{L}_\pi > r$ , with  $r$  typically greater than one. For a loose pion selection, candidates are rejected if they satisfy tighter kaon or lepton criteria.

### III. RECONSTRUCTION OF $B$ MESONS

Neutral  $B$  mesons in flavor eigenstates are reconstructed in the hadronic final states  $B^0 \rightarrow D^{(*)-}\pi^+$ ,  $D^{(*)-}\rho^+$ ,  $D^{(*)-}a_1^+$ , and  $J/\psi K^{*0}(K^+\pi^-)$ , and the semileptonic decay mode  $B^0 \rightarrow D^{*-}\ell^+\nu$ . The  $CP$  sample is reconstructed in the channels  $B^0 \rightarrow J/\psi K_S^0$ ,  $\psi(2S)K_S^0$ ,  $\chi_{c1}K_S^0$ ,  $J/\psi K^{*0}$  ( $K^{*0} \rightarrow K_S^0\pi^0$ ) and  $J/\psi K_L^0$ . In some cases, control samples of charged  $B$  decays are studied, where the hadronic final states  $B^+ \rightarrow \bar{D}^{(*)0}\pi^+$ ,  $J/\psi K^{(*)+}$ ,  $\psi(2S)K^+$  and  $\chi_{c1}K^+$  are used. All final-state particles, with the exception of the neutrino in the semileptonic decay, are reconstructed. A number of  $\bar{D}^0$  and  $D^-$  decay modes are used to achieve reasonable reconstruction efficiency despite the typically small branching fractions for any given  $B$  or  $D$  decay channel. A summary of the various reconstructed  $B$  samples and purities is provided in Table III.

TABLE III: Event yields for the different samples used in this analysis, before any tagging or tagging vertex requirements. The yields, purity, and signal size for  $B$  decays to hadronic final states are obtained from a fit to the  $m_{ES}$  distribution described in Section III C, after selection on  $\Delta E$ . Purities are quoted for  $m_{ES} > 5.27 \text{ MeV}/c^2$ . The results for  $J/\psi K_L^0$  are obtained from a fit to the  $\Delta E$  distribution described in Section III D. The purity for  $J/\psi K_L^0$  is quoted for events with  $\Delta E < 10 \text{ MeV}$ . The results for  $D^{*-}\ell^+\nu$  are obtained from a fit to the  $\cos\theta_{B-D^*\ell}$  distribution described in Section III E. Purity is quoted for  $-1.1 < \cos\theta_{B-D^*\ell} < 1.1$ .

Sample	Final state	Signal	Purity (%)
$B_{CP}$	$J/\psi K_S^0$ ( $K_S^0 \rightarrow \pi^+\pi^-$ )	$461 \pm 22$	99
	$J/\psi K_S^0$ ( $K_S^0 \rightarrow \pi^0\pi^0$ )	$113 \pm 12$	93
	$\psi(2S)K_S^0$	$86 \pm 17$	96
	$\chi_{c1}K_S^0$	$44 \pm 8$	98
	$J/\psi K^{*0}$ ( $K^{*0} \rightarrow K_S^0\pi^0$ )	$64 \pm 10$	74
	$J/\psi K_L^0$	$257 \pm 24$	60
	Total	$1025 \pm 41$	83
$B_{flav}$	$D^{*-}\pi^+$	$2380 \pm 57$	92
	$D^{*-}\rho^+$	$1438 \pm 52$	84
	$D^{*-}a_1^+$	$1146 \pm 45$	80
	$D^-\pi^+$	$2685 \pm 65$	83
	$D^-\rho^+$	$1421 \pm 57$	74
	$D^-a_1^+$	$845 \pm 44$	67
	$J/\psi K^{*0}$ ( $K^{*0} \rightarrow K^+\pi^-$ )	$1013 \pm 36$	95
	Total	$10941 \pm 133$	83
$B^+$	$\bar{D}^0\pi^+$	$6850 \pm 102$	83
	$\bar{D}^{*0}\pi^+$	$1708 \pm 51$	91
	$J/\psi K^+$	$1921 \pm 46$	97
	$\psi(2S)K^+$	$292 \pm 18$	98
	$\chi_{c1}K^+$	$195 \pm 29$	95
	$J/\psi K^{*+}$ ( $K^{*+} \rightarrow K^+\pi^0$ )	$384 \pm 25$	87
	Total	$11343 \pm 129$	86
Semi-leptonic $B^0$	$D^{*-}\ell^+\nu$	$29042 \pm 1500$	78

#### A. Event selection

Multihadron events are selected by demanding a minimum of three reconstructed charged tracks in the polar angle range  $0.41 < \theta_{lab} < 2.54 \text{ rad}$ . Charged tracks must be reconstructed in the DCH and are required to originate within 1.5 cm in  $xy$  and 10 cm in  $z$  of the nominal beamspot. A primary vertex is formed on an event-by-event basis from a vertex fit to all charged tracks in the fiducial volume. Tracks with a large  $\chi^2$  contribution to the vertex fit are removed until an overall  $\chi^2$  probability greater than 1% is obtained or only two tracks remain. The resolution achieved by this method is about  $70 \mu\text{m}$  in  $x$  and  $y$  for hadronic events. Events are required to have a primary vertex within 0.5 cm of the average position of the interaction point in the plane transverse to the beamline, and 6 cm longitudinally. Electromagnetic bumps in the calorimeter in the polar angle range  $0.410 < \theta_{lab} < 2.409 \text{ rad}$  that are not associated with charged tracks, have an energy greater than 30 MeV, and a shower shape consistent with a photon interaction are taken as neutrals. A total energy greater than 4.5 GeV in the fiducial regions for charged tracks and neutrals is required. To reduce continuum background, we require the normalized second Fox-Wolfram moment [22]  $R_2$  of the event, calculated with both charged tracks and neutrals, to be less than 0.5 (0.45) in hadronic (semileptonic) decay modes. The  $\ell^{\text{th}}$  Fox-Wolfram moment is the momentum-weighted sum of Legendre polynomial of the  $\ell^{\text{th}}$  order computed from the cosine of the angle between all pairs of tracks. The ratio  $R_2$  provides good separation between jet-like continuum events and more spherical  $B\bar{B}$  events.

#### B. Reconstruction of decay daughters

The reconstruction of  $B$  mesons typically involves the summation of a set of related decay modes, with multiple decay chains for the charm daughters or other short-lived decay products. To simplify analysis of such complex decay chains, virtual *composite* particles and their error matrices are constructed from the original daughter particles. The composite particle then replaces the daughters in subsequent fits and analysis. The three-momentum of the virtual particle is fit directly, rather than computed from the updated daughters, improving speed and numerical accuracy.

Vertex and kinematic fitting is used to improve four-momenta and position measurements, as well as to measure the time difference between decaying  $B$  hadrons in the  $\Upsilon(4S) \rightarrow B\bar{B}$  decay. For example, in the case of  $B^0 \rightarrow J/\psi K_S^0$ , the position measurement of the  $B^0$  can be improved with the constraint that the line-of-flight of the  $K_S^0$  intersects the  $J/\psi$  vertex. The energy resolution of the  $B^0$  can also be improved by applying a mass

constraint to the  $J/\psi$  and  $K_s^0$  daughters. Generalized procedures have been developed and tested with constraints implemented by the Lagrange-multiplier technique. Possible constraints include a common decay vertex, mass, energy, momentum, beam energy (with and without smearing), beam-spot position and line-of-flight.

Non-linearities in the fits require the use of an iterative procedure, where convergence is defined by demanding that the change in  $\chi^2$  between two successive iterations is less than 0.01, within a maximum of six iterations. Simple fits involving only vertex constraints (except long-lived particles) are, however, accurate enough with a single iteration.

### 1. $\pi^0$ selection

Neutral pion candidates are formed from pairs of EMC bumps with energy greater than 30 MeV, assumed to be photons originating from the interaction point. The invariant mass of the photon pair is required to be within  $\pm 20 \text{ MeV}/c^2$  ( $2.5\sigma$ ) of the nominal  $\pi^0$  mass, with a minimum summed energy of 200 MeV. Selected candidates are subjected to a kinematic fit with a  $\pi^0$  mass constraint. Within the acceptance of the EMC, efficiencies for this selection vary from about 55 to 65% for  $\pi^0$  energies from 0.3 to 2.5 GeV, typical of  $B$  decays.

### 2. $K_s^0$ selection

Candidates in the  $K_s^0 \rightarrow \pi^+\pi^-$  mode are selected by requiring an invariant  $\pi^+\pi^-$  mass, computed at the vertex of the two tracks, between 462 and 534  $\text{MeV}/c^2$ . The  $\chi^2$  of the vertex fit must have a probability greater than 0.1%. The angle between the flight direction and the momentum vector for the  $K_s^0$  candidate is required to be smaller than 200 mrad. Finally, the transverse flight distance from the primary vertex in the event,  $r_{xy}$ , must be greater than 2 mm.

Optimization for the reconstruction of the  $CP$  sample has produced slightly different  $K_s^0$  selection criteria. The  $\pi^+\pi^-$  invariant mass, determined at the vertex of the two tracks, is required to lie between 489 and 507  $\text{MeV}/c^2$  and the three-dimensional flight length with respect to the vertex of the charmonium candidate is required to be greater than 1 mm.

Pairs of  $\pi^0$  candidates, each in the mass range 100–155  $\text{MeV}/c^2$  ( $-5\sigma$ ,  $+3\sigma$ ) and formed from non-overlapping EMC bumps, are combined to construct  $K_s^0 \rightarrow \pi^0\pi^0$  candidates. For each  $K_s^0$  candidate with an energy greater than 800 MeV and a mass between 300 and 700  $\text{MeV}/c^2$  at the interaction point, we determine the most probable  $K_s^0$  decay point along the path defined by the initial  $K_s^0$  momentum vector and the  $J/\psi$  vertex by maximizing the product of probabilities for the daughter  $\pi^0$  mass-constrained fits. Allowing for vertex resolution, we require the distance from the decay point

to the  $J/\psi$  vertex to be between  $-10$  and  $+40$  cm and the  $K_s^0$  mass, using the measured decay point, to be between 470 and 536  $\text{MeV}/c^2$ .

### 3. $K_L^0$ selection

Candidates for  $K_L^0$  mesons are identified in the EMC and IFR detectors as reconstructed clusters that cannot be associated with any charged track in the event. EMC candidates must have a cluster energy between 200 MeV and 2 GeV and a polar angle  $\theta$  that satisfies  $\cos\theta < 0.935$ . To suppress backgrounds from  $\pi^0$  decay,  $K_L^0$  candidates consistent with a photon are paired with other neutrals with  $E_\gamma > 30$  MeV. Any candidate with  $100 < m(\gamma\gamma) < 150 \text{ MeV}/c^2$  is rejected. Likewise, clusters with more than 1 GeV energy that contain two bumps are rejected if the bump energies and shower shapes are consistent with two photons from a  $\pi^0$  decay. Monte Carlo simulation shows that clusters due to true  $K_L^0$  mesons are easily distinguished from  $\pi^0$  candidates by these criteria. The remaining background consists primarily of photons and overlapping showers. Isolated clusters produced by charged hadrons are removed by the basic clustering algorithm, which requires a minimum separation of about 20 cm between clusters.

IFR candidates are defined as clusters with hits in two or more RPC layers that are not matched to any reconstructed charged track. To reduce beam-related backgrounds and to avoid regions where the charged tracking efficiency is low, we require that the polar angle  $\theta$  of the IFR cluster satisfy  $-0.75 < \cos\theta < 0.93$ , and eliminate clusters that begin in the outer 25% of the forward IFR endcap. Due to the irregular structure of hadronic showers, some hits from charged tracks are missed by the tracking association. We suppress these clusters by rejecting  $K_L^0$  candidates that lie within  $\pm 350$  mrad in polar angle and in the range  $-750(-300)$  to  $+300(+750)$  mrad in azimuth of the EMC intersection of any positively (negatively) charged track in the event. The remaining background is predominantly from charged particles and detector noise.

Some  $K_L^0$  candidates satisfy both the EMC and IFR selection requirements. In the reconstruction of  $B^0 \rightarrow J/\psi K_L^0$ , additional criteria described in Section III D are applied to resolve the classification of the corresponding  $B$  candidates. Extensive studies of  $K_L^0$  detection efficiencies have been conducted with a control sample of radiatively produced  $\phi$  mesons, decaying to  $K_L^0 K_S^0$ .

### 4. Selection of light resonances

For  $\rho^-$  candidates, the  $\pi^-\pi^0$  mass is required to lie within  $\pm 150 \text{ MeV}/c^2$  of the nominal  $\rho^-$  mass. The  $\pi^0$  from the  $\rho^-$  decay is required to have an energy greater than 300 MeV. We reconstruct  $K^{*0}$  candidates in the  $K^+\pi^-$  and  $K_s^0\pi^0$  modes, while  $K^{*+}$  candidates are re-

constructed in the  $K^+\pi^0$  and  $K_s^0\pi^+$  modes. The invariant mass of the two daughters is required to be within  $\pm 100 \text{ MeV}/c^2$  of the nominal  $K^*$  mass. Candidates in the mode  $a_1^+ \rightarrow \pi^+\pi^-\pi^+$  are reconstructed by combining three charged pions, with invariant mass in the range of 1.0 to 1.6  $\text{GeV}/c^2$ . In addition, the  $\chi^2$  probability of a vertex fit of the  $a_1^+$  candidate is required to be greater than 0.1%.

### 5. Charmed meson and charmonium selection

The decay channels  $K^+\pi^-$ ,  $K^+\pi^-\pi^0$ ,  $K^+\pi^+\pi^-\pi^-$  and  $K_s^0\pi^+\pi^-$  are used to reconstruct  $\bar{D}^0$  candidates, while  $D^-$  candidates are selected in the  $K^+\pi^-\pi^-$  and  $K_s^0\pi^-$  modes. Charged and neutral kaons are required to have a momentum greater than 200  $\text{MeV}/c$ . The same criterion is applied to the pion in  $B^0 \rightarrow D^{(*)-}\pi^+$ ,  $B^0 \rightarrow D^{(*)-}\rho^+$  decay. For the decay modes  $B^0 \rightarrow D^{(*)-}a_1^+$ , the pions are required to have momentum larger than 150  $\text{MeV}/c$ . We require  $\bar{D}^0$  and  $D^-$  candidates to lie within  $\pm 3\sigma$  of the nominal masses, where the error  $\sigma$  is calculated event-by-event. The distributions of the difference between measured and nominal  $\bar{D}^0$  and  $D^-$  meson masses, normalized by the measured error on the candidate masses, are found to have an RMS in the range 1.1–1.2 when fit with a Gaussian distribution. For  $\bar{D}^0 \rightarrow K^+\pi^-\pi^0$ , we only reconstruct the dominant resonant mode  $\bar{D}^0 \rightarrow K^+\rho^-$ , followed by  $\rho^- \rightarrow \pi^-\pi^0$ . The angle  $\theta_{D^0\pi}^*$  between the  $\pi^-$  and  $\bar{D}^0$  in the  $\rho^-$  rest frame must satisfy  $|\cos\theta_{D^0\pi}^*| > 0.4$ . Finally, all  $\bar{D}^0$  and  $D^-$  candidates are required to have a momentum greater than 1.3  $\text{GeV}/c$  in the  $\Upsilon(4S)$  frame and a  $\chi^2$  probability for the topological vertex fit greater than 0.1%. A mass-constrained fit is applied to candidates satisfying these requirements.

We form  $D^{*-}$  candidates in the decay  $D^{*-} \rightarrow \bar{D}^0\pi^-$  by combining a  $\bar{D}^0$  with a pion that has momentum greater than 70  $\text{MeV}/c$ . The soft pion is constrained to originate from the beamspot when the  $D^{*-}$  vertex is computed. To account for the small energy release in the decay  $\Upsilon(4S) \rightarrow B\bar{B}$  (resulting in a small transverse flight of the  $B$  candidates), the effective vertical size of the beam spot is increased to 40  $\mu\text{m}$ . Monte Carlo simulation was used to verify that this does not introduce any significant bias in the selection or in the  $\Delta t$  measurement. After applying a mass-constrained fit to the  $\bar{D}^0$  daughter,  $D^{*-}$  candidates are required to have  $m(\bar{D}^0\pi^-)$  within  $\pm 1.1 \text{ MeV}/c^2$  of the nominal  $D^{*-}$  mass for the  $\bar{D}^0 \rightarrow K^+\pi^-\pi^0$  mode and  $\pm 0.8 \text{ MeV}/c^2$  for all other modes. This corresponds to about  $\pm 2.5$  times the RMS width of the signal distribution, which is estimated by taking a weighted average of the core and broad Gaussian components of the observed  $m(\bar{D}^0\pi^-)$  distributions.

We form  $\bar{D}^{*0}$  candidates by combining a  $\bar{D}^0$  with a  $\pi^0$  with momentum less than 450  $\text{MeV}/c$  in the  $\Upsilon(4S)$  frame.  $\bar{D}^{*0}$  candidates are required to have  $m(\bar{D}^0\pi^0)$  within  $\pm 4 \text{ MeV}/c^2$  of the nominal value, after applying a

mass-constrained fit to the  $\bar{D}^0$  daughter.

Candidates for  $J/\psi$  and  $\psi(2S)$  mesons are reconstructed in their  $e^+e^-$  and  $\mu^+\mu^-$  decay modes, while  $\psi(2S)$  mesons are also reconstructed in the  $J/\psi\pi^+\pi^-$  channel. Table IV shows the particle identification and invariant mass requirements for the  $e^+e^-$  and  $\mu^+\mu^-$  daughters. These vary with reconstructed  $B$  decay channel due to the differing levels of background encountered. For  $J/\psi \rightarrow e^+e^-$  and  $\psi(2S) \rightarrow e^+e^-$  decays, where the electron may have radiated Bremsstrahlung photons, the missing energy is recovered by identifying clusters with more than 30  $\text{MeV}$  lying within 35  $\text{mrad}$  in polar angle and 50  $\text{mrad}$  in azimuth of the electron direction projected onto the EMC.

For the  $\psi(2S) \rightarrow J/\psi\pi^+\pi^-$  mode,  $J/\psi$  candidates are constrained to the nominal mass and then combined with pairs of oppositely-charged tracks considered as pions, with invariant mass between 400 and 600  $\text{MeV}/c^2$ . Candidates with  $0.574 < m(J/\psi\pi^+\pi^-) - m(J/\psi) < 0.604 \text{ GeV}/c^2$  are retained.

Photon candidates used for the reconstruction of  $\chi_{c1} \rightarrow J/\psi\gamma$  are required to lie within the calorimeter fiducial volume ( $0.41 < \theta_\gamma < 2.41 \text{ rad}$ ) and have an energy greater than 150  $\text{MeV}$ . In addition, the candidate should not form, in combination with any other photon in the event having at least 70  $\text{MeV}$  of energy, a  $\pi^0$  candidate with mass between 120 and 150  $\text{MeV}/c^2$ . The invariant mass of the  $\chi_{c1}$  candidates is required to be greater than 3.476 and smaller than 3.546  $\text{GeV}/c^2$ .

### C. B meson selection in fully-reconstructed modes

We reconstruct  $B$  candidates in all modes except  $B^0 \rightarrow J/\psi K_L^0$  and  $B^0 \rightarrow D^{*-}\ell^+\bar{\nu}$  using a pair of nearly uncorrelated kinematic variables, the difference  $\Delta E$  between the energy of the  $B$  candidate and the beam energy in the  $\Upsilon(4S)$  center-of-mass frame, and the beam-energy substituted mass,  $m_{\text{ES}}$ , defined as

$$m_{\text{ES}} = \sqrt{\left(\frac{\frac{1}{2}s + \mathbf{p} \cdot \mathbf{p}_i}{E_i}\right)^2 - p^2}, \quad (15)$$

where  $s$  is the square of the center-of-mass energy,  $E_i$  and  $\mathbf{p}_i$  are the total energy and the three momentum of the initial state in the laboratory frame, and  $\mathbf{p}$  is the three momentum of the  $B$  candidate in the same frame. For the purpose of determining event counts and purities, a signal region is defined in the  $(m_{\text{ES}}, \Delta E)$  plane as  $5.27 < m_{\text{ES}} < 5.29 \text{ GeV}/c^2$  and  $|\Delta E| < 3\sigma(\Delta E)$ , where  $\sigma(\Delta E)$  is the resolution on  $\Delta E$ . Likewise, a sideband region is defined as  $5.20 < m_{\text{ES}} < 5.26 \text{ GeV}/c^2$  and  $|\Delta E| < 3\sigma(\Delta E)$ . The value of  $\sigma(\Delta E)$  is mode-dependent and varies between 7 to 40  $\text{MeV}$  as measured in the data. When multiple  $B$  candidates (with  $m_{\text{ES}} > 5.20 \text{ MeV}/c^2$ ) are found in the same event, the candidate with the smallest value of  $|\Delta E|$  is selected.

Two types of background in the sample of selected  $B^0$  candidates are distinguished. The first background,

TABLE IV: Particle identification and invariant mass requirements for  $J/\psi$  and  $\psi(2S) \rightarrow \ell^+\ell^-$  candidates. The minimal particle identification criteria are applied to both daughters, while only one daughter must pass the restrictive requirement. Electron and muon selection requirements are defined in Section IID. Mass ranges are quoted in  $\text{GeV}/c^2$  and MIP refers to a minimum-ionizing particle.

$B$ channel	$e^+e^-$ candidates			$\mu^+\mu^-$ candidates		
	Minimal	Restrictive	$m(e^+e^-)$	Minimal	Restrictive	$m(\mu^+\mu^-)$
$J/\psi K_S^0$	None	Tight or noCal	2.95-3.14	MIP	Loose	3.06-3.14
$\psi(2S)K_S^0 (\ell^+\ell^-)$	VeryLoose	Tight	3.436-3.736	VeryLoose	Loose	3.06-3.14
$\psi(2S)K_S^0 (J/\psi \pi^+\pi^-)$	VeryLoose	Tight	2.95-3.14	VeryLoose	Loose	3.06-3.14
$\chi_{c1} K_S^0 (J/\psi \gamma)$	Loose	Tight	2.95-3.14	VeryLoose	Loose	3.06-3.14
$J/\psi K^*$	Tight	Tight	2.95-3.14	Loose	Loose	3.06-3.14
$J/\psi K_L^0$	Loose	VeryTight	3.00-3.13	Loose	Tight	3.06-3.13

called combinatorial, arises from random combinations of charged tracks and neutral showers from both  $B$  mesons in  $B\bar{B}$  events or from continuum events. This background is smoothly distributed in  $m_{\text{ES}}$  and does not peak near the  $B$  mass. The second, so-called ‘‘peaking’’ background, consists of events in which, for example, a slow pion from the reconstructed  $B$  meson is replaced by a slow pion from the tagging  $B$ , causing an enhancement near the nominal  $B$  mass. The peaking background from charged  $B$  decays is considered as a specific background source in the construction of the full likelihood function for  $B^0$ - $\bar{B}^0$  mixing, since these events have a particular time structure and set of effective dilutions. In this case, the peaking background from other neutral  $B$  decays has time-dependent properties and dilutions that are essentially identical to the signal and is treated as such. For the likelihood describing the  $CP$  sample, the peaking background is simply assumed to have zero effective  $CP$ .

Suppression of continuum background, in addition to a general requirement on  $R_2$ , is typically provided by restricting the thrust angle  $\theta_{\text{th}}$ , defined as the angle between the thrust axis of the particles that form the reconstructed  $B_{\text{rec}}$  candidate and the thrust axis of the remaining tracks and unmatched clusters in the event, computed in the  $\Upsilon(4S)$  frame. The two thrust axes are almost uncorrelated in  $B\bar{B}$  events, because the  $B^0$  mesons are nearly at rest in the  $\Upsilon(4S)$  rest frame. In continuum events, which are more jet-like, the two thrust axes tend to have small opening angles. Thus, a requirement on the maximum value of  $|\cos\theta_{\text{th}}|$  is effective in continuum rejection.

Signal yields and sample purities are extracted from fits to the  $m_{\text{ES}}$  distributions of  $B$  candidates with a Gaussian distribution for the signal and an ARGUS background shape [23] for the combinatorial background with a functional form given by

$$\mathcal{A}(m_{\text{ES}}; m_0, \xi) = A_B m_{\text{ES}} \sqrt{1 - x_{\text{ES}}^2} e^{\xi} (1 - x_{\text{ES}}^2), \quad (16)$$

for  $x_{\text{ES}} = m_{\text{ES}}/m_0 < 1$ , where  $m_0$  represents the kinematic upper limit and is held fixed at the center-of-mass beam energy  $E_b^* = 5.291 \text{ GeV}$ , and  $\xi$  and  $A_B$  are free parameters.

We assign background and signal probabilities to each event included in the likelihood fit based on the measured value for  $m_{\text{ES}}$ . However, it is the  $m_{\text{ES}}$  sideband region, where the background probabilities are essentially 100%, that dominates the determination of the combinatorial background fraction and  $\Delta t$  structure for background events under the  $B^0$  signal peak. Monte Carlo simulation shows a modest  $m_{\text{ES}}$  dependence on the composition of the combinatorial background over the sideband range  $m_{\text{ES}} > 5.2 \text{ GeV}/c^2$  through the  $B$  signal region, due to variation of the fraction of continuum versus  $B\bar{B}$  contributions. Since these two sources have different  $\Delta t$  behaviors, the changing composition leads to a small correction and systematic error on the precision mixing measurement, but is negligible for the  $\sin 2\beta$  extraction. The fraction of peaking backgrounds from charged  $B$  decays are estimated with Monte Carlo simulation as described in the following sections.

### 1. $B^0$ decays to flavor-eigenstates

Candidates in the  $B_{\text{flav}}$  sample of neutral flavor-eigenstate  $B$  mesons are formed by combining a  $D^{*-}$  or  $D^-$  with a  $\pi^+$ ,  $\rho^+$  ( $\rho^+ \rightarrow \pi^+\pi^0$ ),  $a_1^+$  ( $a_1^+ \rightarrow \pi^+\pi^-\pi^+$ ), or by combining a  $J/\psi$  candidate with a  $K^{*0}$  ( $K^{*0} \rightarrow K^+\pi^-$ ). As described in Section IID, kaon identification is used to reject background. For most  $B^0$  modes, it is possible to achieve signal purities of at least 90% with the **VeryLoose** selection, or no particle identification at all. However, for the mode  $B^0 \rightarrow D^- a_1^+$ , the tighter kaon identification is required to reduce large combinatorial backgrounds.

For final states with a  $D^*$  and 2 (3) pions we require  $|\cos\theta_{\text{th}}| < 0.9$  (0.8) for the  $\bar{D}^0 \rightarrow K^+\pi^-$  and  $K^+\pi^-\pi^0$  modes and 0.8 (0.7) for  $\bar{D}^0 \rightarrow K^+\pi^+\pi^-\pi^-$  and  $K_S^0\pi^+\pi^-$ , while no requirement is made for the  $B^0 \rightarrow D^{*-}\pi^+$  mode. In modes which contain a  $D^-$  and a  $\pi^+$ ,  $\rho^+$ , or  $a_1^+$  in the final state, we require  $|\cos\theta_{\text{th}}| < 0.9$ , 0.8, or 0.7, respectively.

The  $B^0$  signal yield and sample purity extracted from fits to the  $m_{\text{ES}}$  distribution are summarized in Table III. The net  $B^0$  signal sample, before applying any decay ver-



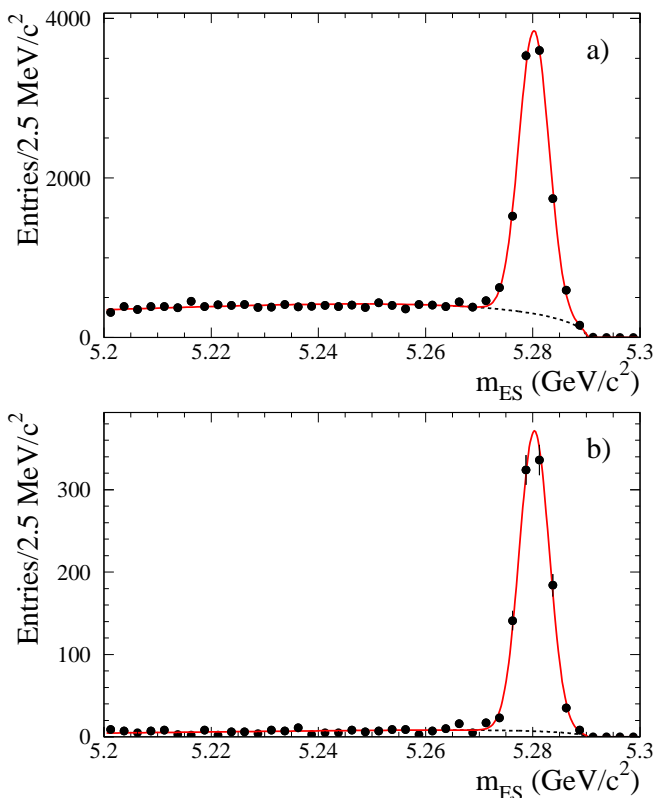


FIG. 3: Distribution of  $m_{ES}$  for all selected flavor-eigenstate  $B^0$  candidates in hadronic decays to (a) open charm and (b) charmonium final states. Overlaid in both cases is the result of a fit with a Gaussian distribution for the signal and an ARGUS function for the background.

text requirements, consists of  $9922 \pm 129$  signal candidates in open charm decays with a purity of about 82%, and  $1013 \pm 36$  in the decay  $B^0 \rightarrow J/\psi K^{*0}$  ( $K^{*0} \rightarrow K^+ \pi^-$ ), with a purity of about 95%. Figure 3 shows the combined  $m_{ES}$  distribution for all the hadronic  $B^0$  modes. Superimposed is the result of a fit with a Gaussian distribution for the signal and an ARGUS background form [23].

The signal obtained by this method includes a small fraction of peaking background from other charged and neutral  $B$  decay modes. However, only the charged  $B$  component needs to be determined, since it alone has a time structure that differs from the signal events. Therefore, the fraction of peaking background is estimated with a sample of  $\Upsilon(4S) \rightarrow B^+ B^-$  Monte Carlo events. The  $B^+$  mesons are forced to decay in the decay modes  $\bar{D}^{*0}$  or  $\bar{D}^0$  with a  $\pi^+$ ,  $\rho^+$ , or  $a_1^+$ , since the main source is decay channels that have one more or one fewer pion in the final state than the signal modes of interest. We then attempt to reconstruct neutral  $B$  mesons in the channels used for the  $B_{flav}$  sample in data. A small peak at the  $B^0$  mass, obtained with the charged  $B$  Monte Carlo sample, leads to an estimate of  $(1.3 \pm 0.3^{+0.2}_{-0.5})\%$  as the peaking component in the  $B_{flav}$  signal. This result is obtained from a fit with a Gaussian distribution, whose mean and

width are fixed by the  $B^0$  signal parameters. The  $\Delta t$  structure of the peaking background in Monte Carlo is found to be consistent with the lifetime of the  $B^+$ , as expected.

## 2. $B^+$ control samples

The  $B^+$  control sample of charged  $B$  candidates is formed by combining a  $\bar{D}^{*0}$ ,  $\bar{D}^0$ ,  $J/\psi$ , or  $\psi(2S)$  candidate with a  $\pi^+$  or  $K^+$ . For the  $\bar{D}^0 \pi^+$  final state, we require  $|\cos \theta_{th}| < 0.9$  for the  $\bar{D}^0 \rightarrow K^+ \pi^-$  mode and 0.8 for all other  $\bar{D}^0$  channels. In modes that contain a  $\bar{D}^{*0} \rightarrow \bar{D}^0 \pi^0$ , the requirement is  $|\cos \theta_{th}| < 0.9$  for  $\bar{D}^0 \rightarrow K^+ \pi^-$ , 0.8 for the  $K^+ \pi^- \pi^0$  and  $K^+ \pi^- \pi^- \pi^+$ , and 0.7 for  $K_s^0 \pi^+ \pi^-$ .

The  $B^+$  signal yield and sample purity extracted from fits to the  $m_{ES}$  distribution are summarized in Table III. The net  $B^+$  signal sample in open charm modes, before applying any decay-vertex requirements, consists of  $2797 \pm 62$  signal candidates in charmonium modes, with a purity of about 94%, and  $8547 \pm 115$  signal candidates in open charm modes, with a purity of about 84%. Figure 4 shows the combined  $m_{ES}$  distribution for all the hadronic  $B^+$  modes. Superimposed on the data is the result of a fit with a Gaussian distribution for the signal and an ARGUS background form [23].

## 3. $B^0$ decays to CP modes involving $K_s^0$

We form the  $B_{CP}$  sample of neutral  $B$  candidates in charmonium modes with a  $K_s^0$  by combining mass-constrained  $J/\psi$ ,  $\psi(2S)$  or  $\chi_{c1}$  candidates with mass-constrained  $K_s^0$  candidates, following the techniques of our recent branching-fraction study [24]. The helicity angle  $\theta_h$  of the  $J/\psi$  daughters with respect to the  $J/\psi$  flight direction in the  $B$  candidate rest frame should have a  $\sin^2 \theta_h$  distribution. Therefore, we require that  $|\cos \theta_h| < 0.8$  for the  $e^+ e^-$  mode and 0.9 for the  $\mu^+ \mu^-$  mode, as an efficient way of rejecting backgrounds. For the  $\psi(2S) K_s^0$  candidates,  $|\cos \theta_h|$  of the  $\psi(2S)$  must be smaller than 0.9 for both leptonic modes.

Distributions of  $m_{ES}$  are shown in Fig. 5 for the  $CP$  samples. Signal event yields and purities, determined from a fit to the  $m_{ES}$  distributions after selection on  $\Delta E$ , are summarized in Table III.

The fraction of peaking background has been estimated with a sample of  $B \rightarrow J/\psi X$  Monte Carlo events. The main source is decay channels that have one more or one less pion in the final state than the signal mode. The fractions are obtained by fitting the misreconstructed  $B \rightarrow J/\psi X$  sample with a Gaussian distribution, whose mean and width are fixed by the  $B^0$  signal parameters. The estimated contributions are  $(0.41 \pm 0.09)\%$ ,  $(1.2 \pm 0.2)\%$ ,  $(2.9 \pm 1.7)\%$ , and  $(1.1 \pm 1.1)\%$  for the  $J/\psi K_s^0$  ( $K_s^0 \rightarrow \pi^+ \pi^-$ ),  $J/\psi K_s^0$  ( $K_s^0 \rightarrow \pi^0 \pi^0$ ),  $\psi(2S) K_s^0$  and  $\chi_{c1} K_s^0$  channels respectively.

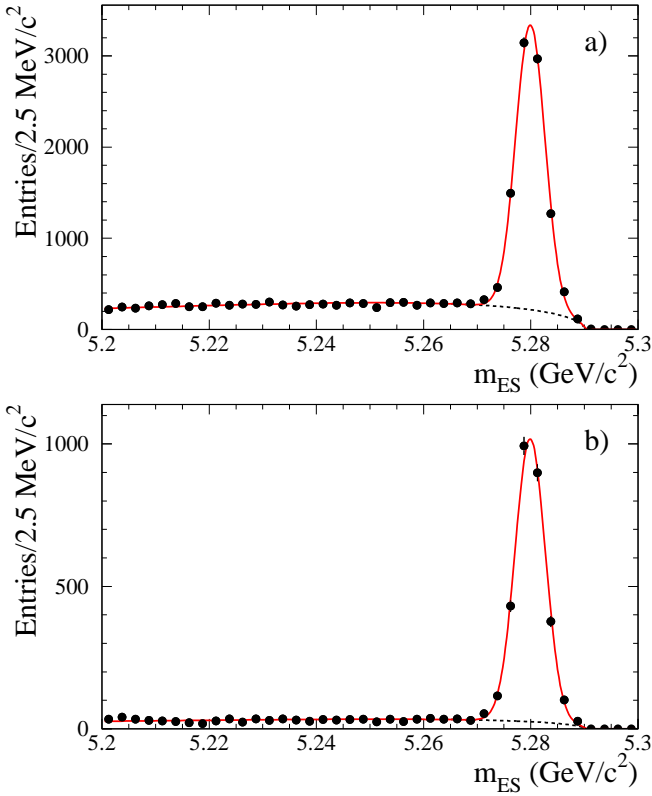


FIG. 4: Distribution of  $m_{ES}$  for all selected flavor-eigenstate  $B^+$  candidates in hadronic decays to (a) open charm and (b) charmonium final states. Overlaid in both cases is the result of a fit with a Gaussian distribution for the signal and an ARGUS function for the background.

In the case of the  $\chi_{c1}K_S^0$  mode we have also explored the possibility of contamination from  $\chi_{c2}K_S^0$  events. These would have a very similar final-state signature, but opposite  $CP$ . However, this decay mode has never been observed and the rate is expected to be highly suppressed due to angular momentum considerations. Figure 6 shows the invariant mass difference,  $m(\ell\ell\gamma) - m(\ell\ell)$ , for the  $\chi_{c1}$  daughters of the  $B^+ \rightarrow \chi_{c1}K^+$  and  $B^0 \rightarrow \chi_{c1}K_S^0$  candidates. The distribution is background subtracted with the  $m_{ES}$  sideband and a fit with two Crystal Ball distributions [25] is superimposed, where the means have been fixed to the known  $\chi_{c1}$  and  $\chi_{c2}$  masses and the widths are forced to be equal. The fraction of  $\chi_{c2}K$  events in the selected sample is found to be consistent with zero and, from the fit, an upper limit of 3.5% at 95% C.L. is set on the fraction of  $B \rightarrow \chi_{c2}K$  candidates in the selected sample.

#### 4. $B^0$ decays to the $CP$ mode $J/\psi K^{*0}$

The  $B_{CP}$  sample is further enlarged by the addition of  $B^0$  candidates in the mode  $J/\psi K^{*0}$  ( $K^{*0} \rightarrow K_S^0\pi^0$ ). For this purpose, mass-constrained  $J/\psi$  candidates are

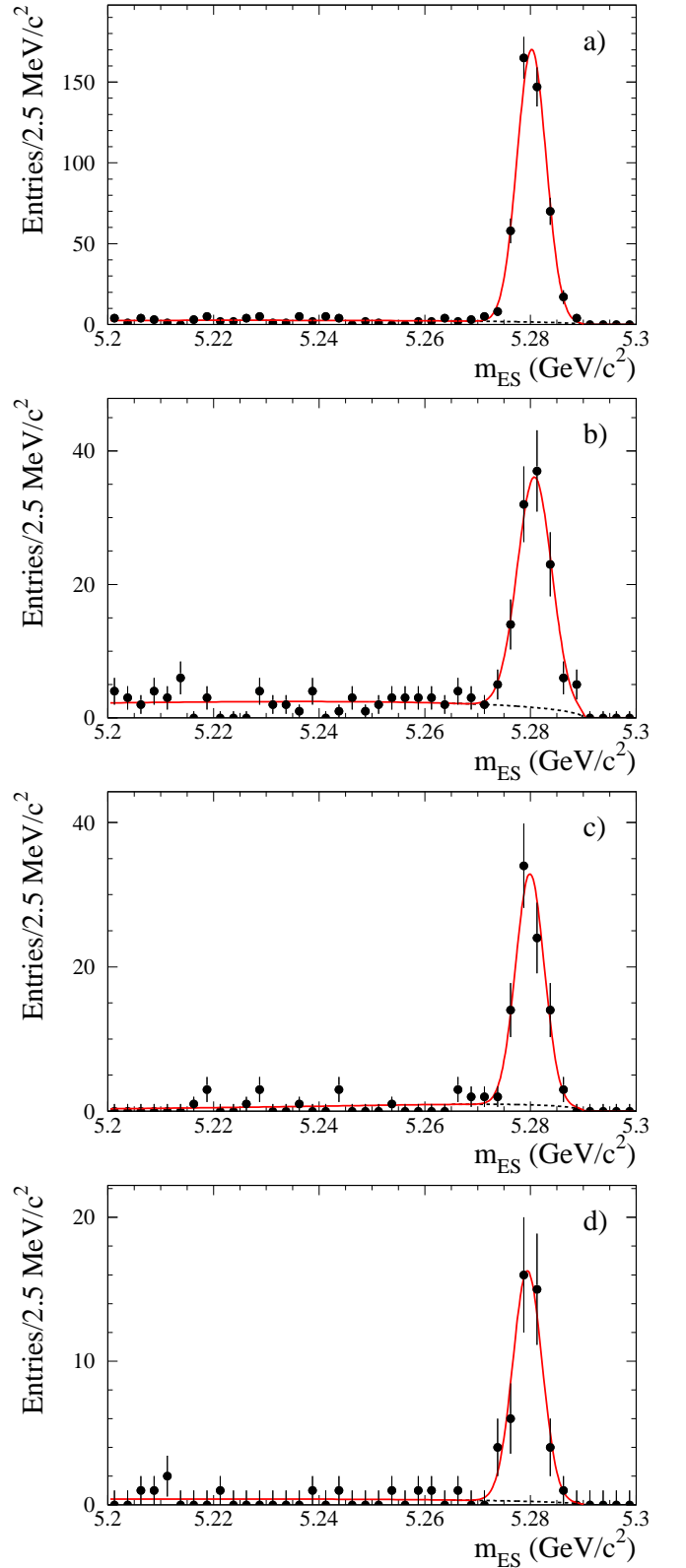


FIG. 5: Candidates for  $B^0 \rightarrow J/\psi K_S^0$  where  $K_S^0$  decays to a)  $\pi^+\pi^-$  or b)  $\pi^0\pi^0$ ; Candidates for c)  $B^0 \rightarrow \psi(2S)K_S^0$  and d)  $B^0 \rightarrow \chi_{c1}K_S^0$  ( $K_S^0 \rightarrow \pi^+\pi^-$ ). Overlaid in each case is the result of a fit with a Gaussian distribution for the signal and an ARGUS function for the background.

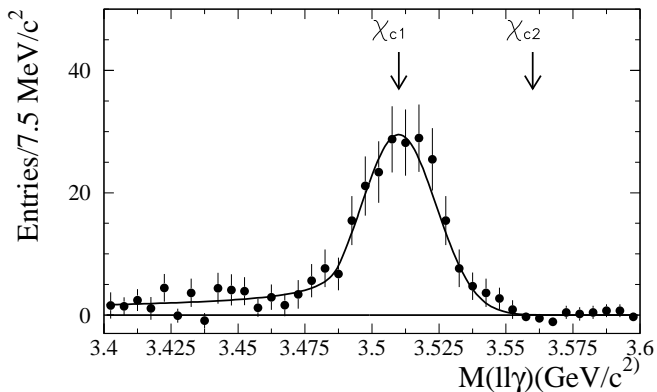


FIG. 6: Distribution of  $m(\ell\ell\gamma)$  for the  $\chi_{c1}$  daughters of  $B^+ \rightarrow \chi_{c1}K^+$  and  $B^0 \rightarrow \chi_{c1}K_S^0$  candidates. The expected location of a  $\chi_{c2}$  signal is indicated by the arrow.

combined with  $K^{*0} \rightarrow K_S^0\pi^0$  candidates to form a  $B^0$  candidate. To reduce the combinatorial background, the angle between the flight direction of the  $K_S^0$  and the vector connecting the reconstructed vertices of the  $J/\psi$  and the  $K_S^0$  candidates is required to be less than 200 mrad. Cross-feed background from other  $B \rightarrow J/\psi X$  modes involving a  $\pi^0$  (which includes cross-feed from the  $CP$  mode itself) is suppressed by requiring the cosine of the helicity angle of the  $K^{*0}$  in the  $B^0$  meson rest frame to be smaller than 0.95. Further details of the selection and analysis of this sample can be found in Ref. [13].

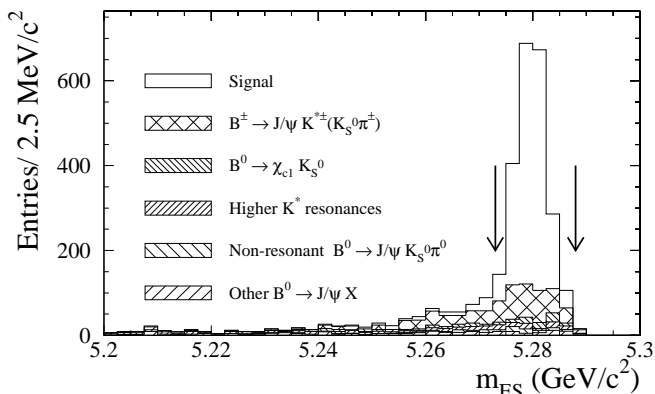


FIG. 7: Distribution of  $m_{ES}$  for selected  $J/\psi K^{*0}$  combinations, where  $K^{*0} \rightarrow K_S^0\pi^0$ . The arrows indicate the region between 5.273 and 5.288  $\text{GeV}/c^2$  that is used to define the sample of  $B^0$  candidates. Monte Carlo estimates of the various background contributions are also indicated.

The  $m_{ES}$  distribution for  $J/\psi K^{*0}$  ( $K^{*0} \rightarrow K_S^0\pi^0$ ) combinations in data is shown in Fig. 7. Given the relatively tight criteria applied in the lepton identification of the daughters of the  $J/\psi$  candidates (see Table IV), the background is dominated by true  $J/\psi$  mesons from  $B$  decays. Its composition can therefore only be estimated

with Monte Carlo simulation and the  $m_{ES}$  distribution is not expected to follow the phase-space form of Eq. 16. Monte Carlo simulation of events with true  $J/\psi$  candidates has been adjusted to match recent results for charmonium branching fractions in  $B$  decays and takes into account the indication of  $S$ -wave  $B^0 \rightarrow J/\psi K_S^0\pi^0$  decays and contributions due to higher  $K^*$  resonances reported in Ref. [13].

As a result, backgrounds are not estimated with a fit to the observed  $m_{ES}$  distribution (Fig. 7), but rather by extrapolation of Monte Carlo background distributions, normalized to the number of produced  $B$  mesons in the data. All  $J/\psi K_S^0\pi^0$  combinations in the range  $5.273 < m_{ES} < 5.288 \text{ GeV}/c^2$  are considered as candidates for this purpose. Estimates of the signal and background contributions in the candidate sample, and the corresponding effective  $CP$ , after acceptance correction for the signal selection, is provided in Table V, while the signal yields and purities in data are listed in Table III. The dominant source of cross-feed background, with zero effective  $CP$ , is  $B^+ \rightarrow J/\psi K^{*+}$  ( $K^{*+} \rightarrow K_S^0\pi^+$ ), where the daughter  $\pi^+$  is exchanged for a background  $\pi^0$ .

TABLE V: Signal and background estimates for the selected  $B^0 \rightarrow J/\psi K^{*0}$  ( $K^{*0} \rightarrow K_S^0\pi^0$ ) sample. All the events within the range  $5.273 < m_{ES} < 5.288 \text{ GeV}/c^2$  are considered as  $B^0$  candidates and the background contributions are estimated with Monte Carlo simulation. The quoted errors are derived from conservative bound on the branching fractions and represent the size of the variation used to estimate the systematic error on  $\sin 2\beta$  due to backgrounds.

Event type	Fraction (%)	Effective $CP$
Signal	$73.6 \pm 7.4$	$+0.65 \pm 0.07$
$B^+ \rightarrow J/\psi K^{*+} (K_S^0\pi^+)$	$17.4 \pm 1.7$	0
$B^0 \rightarrow \chi_{c1} K_S^0$	$2.4 \pm 0.7$	-1
Higher $K^*$ resonances	$2.6 \pm 1.3$	$0 \pm 1$
Non-resonant $B^0 \rightarrow J/\psi K_S^0\pi^0$	$1.8 \pm 0.9$	$0 \pm 1$
Other $B^0 \rightarrow J/\psi X$	$2.4 \pm 1.2$	$0 \pm 1$
Non $B \rightarrow J/\psi X$	0	0

#### D. $B^0$ decays to the $CP$ mode $J/\psi K_L^0$

Candidates for the  $B_{CP}$  sample in the mode  $B^0 \rightarrow J/\psi K_L^0$  are obtained by combining mass-constrained  $J/\psi$  and  $K_L^0$  candidates, following the methods in Ref. [24]. The  $J/\psi$  candidates are required to have a momentum in the  $\Upsilon(4S)$  frame between 1.4 and 2.0  $\text{GeV}/c$ . As the  $K_L^0$  energy is not well measured by the EMC or IFR detectors, the laboratory momentum of the  $K_L^0$  is determined by its flight direction as measured from the EMC or IFR cluster and the constraint that the invariant mass of the  $J/\psi K_L^0$  system has the known  $B^0$  mass. The production angle  $\theta_B$  of a  $B$  meson with respect to the  $z$  axis in the  $\Upsilon(4S)$  frame follows a  $\sin^2\theta_B$  distribution. We require that  $|\cos\theta_B| < 0.9$ . The  $J/\psi$  helicity angle is required to satisfy  $|\cos\theta_h| < 0.9$  and the sum of

TABLE VI: Monte Carlo prediction for the composition of background channels containing a true  $J/\psi$  that pass the  $B^0 \rightarrow J/\psi K_L^0$  selection criteria. Events are required to have  $|\Delta E| < 10$  MeV. The quoted errors are derived from conservative bound on the branching fractions and represent the size of the variation used to estimate the systematic error on  $\sin 2\beta$  due to backgrounds.

Event type	EMC (%)	IFR (%)	Effective $CP$
$B^0 \rightarrow J/\psi K^{*0}(K_L^0\pi^0)$	$23 \pm 3$	$26 \pm 3$	$-0.68 \pm 0.07$
$B^+ \rightarrow J/\psi K^{*\pm}(K_L^0\pi^\pm)$	$28 \pm 4$	$45 \pm 6$	0
$B^0 \rightarrow J/\psi K_S^0$	$13 \pm 2$	$2 \pm 1$	-1
$B^0 \rightarrow \chi_{c1} K_L^0$	$3 \pm 1$	$5 \pm 1$	+1
$B \rightarrow J/\psi K_L^0\pi$	$1_{-1}^{+2}$	$1_{-1}^{+2}$	0
Other $B^0 \rightarrow J/\psi X$	$32 \pm 16$	$21 \pm 10$	$0 \pm 0.25$

$|\cos\theta_B|$  and  $|\cos\theta_h|$  must be less than 1.3. Events with a reconstructed charged or neutral  $B$  decay to  $J/\psi K_S^0$  ( $K_S^0 \rightarrow \pi^+\pi^-$  or  $\pi^0\pi^0$ ),  $J/\psi K^{*0}$  ( $K^{*0} \rightarrow K^+\pi^-$  or  $K_S^0\pi^0$ ),  $J/\psi K^+$ , or  $J/\psi K^{*+}$  ( $K^{*+} \rightarrow K_S^0\pi^+$  or  $K^+\pi^0$ ) are explicitly removed. The total missing transverse momentum projected along the  $K_L^0$  direction, where the total momentum is calculated with all charged tracks and neutral clusters (without the  $K_L^0$ ), must be no more than 0.25 (0.40) GeV/ $c$  lower than the calculated  $K_L^0$  transverse momentum for EMC (IFR)  $K_L^0$  candidates.

Events where multiple  $J/\psi K_L^0$  combinations with  $\Delta E < 80$  MeV satisfy these requirements are treated as a special case. A hierarchy is imposed where the highest energy EMC cluster for multiple EMC combinations, or the IFR cluster with the largest number of layers for multiple IFR combinations is selected. In cases where there are both an EMC and IFR combination, the EMC combination is selected because it is expected to have better angular resolution. Although the EMC information is used, such events are counted as IFR events, since they have the same relatively high signal purity.

TABLE VII: Results of the binned likelihood fit to the full  $\Delta E$  distribution of the  $B^0 \rightarrow J/\psi K_L^0$  combinations. All signal yields and background estimates are reported for the  $B_{CP}$  candidate range  $|\Delta E| < 10$  MeV.

	$K_L^0$ reconstruction type		
	EMC & IFR	EMC	IFR
Data events	427	228	199
Signal	$257 \pm 24$	$128 \pm 17$	$129 \pm 17$
$J/\psi X$ bkgd	$154 \pm 15$	$89 \pm 11$	$65 \pm 10$
non- $J/\psi$ bkgd	$19 \pm 2$	$14 \pm 2$	$5 \pm 1$
Signal fraction	$0.60 \pm 0.04$	$0.56 \pm 0.05$	$0.65 \pm 0.05$

The difference  $\Delta E$  between the energy of the  $J/\psi K_L^0$  system and the beam energy in the  $\Upsilon(4S)$  frame is used to discriminate between signal and backgrounds. The  $\Delta E$  distribution of selected  $B^0 \rightarrow J/\psi K_L^0$  combinations for the  $\Upsilon(4S)$  data is shown in Fig. 8. Signal events are peaked within  $\pm 10$  MeV of  $\Delta E = 0$  while background

events extend towards positive values of  $\Delta E$ . The small signal width and the asymmetric distribution of the background in comparison with the  $K_S^0$  modes are both consequences of the mass constraint used to determine the  $K_L^0$  momentum.

The purity of the  $B^0 \rightarrow J/\psi K_L^0$  sample is the lowest of the  $CP$  modes (60%). Irreducible backgrounds are dominantly from  $B \rightarrow J/\psi K_L^0 X$  modes, which cannot be distinguished from signal due to imposition of the  $m_B$  mass constraint in determining the momentum of the  $K_L^0$  candidate. The largest single background contribution is from  $B \rightarrow J/\psi K^*$ , where the  $K^*$  decays to  $K_L^0\pi$ . This mode and backgrounds from other  $B \rightarrow J/\psi X$  decays are studied with Monte Carlo simulation. The composition of the events that are included in the  $J/\psi K_L^0$  sample is given in Table VI. The effective  $CP$ , after acceptance correction for the signal selection, is also provided. The additional background from events with a misreconstructed  $J/\psi \rightarrow \ell\ell$  candidate is studied with the  $m(\ell\ell)$  sidebands.

A binned likelihood fit to the  $\Delta E$  distribution is performed separately for the EMC and IFR categories to determine the composition of the  $B^0 \rightarrow J/\psi K_L^0$  sample. There are three fit components: the fraction of the data that is signal, the number of  $B \rightarrow J/\psi X$  background events, and the number of non- $J/\psi$  background events. The  $\Delta E$  shapes for the signal and the  $J/\psi X$  background are determined from Monte Carlo simulation. The  $\Delta E$  shape of the non- $J/\psi$  component is taken from the  $m(\ell\ell)$  sideband in the data. A Poisson term, with mean given by the expected number of non- $J/\psi$  events in the  $m(\ell\ell)$  signal region, is included in the likelihood to constrain the normalization of the non- $J/\psi$  component. The result of the fit is shown in Fig. 8, and the corresponding signal and background fractions are reported in Table VII for the  $B^0 \rightarrow J/\psi K_L^0$  combinations that are selected as  $B_{CP}$  candidates in the interval  $|\Delta E| < 10$  MeV. As expected from Monte Carlo studies, the purity of the IFR sample is significantly better than the EMC sample, mainly because the  $B^0 \rightarrow J/\psi K_S^0$  ( $K_S^0 \rightarrow \pi^0\pi^0$ ) background is significantly larger in the EMC sample. Since the purities of the two subsamples are quite different, we obtain better statistical sensitivity in the  $\sin 2\beta$  fit by treating the EMC and IFR categories separately.

## E. Semileptonic $B^0$ decays

The semileptonic decay  $B^0 \rightarrow D^{*-}\ell^+\nu$ , with a measured branching fraction of  $(4.60 \pm 0.27)\%$  [11], is potentially a copious source of reconstructed  $B^0$  mesons. However, since the neutrino cannot be detected, the background levels in selected samples are generally larger and more difficult to characterize. Likewise, the  $\Delta z$  determination cannot take advantage of the beam spot and reconstructed  $B^0$  direction. As a consequence, we use a large sample of  $D^{*-}\ell^+\bar{\nu}$  candidates only as a cross check on our determination of the mistag rates from the time structure of the  $B_{\text{flav}}$  and  $B_{CP}$  events. The selection

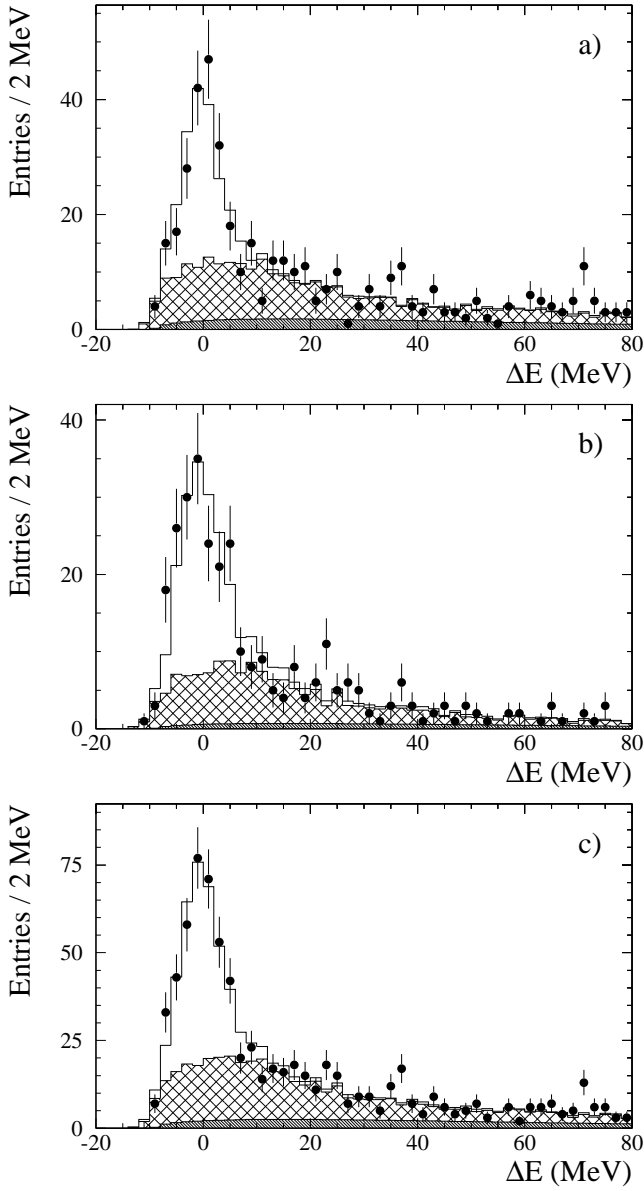


FIG. 8: Distribution of  $\Delta E$  for selected  $B^0 \rightarrow J/\psi K_L^0$  combinations where the  $K_L^0$  is identified a) in the EMC, b) in the IFR, or c) either subsample combined. The points with error bars are the data. The open histogram is the result of a three-component binned likelihood fit, where the three components are signal (open), inclusive  $J/\psi$  background (cross hatched), and non- $J/\psi$  combinatorial background (dark shading). The shapes of the signal and inclusive  $J/\psi$  background are taken from Monte Carlo. The shape of the non- $J/\psi$  combinatorial background is taken from the  $m(\ell\ell)$  sideband in data. Candidates for the  $B_{CP}$  sample are selected in the region  $|\Delta E| < 10$  MeV.

criteria for this control sample and the characterization of backgrounds is described here, while the analysis of the mistag rates is reported in Section VIII C 4. The semileptonic  $B^0$  sample is obtained by reconstructing the

$D^{*-}$  through its decay to  $\bar{D}^0\pi^-$ , where the three decay modes  $K^+\pi^-$ ,  $K^+\pi^+\pi^-\pi^-$  and  $K^+\pi^-\pi^0$  are used to reconstruct the  $\bar{D}^0$ .

### 1. Event selection

All reconstructed  $\bar{D}^0$  candidates are required to have an invariant mass within  $\pm 2.5\sigma$  of the nominal  $D^0$  mass, based on the observed RMS width of the signal. A vertex fit to the  $\bar{D}^0$  candidate is required to have a  $\chi^2$  probability greater than 0.001. There are no additional requirements for  $\bar{D}^0 \rightarrow K^+\pi^-$ . For  $\bar{D}^0 \rightarrow K^+\pi^+\pi^-\pi^-$  and  $\bar{D}^0 \rightarrow K^+\pi^-\pi^0$  we require a **VeryLoose** kaon and a **Loose** pion particle identification as described in Section II D, and a minimum  $\pi^0$  momentum of 200 MeV/c in the laboratory frame. In addition, the  $K$  and  $\pi$  candidates are required to have momenta greater than 200 and 150 MeV/c, respectively, for the mode  $\bar{D}^0 \rightarrow K^+\pi^+\pi^-\pi^-$ . The decay  $\bar{D}^0 \rightarrow K^+\pi^-\pi^0$  occurs mostly through quasi-two-body channels. The  $\rho$  and  $K^*$  resonances dominate and we use weights calculated from the Dalitz-plot position for each candidate [26] to construct a probability per  $D^0$  and select events using this quantity as a way of suppressing combinatorial background.

$\bar{D}^0$  candidates satisfying these requirements are combined with all charged tracks with a minimum transverse momentum of 50 MeV/c and charge opposite to that of the kaon from the  $\bar{D}^0$  to form  $D^{*-}$  candidates. The mass difference  $m(\bar{D}^0\pi^-) - m(\bar{D}^0)$  is required to lie within  $\pm 2.5\sigma$  of the nominal value, based on the observed RMS width of the signal.

Finally,  $D^{*-}$  candidates are combined with electron or muon candidates satisfying the **Tight** lepton-identification requirements described in Section II D. The lepton is required to have charge opposite to that of the  $D^{*-}$  and momentum greater than 1.2 GeV/c in the  $\Upsilon(4S)$  frame. A vertex fit to the  $D^{*-}\ell^+$  candidate is required to converge and have a  $\chi^2$  probability greater than 0.01. The  $D^{*-}$  and lepton from a true  $B^0$  decay tend to be back-to-back in the  $B^0$  rest frame, so we require  $\cos\theta_{D^{*-}\ell} < 0$  where  $\theta_{D^{*-}\ell}$  is the angle between the  $D^{*-}$  and the lepton in the  $\Upsilon(4S)$  frame. The cosine of the angle between the thrust axes of the  $(D^{*-}\ell^+)$  pair and the rest of the event is required to satisfy  $|\cos\theta_{\text{th}}| \leq 0.85$ , in order to reduce background from  $e^+e^- \rightarrow c\bar{c}$  events.

The neutrino cannot be reconstructed in the detector, but we can determine whether the missing four-momentum of the candidate is consistent with a particle of zero mass:

$$(p_B - p_{D^{*-}} - p_\ell)^2 = p_\nu^2 = 0. \quad (17)$$

Applying this relation in the  $\Upsilon(4S)$  frame, we obtain a constraint on the angle between the  $B^0$  and the  $D^{*-}\ell^+$  system:

$$\cos\theta_{B-D^{*}\ell} = \frac{m_B^2 + m_{D^{*}\ell}^2 - 2E_B E_{D^{*}\ell}}{2|\mathbf{p}_B||\mathbf{p}_{D^{*}\ell}|}. \quad (18)$$

The energy  $E_B$  and magnitude of the momentum  $|\mathbf{p}_B|$  of the initial-state  $B^0$  are known in the  $\mathcal{T}(4S)$  frame from the boosted beam energies. The energy  $E_{D^*\ell}$ , the magnitude of the momentum  $|\mathbf{p}_{D^*\ell}|$ , and the invariant mass  $m_{D^*\ell}$  of the  $D^{*-}\ell^+$  system are obtained from the four-momenta of the  $D^{*-}$  and the lepton. The cosine of the angle  $\cos\theta_{B-D^*\ell}$  should lie in the physical region  $[-1, +1]$  for true  $D^{*-}\ell^+\bar{\nu}$  events. Allowing for detector resolution effects in the reconstructed momenta and angles, we require  $|\cos\theta_{B-D^*\ell}| < 1.1$ .

After applying these selection criteria, we obtain a sample of about 37500  $B^0 \rightarrow D^{*-}\ell^+\bar{\nu}$  candidates. The  $\cos\theta_{B-D^*\ell}$  distribution of these candidates is shown in Fig. 9.

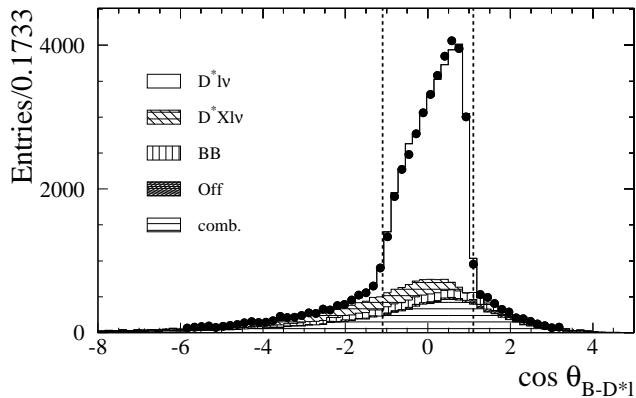


FIG. 9: Extraction of  $B\bar{B}$  and  $D^{**}$  backgrounds from the data. The points show the  $\cos\theta_{B-D^*\ell}$  distribution for the reconstructed signal. The histogram shows the result of the fit described in the text. The different background contributions are indicated by the various hatchings.

## 2. Sample composition

The final sample contains a fraction  $f_{\text{sig}}$  of  $B^0 \rightarrow D^{*-}\ell^+\bar{\nu}$  signal events, as well as fractions  $f_{\text{comb}}$  of  $D^{*-}$  combinatorial background,  $f_{\text{off}}$  of continuum background (a true  $D^{*-}$  and an identified lepton),  $f_{B^+ \rightarrow D^*X\ell\bar{\nu}}$  of  $B \rightarrow D^*\pi\ell\bar{\nu}$  events, where the  $D^*\pi$  can come from a radially or orbitally-excited  $L = 1$  state or non-resonant decay, and finally  $f_{B\bar{B}}$  of background from  $B\bar{B}$  events with a true  $D^{*-}$  and an identified lepton ( $B\bar{B} \rightarrow D^*Y\ell$ ). Examples in this last category are cases where the  $D^{*-}$  and the lepton come from two different  $B$  mesons or where the lepton and the  $D^{*-}$  are from the same  $B$  but the lepton is produced in a charm decay.

The combinatorial and continuum backgrounds can be extracted directly from the data. The former is determined with the  $m(\bar{D}^0\pi^-) - m(\bar{D}^0)$  distribution itself. The latter is estimated with the off-resonance data sample, weighted by the ratio of the relative integrated luminosities for on- and off-resonance data. The remaining three contributions can be distinguished by their dif-

ferent distributions in  $\cos\theta_{B-D^*\ell}$ . The  $B^0 \rightarrow D^{*-}\ell^+\bar{\nu}$  signal events are expected to lie in the region  $-1 < \cos\theta_{B-D^*\ell} < 1$ , while contributions from  $B \rightarrow D^*\pi\ell\bar{\nu}$  semileptonic decay, due to missing particles, must extend below the kinematic threshold  $\cos\theta_{B-D^*\ell} < -1$ . Finally,  $B\bar{B}$  background events populate the full  $\cos\theta_{B-D^*\ell}$  distribution. Thus, the region  $\cos\theta_{B-D^*\ell} > 1$  contains mainly  $B\bar{B}$  background, while the region  $\cos\theta_{B-D^*\ell} < -1$  is mostly populated by  $B \rightarrow D^*\pi\ell\bar{\nu}$ . The shape of the  $\cos\theta_{B-D^*\ell}$  distributions for these three components is obtained from Monte Carlo simulation and a fit to the full  $\cos\theta_{B-D^*\ell}$  range is used to determine the two background fractions in the signal region.

The orbitally-excited resonances that can decay to  $D^*\pi$  are the two narrow states  $D_1, D_2^*$  (observed with masses around 2420 and 2460 MeV/ $c^2$ ) and the broad state  $D_1^*$  (not yet seen, but with mass expected to be about 2420 MeV/ $c^2$  and  $\Gamma \geq 250$  MeV). Contributions from  $B \rightarrow D^*X\ell\bar{\nu}$  decays with more than one pion are expected to be small and are more easily separated from the signal with  $\cos\theta_{B-D^*\ell}$ . Isospin symmetry requires that the charged  $B$  contribution be 2/3 of the total  $D^{*-}\pi$  pairs from  $B \rightarrow D^*\pi\ell\bar{\nu}$  decays, either from orbitally-excited states or non-resonant decays. The  $\cos\theta_{B-D^*\ell}$  distribution obtained from Monte Carlo simulation for the different channels is modeled with a general function that is sufficiently flexible to describe both individual channels as well as a superposition of excited charm modes.

After subtraction of continuum and combinatorial backgrounds, a fit is performed to the resulting  $\cos\theta_{B-D^*\ell}$  distribution over the full observed range  $[-8, +5]$ . However, it is only the relative fraction of the various backgrounds in the signal window  $\cos\theta_{B-D^*\ell} \in [-1.1, 1.1]$  that we require. Furthermore, in the case of  $D^{**}$ , only the charged  $B$  contribution is a background for the measurement of the mistag fraction and is assumed to be 2/3 of the total  $D^{**}$  contribution. The fitted fractions are defined by:

$$g_{**} = N(B^+ \rightarrow D^*X\ell\bar{\nu})/[N(B^0 \rightarrow D^{*-}\ell^+\bar{\nu}) + N(B^0 \rightarrow D^*X\ell^+\bar{\nu}) + N(B^+ \rightarrow D^*X\ell\bar{\nu})]$$

$$g_{BB} = N(B\bar{B} \rightarrow D^*Y\ell)/[N(B^0 \rightarrow D^{*-}\ell^+\bar{\nu}) + N(B^0 \rightarrow D^*X\ell^+\bar{\nu}) + N(B\bar{B} \rightarrow D^*Y\ell)] \quad (19)$$

where the  $N$  is the number of events from a given process that survives the selection requirements.

The result of the fit to the full untagged sample is shown in Fig. 9, along with the Monte Carlo model for the  $D^{**}$  component. The  $\chi^2$  of the fit in the full  $\cos\theta_{B-D^*\ell}$  range is 82 for 69 degrees of freedom. The fitted contributions are  $g_{**} = (4.5 \pm 0.3 \pm 2.2)\%$  and  $g_{BB} = (4.8 \pm 0.4 \pm 2.2)\%$ , where the first error is statistical and the second systematic. To estimate the systematic error on these fractions, three extreme assumptions have been made concerning the  $B \rightarrow D^*X\ell\bar{\nu}$  background: all narrow  $D^{**}$  states, all broad  $D^{**}$  states, or all non-resonant decays. The largest deviation comes from

the non-resonant model. Another source of systematic uncertainty is the assumed form for the  $\cos\theta_{B-D^*\ell}$  distributions in the Monte Carlo simulation. The contribution from this effect has been estimated by incorporating a 30% fraction with a uniform distribution.

The absolute background fractions in the untagged sample are given in Table VIII, where the uncertainties include both statistical and systematic contributions.

The sum of the fractions of signal and background contributions is constrained to unity. On this basis the signal component is found to be  $f_{\text{sig}} = (78 \pm 4)\%$  leading to an estimated yield of  $29042 \pm 1500 B^0 \rightarrow D^{*-}\ell^+\bar{\nu}$  signal events.

TABLE VIII: Sample composition in data as determined from fits to the  $\cos\theta_{B-D^*\ell}$  distributions. The fractions have been computed without a requiring tagging information. The dominant errors are systematic except for  $f_{c\bar{\nu}}$ , which is limited by the statistics.

$f_{\text{comb}}$	$f_{\text{off}}$	$f_{B\bar{B}}$	$f_{B^+ \rightarrow D^* X \ell \bar{\nu}}$
$0.139 \pm 0.028$	$0.008 \pm 0.002$	$0.039 \pm 0.018$	$0.037 \pm 0.018$

#### IV. FLAVOR TAGGING

After the daughter tracks of the reconstructed  $B$  are removed, the remaining tracks are analyzed to determine the flavor of the  $B_{\text{tag}}$ , and this ensemble is assigned a tag flavor, either  $B^0$  or  $\bar{B}^0$ .

We use four different types of flavor tag, or tagging categories, in this analysis. The first two tagging categories rely upon the presence of a prompt lepton, or one or more charged kaons in the event. The next two categories exploit a variety of inputs with a neural-network algorithm. These tagging categories are hierarchical and mutually exclusive.

To quantify the discriminating power of each tagging category, we use as a figure of merit the effective tagging efficiency  $Q_i = \epsilon_i (1 - 2w_i)^2$ , where  $\epsilon_i$  is the fraction of events associated to the tagging category  $i$  and  $w_i$  is the mistag fraction, the probability of incorrectly assigning the tag to an event in this category. The statistical errors in the measurements of  $\sin 2\beta$  and  $\Delta m_d$  are inversely proportional to  $\sqrt{\sum_i Q_i}$ .

The mistag fractions are measured with the  $B_{\text{flav}}$  data sample. The results are shown in Section VII. The performance of the tagging algorithm,  $\sqrt{\sum_i Q_i}$ , was optimized and the neural networks were trained with Monte Carlo simulations only. Differences between the tagging inputs in data and in simulation may make the actual tagging algorithm somewhat non-optimal, but would not lead to a bias because the wrong-tag fractions  $w_i$  are measured directly with data, both for the mixing and  $CP$ -violation measurements.

#### A. Lepton and kaon tags

The **Lepton** and **Kaon** tagging categories use the correlation between the flavor of the decaying  $b$  quark and the charge of a primary lepton from a semileptonic decay or the charge of a kaon from the chain  $b \rightarrow c \rightarrow s$ .

For the **Lepton** category we use both electrons and muons, which are required to pass the **VeryTight** and **Tight** selection, respectively (see Tables I and II). A minimum requirement of 1.0 (1.1) GeV/ $c$  on the electron (muon) center-of-mass momentum is applied to reduce the contamination from softer, opposite-sign leptons coming from cascade semileptonic decays of charm mesons. The center-of-mass momentum spectra for electrons and muons are compared to simulation in Fig. 10 for the  $B_{\text{flav}}$  sample, after background subtraction based on the  $m_{\text{ES}}$  sideband events. In each event, the electron or muon with the greatest center-of-mass momentum is used for flavor tagging; for the tiny fraction of events with both an electron and muon, the electron is used due to its smaller misidentification rate.

The kaon content of the event is evaluated by taking the sum of the charges of all kaons identified with a neural network algorithm (K subnet described below in Section IV B). The kaon identification algorithm has been set to maximize the effective tagging efficiency  $Q$ . There are 0.8 charged kaons per  $B$  decay, and roughly 15% of these have the wrong sign (e.g.  $K^-$  from  $B^0$ , rather than the expected  $K^+$ ). Wrong-sign kaons occur primarily in  $B$  decays to a charmed-anti-charmed pair of mesons. The momentum distributions are quite similar for right- and wrong-sign kaons; we find no kinematic quantity that distinguishes between them. The center-of-mass momentum spectrum for charged kaons and the distribution of charged kaon multiplicity are shown in Fig. 11 for the  $B_{\text{flav}}$  sample.

An event with an identified high-momentum lepton is assigned to the **Lepton** category unless the sum of the charges of any kaons present has the opposite sign. Next, events are assigned to the **Kaon** category if the sum of the kaon charges is non-zero. The charge of the lepton or sum of kaon charges is used to assign the flavor of the  $B_{\text{tag}}$ . All remaining events, approximately 55% of the total including those with inconsistent lepton and kaon charge (0.5% of all events in simulation) and those with two oppositely-charged kaons (4.6% of all events in simulation), are passed to the neural-network-based categories.

#### B. Neural-network tags

Besides identified high-momentum leptons and charged kaons, there are other features that can be used to determine the flavor of the  $B_{\text{tag}}$ , although not as easily or cleanly distinguishing. These include soft pions from  $D^*$  decays, high-momentum primary leptons that are not selected by the electron or muon identification algorithms,

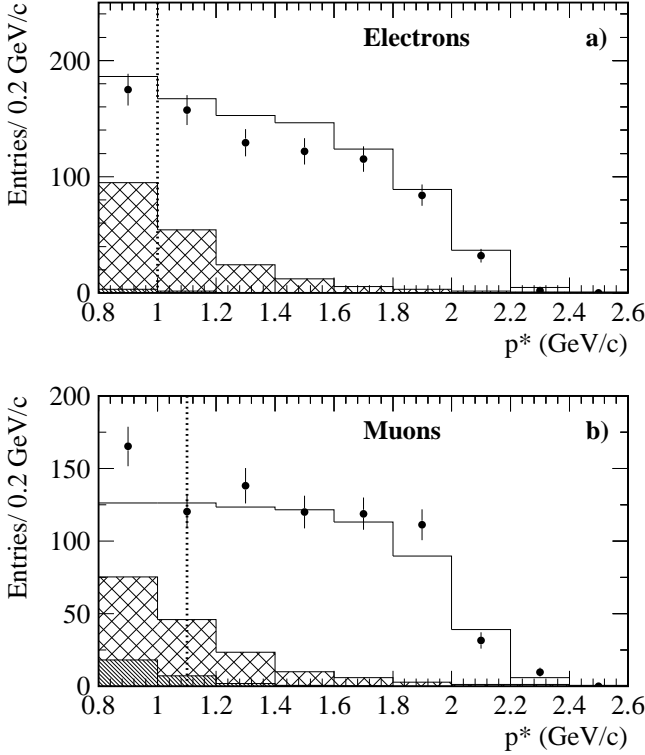


FIG. 10: Center-of-mass momentum distribution for a) electrons and b) muons. Data from the  $B_{\text{flav}}$  sample, after background subtraction based on the  $m_{\text{ES}}$  sideband, are shown as points. The open histogram shows primary leptons, the cross-hatched histogram cascade leptons, and the diagonally-hatched histogram fake leptons, all from simulation. The simulation is normalized, with a residual overall systematic error of 5%, to the total number of  $B^0$  decays in data after background subtraction, not to the number of observed leptons. The vertical lines at 1.0 GeV/c for electrons and 1.1 GeV/c for muons indicate the requirement on center-of-mass momentum for the **Lepton** category.

lower-momentum primary leptons, and charged kaons that are not selected by the kaon identification algorithm. These sources are combined with a multivariate method; we use a sequence of neural networks to flavor-tag those events not assigned to the **Lepton** or **Kaon** categories.

Three different track-based neural networks, called “subnets”, are trained, each with a specific goal. The L, K, and **SoftPi** subnets are sensitive to the presence of primary leptons, charged kaons and soft pions from  $D^*$  decays, respectively. Each subnet is applied to all tracks from the  $B_{\text{tag}}$ .

The L subnet uses the binary output of the electron and muon identification algorithms on the input track, the center-of-mass momentum of the input track, and a pair of kinematic variables,  $E_W^{90}$  and  $\cos\theta_{l\nu}$ , that separate primary leptons from cascade leptons and other tracks.

The isolation variable,  $E_W^{90}$ , is given by the sum of the energies of all tracks within  $90^\circ$  of the  $W$  direction. The

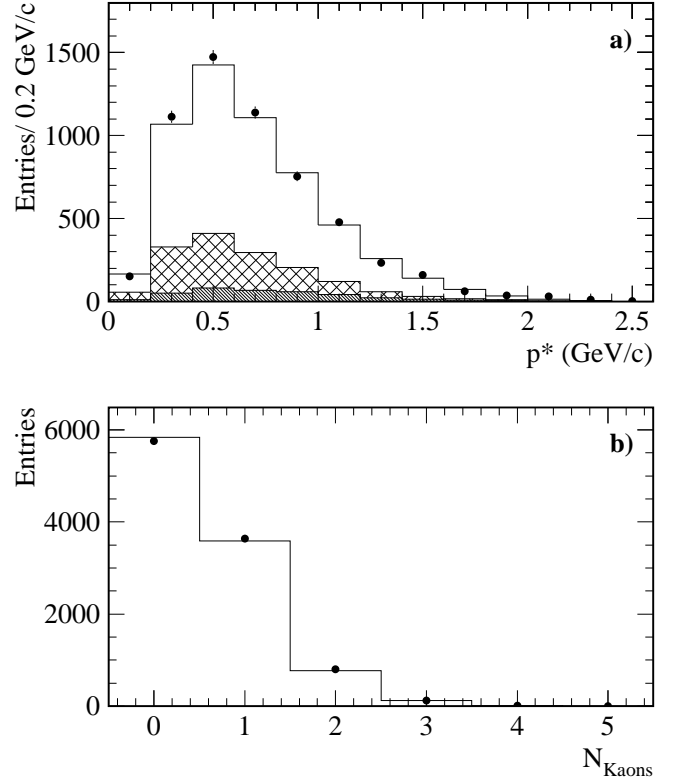


FIG. 11: a) Center-of-mass momentum distribution for kaons and b) kaon multiplicity per event. Data from the  $B_{\text{flav}}$  sample, after background subtraction based on the  $m_{\text{ES}}$  sideband, are shown as points. The histograms are from simulation. In a), the diagonally-hatched histogram is from fake kaons, the cross-hatched histogram is from kaons that have the wrong-sign charge, and the open histogram is from kaons with the right-sign charge, all from simulation. The simulation is normalized to the total number of  $B^0$  flavor candidates after background subtraction, not to the number of observed kaons.

$W$  momentum is inferred as the sum of the input track momentum and the neutrino momentum, which we take to be the missing momentum in the center-of-mass frame using all charged tracks in the  $B_{\text{tag}}$ . This variable is effective because in a semileptonic decay the hadrons recoiling against the virtual  $W$  would generally go off in the opposite direction.

The other kinematic variable used,  $\cos\theta_{l\nu}$ , is the cosine of the angle between the input track and the neutrino direction. The distributions in the  $B_{\text{flav}}$  sample and simulation of  $E_W^{90}$  and  $\cos\theta_{l\nu}$  are shown in Fig. 12a and b, for all events not in the **Lepton** or **Kaon** category. The corresponding distribution of the L subnet output is shown in Fig. 13a.

The K subnet uses the input track momentum in the laboratory frame, together with the three relative likelihoods  $\mathcal{L}_K/(\mathcal{L}_\pi + \mathcal{L}_K)$  for the SVT, the DCH and the DIRC. The SVT and DCH likelihoods are derived from  $dE/dx$  measurements, and the DIRC likelihood is calcu-



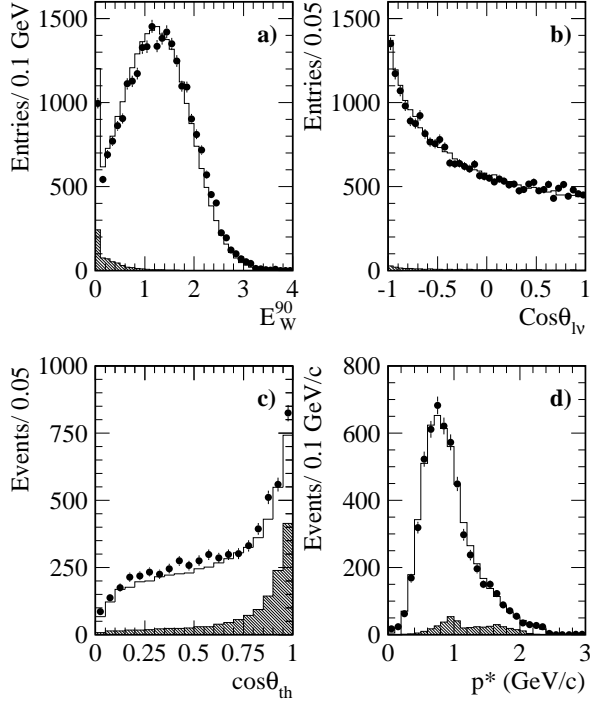


FIG. 12: Inputs to the subnets: a)  $E_W^{90}$ , b)  $\cos\theta_{IV}$ , c)  $\cos\theta_{th}$  for low center-of-mass momentum tracks ( $p^* < 0.18$  GeV/c), and d) the center-of-mass momentum for all tracks. The points are data from the  $B_{flav}$  sample after background subtraction based on the  $m_{ES}$  sideband, and the histogram is simulation. For  $\cos\theta_{th}$  the diagonally-hatched histogram shows the contribution from soft- $\pi$  coming from  $D^*$  decays, and for the other distributions shows the component from primary leptons. The simulation is normalized to the total number of  $B^0$  flavor candidates after the background subtraction.

lated from a global fit to the number of photons detected, their positions and arrival times relative to the corresponding track. The distribution of the K subnet output, again for events not in the Lepton or Kaon category, is shown in Fig. 13b.

The **SoftPi** subnet uses the center-of-mass momentum of the input track, the cosine of the angle of the input track with the thrust axis  $\cos\theta_{th}$ , and the center-of-mass momentum of the minimum momentum track. The thrust axis is determined from all charged tracks and neutral clusters in the  $B_{tag}$ . The direction of any  $D^*$  in the decay of the  $B_{tag}$  is approximated by the direction of the thrust axis. Thus soft pions from  $D^*$  decays, which are aligned with the  $D^*$  direction in the center-of-mass frame, tend to be correlated with the thrust axis. The distribution of  $\cos\theta_{th}$  is shown for low center-of-mass momentum tracks in Fig. 12c, comparing the  $B_{flav}$  sample with simulation for all events not in the **Lepton** or **Kaon** category. The corresponding distribution of the **SoftPi** subnet output is shown in Fig. 13c.

The outputs of the three subnets are among the inputs to a final neural network, which is trained to distinguish

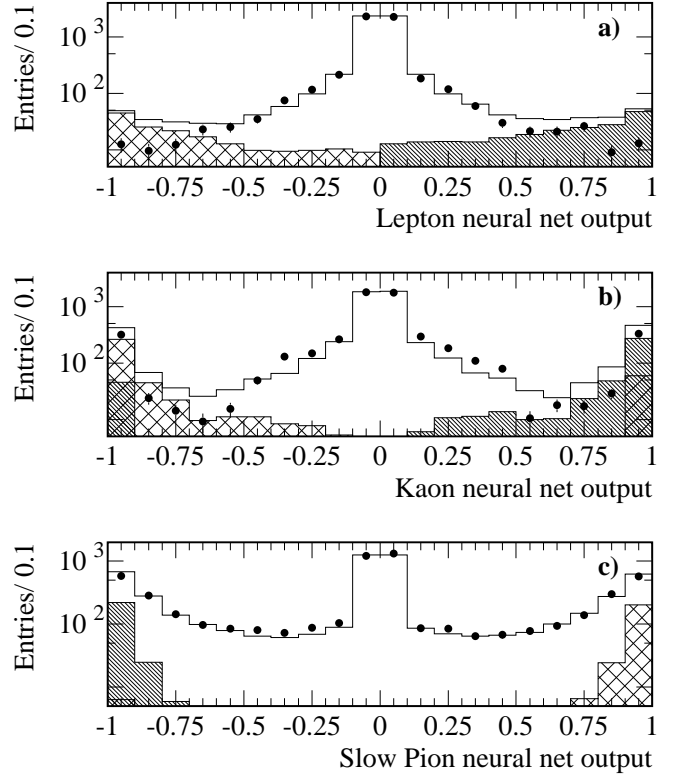


FIG. 13: Output of the subnets for events not assigned to the **Lepton** or **Kaon** categories: a) L subnet, b) K subnet, and c) **SoftPi** subnet. The points are data from the  $B_{flav}$  sample after background subtraction based on the  $m_{ES}$  sideband, and the histogram is simulation. For each distribution, the filled portion of the histogram shows the component with a  $B^0$  (singly-hatched) or  $\bar{B}^0$  (cross-hatched) tag from the full neural network algorithm that arises from true primary leptons, kaons, or soft-pions respectively. Note that the latter has the opposite charge correlation with the  $B^0$  tag. The simulation is normalized to the total number of  $B^0$  flavor candidates after background subtraction.

between  $B^0$  and  $\bar{B}^0$ . The variables used as inputs to the final network include the maximal values of the L and **SoftPi** subnet outputs, each multiplied by the charge of the corresponding input track, and the highest and the second-highest values of the K subnet output again multiplied by the charge of the corresponding input tracks. The two other inputs to the final neural network are the center-of-mass momentum of the maximum momentum track multiplied by its charge, and the number of tracks with significant impact parameters. The latter is an indicator of the presence of  $K_s^0$  mesons. The distribution of the center-of-mass momentum for all tracks is shown in Fig. 12d.

The output from the final neural network,  $x_{NT}$ , is mapped onto the interval  $[-1, 1]$ . The assigned flavor tag is  $B^0$  if  $x_{NT}$  is negative, and  $\bar{B}^0$  otherwise. Events with  $|x_{NT}| > 0.5$  are assigned to the NT1 tagging category and

events with  $0.2 < |x_{NT}| < 0.5$  to the NT2 tagging category. Events with  $|x_{NT}| < 0.2$ , approximately 30% of the total, have very little tagging power and are rejected. The distribution of  $x_{NT}$  for all events not assigned to the **Lepton** or **Kaon** category is shown in Fig. 14a.

Most of the separation between  $B^0$  and  $\bar{B}^0$  in the NT1 and NT2 tagging categories derives from primary leptons that are not identified as electrons or muons and from soft pions from  $D^*$  decays. Simulation studies indicate that roughly 37% of the effective tagging efficiency  $Q$  is due to events with unidentified primary leptons, 28% is due to events with a soft pion, a further 11% from events with a lower momentum primary lepton, and the remainder from a mixture of the various inputs. This classification is shown for the NT1 and NT2 categories in Fig. 14b for a simulation of  $B^0$  decays. The modest disagreements between Monte Carlo simulation and data that are evident in the distributions of the subnet output variables shown in Fig. 13 lead to a difference in the predicted value of  $Q = (3.0 \pm 0.1)\%$  and  $(1.4 \pm 0.1)\%$  for NT1 and NT2 categories in simulation versus  $(2.5 \pm 0.4)\%$  and  $(1.2 \pm 0.3)\%$  as measured in data.

## V. TIME DIFFERENCE MEASUREMENT

The difference between  $B$  decay times,  $\Delta t = t_{\text{rec}} - t_{\text{tag}}$ , is determined from the measured separation  $\Delta z$  between the vertex of the reconstructed  $B$  meson ( $B_{\text{rec}}$ ) and the vertex of the flavor-tagging  $B$  meson ( $B_{\text{tag}}$ ) along the  $z$  axis. The  $\Delta z$  resolution is dominated by the  $z$  position resolution for the  $B_{\text{tag}}$  vertex.

### A. $\Delta z$ reconstruction

In the reconstruction of the  $B_{\text{rec}}$  vertex, we use all charged daughter tracks. Daughter tracks from  $K_s^0$  and  $D$  candidates are first fit to a separate vertex and the resulting parent momentum and position are used in the fit to the  $B_{\text{rec}}$  vertex. Mass constraints, which include neutral daughters, are used for  $D$  candidates but not for  $D^{*-}$ ,  $J/\psi$  and  $\psi(2S)$  candidates. The RMS resolution in  $z$  for the  $B_{\text{rec}}$  vertex in Monte Carlo simulation is about  $65 \mu\text{m}$  for more than 99% of the  $B$  candidates, and  $40 \mu\text{m}$  for about 80% of the candidates. As described in Section VE, the resolution is about 5% worse in data than in Monte Carlo simulation.

The vertex for the  $B_{\text{tag}}$  decay is constructed from all tracks in the event except the daughters of  $B_{\text{rec}}$ . For fully reconstructed modes, an additional constraint is provided by the calculated  $B_{\text{tag}}$  production point and three-momentum, with its associated error matrix. This is determined from the knowledge of the three momentum of the fully reconstructed  $B_{\text{rec}}$  candidate, its decay vertex and error matrix, and from the knowledge of the average position of the interaction point and the  $\Upsilon(4S)$  average boost (see Fig. 15). These  $B_{\text{tag}}$  parameters are

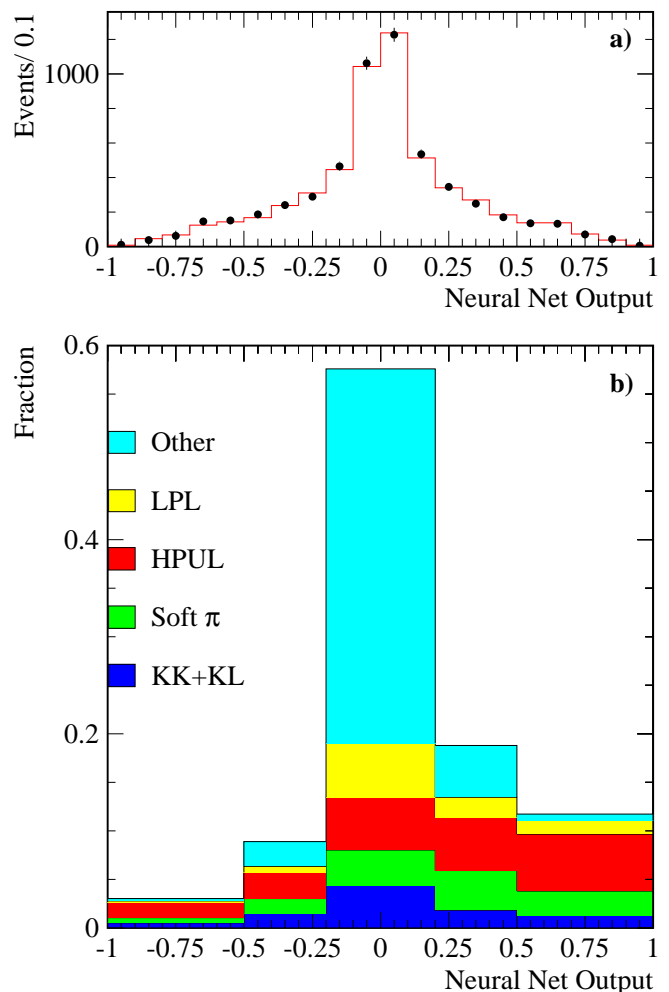


FIG. 14: a) Output of the final neural network for  $B_{\text{flav}}$  events that are not assigned to the **Lepton** or **Kaon** category, where the points are from the  $B_{\text{flav}}$  data after a background subtraction and the histogram is simulation; b) Neural network output from simulation of single  $B^0$  decays with no time evolution, again for events not in the **Lepton** or **Kaon** category. The breakdown from bottom to top is events with two kaons or a kaon and lepton (KK+KL), events with a soft pion (soft  $\pi$ ), events with a high momentum unidentified lepton (HPUL), events with a lower momentum lepton (LPL), and all remaining events. The outermost bins correspond to the category NT1 and the next to NT2. Entries for  $x_{NT} > 0.0$  represent correct tags, while those for  $x_{NT} < 0$  are mistags in each of the categories. The center bin contains events for which no tag is assigned.

used as input to a geometrical fit to a single vertex, including all other tracks in the event except those used to reconstruct  $B_{\text{rec}}$ . In order to reduce bias and tails due to long-lived particles,  $K_s^0$  and  $\Lambda^0$  candidates are used as input to the fit in place of their daughters. In addition, tracks consistent with photon conversions ( $\gamma \rightarrow e^+e^-$ ) are excluded. To reduce contributions from charm decay products, which bias the determination of the vertex po-

sition, the track with the largest vertex  $\chi^2$  contribution greater than 6 is removed and the fit is redone until no track fails the  $\chi^2$  requirement. In Monte Carlo simulation, the RMS of the core and tail Gaussian components of the residual  $\Delta z$  distribution (measured  $\Delta z$  minus true  $\Delta z$ ) is  $190\ \mu\text{m}$ . We fit this residual distribution to the sum of three Gaussian distributions and find that the RMS of the narrowest Gaussian, which contains 70% of the area, is about  $100\ \mu\text{m}$ . Only 1% of the area is in the widest Gaussian.

The absolute scale of the measurement of  $\Delta z$  depends on the assumed positions of the silicon wafers in the SVT. These positions are determined from a combination of survey measurements made before the SVT was installed and measurements of the positions of individual SVT modules, each containing several silicon wafers, made with high-momentum charged particles that traverse the SVT. We check the absolute scale comparing the known positions of distinct mechanical features at each end of the beampipe (about 18 cm apart) with the apparent position measured with charged tracks in the SVT. The locations of these mechanical features are measured from the positions of track vertices at least 2 cm from the interaction point that contain a well-identified proton, which are mainly due to  $e^\pm$ -nucleon interactions in material. The measured distance in  $z$  between these mechanical features is in agreement with the known distance to a precision of 0.2%. We conservatively enlarge this to 0.4% to account for any additional uncertainty in extrapolating to the interaction point.

### B. $\Delta t$ measurement

By far the dominant limitation on the accuracy with which  $\Delta t$  is determined from the measured decay length difference  $\Delta z$  is the experimental resolution on the  $\Delta z$  measurement. The next most significant limitation is the  $B$  meson momentum of about  $340\ \text{MeV}/c$  in the  $\Upsilon(4S)$  rest frame. We partially correct for this effect, as described below. The impact on the  $\Delta t$  measurement of the spread in the two beam energies, which results in a distribution of  $\Upsilon(4S)$  momenta with a Gaussian width of about  $6\ \text{MeV}/c$ , is negligible. Finally, we correct for the 20 mrad angle between the  $\Upsilon(4S)$  boost direction (the  $z$  axis in the following discussion) and the axis of symmetry of the detector, along which we measure the separation between vertices.

Neglecting the  $B$  momentum in the  $\Upsilon(4S)$  frame, we can write

$$\Delta z = \beta\gamma c\Delta t, \quad (20)$$

where  $\beta\gamma$  is the  $\Upsilon(4S)$  boost factor. The average value for the boost factor is  $\beta\gamma = 0.55$ . The boost factor is calculated directly from the beam energies, which are monitored every 5 seconds, and has an uncertainty of 0.1%.

In the case of a fully reconstructed  $B_{\text{rec}}$ , we measure with good precision the momentum direction of the reconstructed candidate, which can be used to correct for the  $B$  momentum in the  $\Upsilon(4S)$  frame. However, the correction depends on the sum of the decay times,  $t_{\text{rec}} + t_{\text{tag}}$ , which can only be determined with very poor resolution. We use the estimate  $t_{\text{rec}} + t_{\text{tag}} = \tau_B + |\Delta t|$  to correct for the measured  $B_{\text{rec}}$  momentum direction and extract  $\Delta t$  from the following expression:

$$\Delta z = \beta\gamma\gamma_{\text{rec}}^*c\Delta t + \gamma\beta_{\text{rec}}^*\gamma_{\text{rec}}^*\cos\theta_{\text{rec}}^*c(\tau_B + |\Delta t|), \quad (21)$$

where  $\theta_{\text{rec}}^*$ ,  $\beta_{\text{rec}}^*$ , and  $\gamma_{\text{rec}}^*$  are the polar angle with respect to the beam direction, the velocity, and the boost factor of the  $B_{\text{rec}}$  in the  $\Upsilon(4S)$  frame. The difference between  $\Delta t$  calculated with Eq. 20 and Eq. 21 is very small because  $\gamma_{\text{rec}}^* = 1.002$  and  $\beta_{\text{rec}}^* = 0.064$ . The event-by-event difference in  $\Delta t$  calculated with the two methods has an RMS of 0.20 ps. Equation 21 improves the  $\Delta t$  resolution by about 5%. In addition, it removes a correlation between the resolution on  $\Delta t$  and the true value of  $\Delta t$ . This correlation is due to the fact that the RMS of the second term in Eq. 21 depends on the expectation value of  $(t_{\text{rec}} + t_{\text{tag}})^2$ , which in turn depends on  $|\Delta t|$ . Equation 21 is used for all  $B$  decays to hadronic final states, while Eq. 20 is used for semileptonic modes since the  $B$  direction cannot be measured for these decays.

### C. Vertex quality requirements

A number of requirements are made in order to ensure a well-determined vertex separation. The fit for both the  $B_{\text{rec}}$  and  $B_{\text{tag}}$  vertex must converge. Also, the error on  $\Delta t$  determined from the vertex fit must be less than 2.4 ps and  $|\Delta t|$  must be less than 20 ps. The efficiency for passing these requirements in data and Monte Carlo simulation is about 97% for all  $B_{\text{rec}}$  modes. From the Monte Carlo simulation, we find that the reconstruction efficiency does not depend on the true value of  $\Delta t$ .

The  $B_{\text{rec}}$  sample is used both to extract the  $B^0$ - $\bar{B}^0$  mixing frequency and to measure the mistag probabilities for the analysis of time-dependent  $CP$ -violating asymmetries. While the  $CP$  measurement is statistically limited, the mixing measurement has a statistical precision of a few percent. Therefore, in order to reduce systematic uncertainties in the mixing measurement, more restrictive vertex criteria are imposed for the  $B_{\text{rec}}$  sample used for the mixing measurement than for the  $CP$  and  $B_{\text{rec}}$  samples used for the  $CP$  measurement. However, as described in Section VIII C 5, the more restrictive criteria are also used as a cross-check in the  $CP$  measurement. In order to reduce further the contributions from charm decay products in the mixing analysis, a track is not used in the reconstruction of the  $B_{\text{tag}}$  vertex if it is identified as a kaon according to the kaon identification algorithm used for tagging (see Section IV A). The maximum allowed error on  $\Delta t$  determined from the vertex fit is decreased from 2.4 ps for the samples used for the  $CP$  measurement

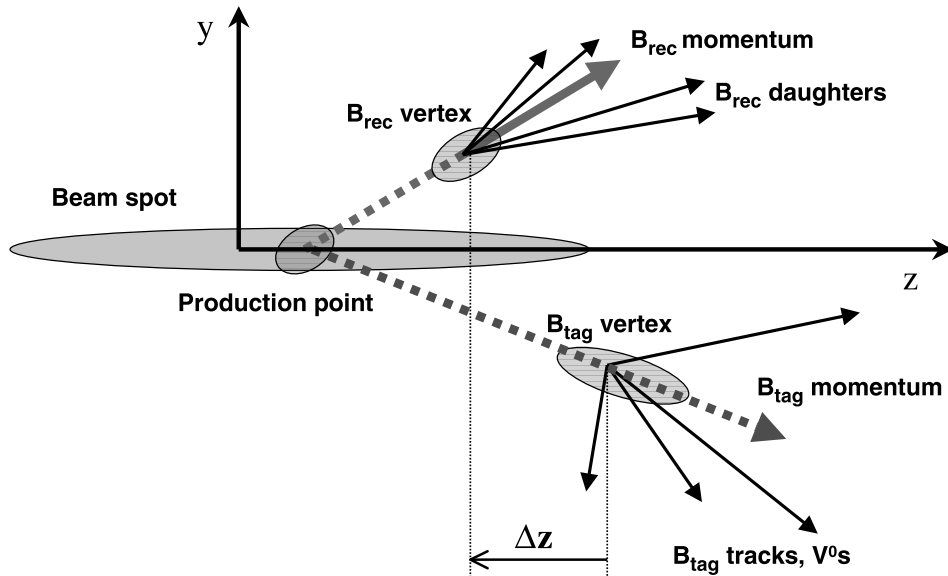


FIG. 15: Schematic view of the geometry in the  $yz$  plane for a  $\Upsilon(4S) \rightarrow B\bar{B}$  decay. For fully reconstructed decay modes, the line of flight of the  $B_{\text{tag}}$  can be estimated from the (reverse) momentum vector and the vertex position of  $B_{\text{rec}}$ , and from the beam spot position in the  $xy$  plane and the  $\Upsilon(4S)$  average boost. Note that the scale in the  $y$  direction is substantially magnified compared to that in the  $z$  direction.

to 1.4 ps for the sample used for the mixing measurement. The efficiency to pass these two additional criteria is about 87% in data. All figures in this section are obtained with the vertex selection criteria applied in the  $CP$  analysis.

#### D. $\Delta t$ resolution function

The  $\Delta t$  resolution function is represented in terms of  $\delta_t = \Delta t - \Delta t_{\text{true}}$  by a sum of three Gaussian distribu-

tions (called the core, tail and outlier components) with different means and widths:

$$\mathcal{R}(\delta_t; \hat{a}) = \sum_{k=1}^2 \frac{f_k}{S_k \sigma_{\Delta t} \sqrt{2\pi}} \exp\left(-\frac{(\delta_t - b_k \sigma_{\Delta t})^2}{2(S_k \sigma_{\Delta t})^2}\right) + \frac{f_3}{\sigma_3 \sqrt{2\pi}} \exp\left(-\frac{\delta_t^2}{2\sigma_3^2}\right). \quad (22)$$

For the core and tail Gaussians, we use the measurement error  $\sigma_{\Delta t}$  derived from the vertex fit for each event but allow two separate scale factors  $S_1$  and  $S_2$  to accommodate an overall underestimate ( $S_k > 1$ ) or overestimate ( $S_k < 1$ ) of the errors for all events. Figure 16a illustrates the correlation between the RMS of  $\delta_t$  and  $\sigma_{\Delta t}$  in Monte Carlo simulation. The core and tail Gaussian distributions are allowed to have a nonzero mean to account for residual charm decay products included in the  $B_{\text{tag}}$  vertex. In the resolution function, these mean offsets are

scaled by the event-by-event measurement error  $\sigma_{\Delta t}$  to account for an observed correlation shown in Fig. 16b between the mean of the  $\delta_t$  distribution and the measurement error  $\sigma_{\Delta t}$  in Monte Carlo simulation. This correlation is due to the fact that, in  $B$  decays, the vertex error ellipse for the  $D$  decay products is oriented with its major axis along the  $D$  flight direction, leading to a correlation between the  $D$  flight direction and the calculated uncertainty on the vertex position in  $z$  for the  $B_{\text{tag}}$  candidate. In addition, the flight length of the  $D$  in the  $z$

direction is correlated with its flight direction. Therefore, the bias in the measured  $B_{\text{tag}}$  position due to inclusion of  $D$  decay products is correlated with the  $D$  flight direction. Taking into account these two correlations, we conclude that  $D$  mesons that have a flight direction perpendicular to the  $z$  axis in the laboratory frame will have the best  $z$  resolution and will introduce the least bias in a measurement of the  $z$  position of the  $B_{\text{tag}}$  vertex, while  $D$  mesons that travel forward in the laboratory will have poorer  $z$  resolution and will introduce a larger bias in the measurement of the  $B_{\text{tag}}$  vertex.

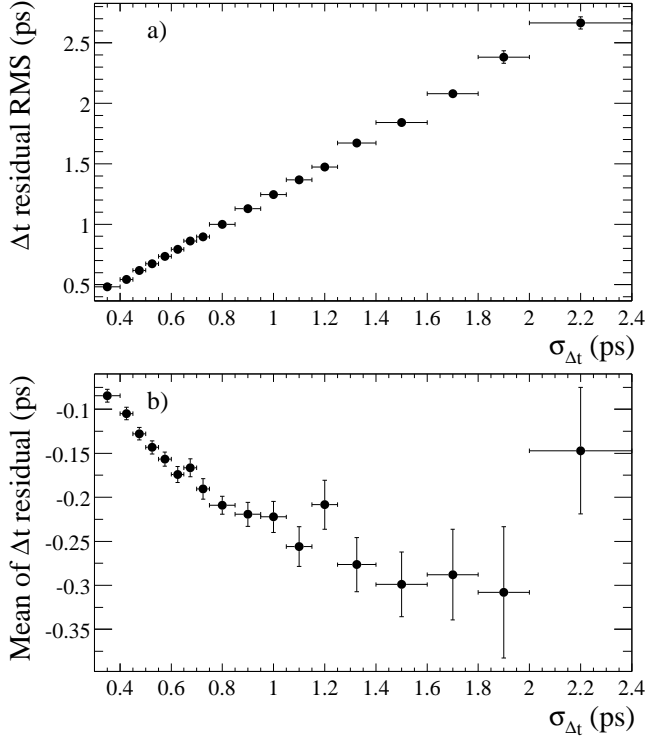


FIG. 16: Correlation between the event-by-event error on  $\Delta t$  ( $\sigma_{\Delta t}$ ) and a) the observed RMS and b) offset of the mean for  $\delta_t = \Delta t - \Delta t_{\text{true}}$  from Monte Carlo simulation.

Monte Carlo simulations confirm the expectation that the resolution function is less biased for events with a primary lepton tag than those with a kaon tag. Therefore, the mean of the core Gaussian is allowed to be different for each tagging category. One common mean is used for the tail component. The third Gaussian has a fixed width of 8 ps and no offset; it accounts for the fewer than 1% of events with incorrectly reconstructed vertices. The resolution parameters extracted from the full likelihood fits to the  $\Delta t$  distributions are shown in Table XIII for the mixing analysis and in Table XVI for the  $CP$  analysis.

Figure 17 shows the distribution of the uncertainties on  $\Delta t$  calculated from the fit to  $\Delta z$  for the flavor-eigenstate sample, and the combined  $\eta_{CP} = -1$  ( $J/\psi K_S^0$ ,  $\psi(2S)K_S^0$ ,  $\chi_{c1}K_S^0$ ) and  $J/\psi K^{*0}$  samples, and compares data with Monte Carlo predictions. Since the  $B_{\text{tag}}$  vertex precision dominates the  $\Delta t$  resolution, no significant differ-

ences between the  $\Delta t$  resolution function for the flavor-eigenstate sample and the  $CP$ -eigenstate sample are expected. Hence, identical resolution functions are used for all modes.

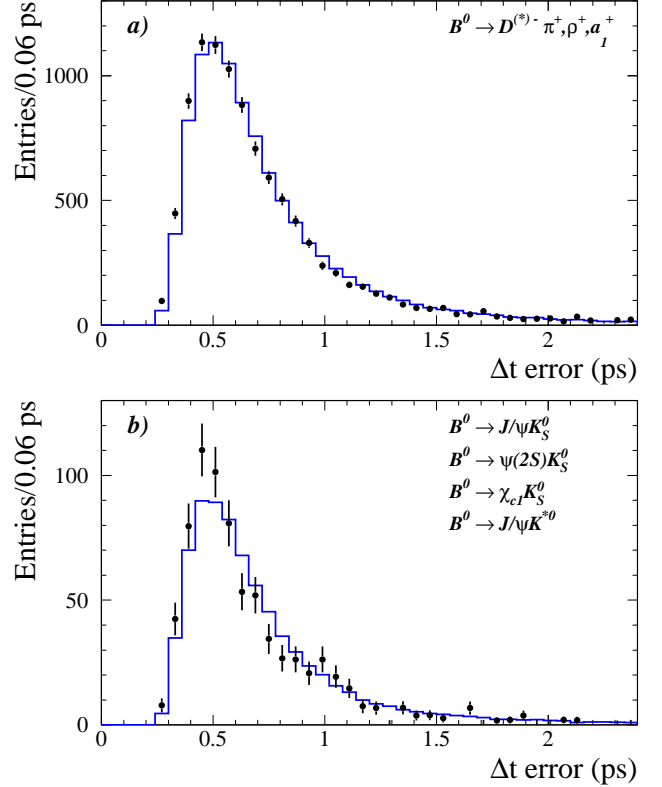


FIG. 17: Distribution of event-by-event uncertainties on  $\Delta t$  ( $\sigma_{\Delta t}$ ) for a) the sample of neutral  $B$  decays to flavor eigenstates other than  $J/\psi K^{*0}(K^+\pi^-)$  and b) the combined  $\eta_{CP} = -1$  ( $J/\psi K_S^0$ ,  $\psi(2S)K_S^0$ ,  $\chi_{c1}K_S^0$ ) and  $J/\psi K^{*0}$  samples. The histogram corresponds to Monte Carlo simulation and the points with error bars to data. All distributions have been background-subtracted with events from the  $m_{ES}$  sideband. The Monte Carlo distribution has been normalized to the same area as the data distribution.

## E. Checks and control samples

Two of the fundamental assumptions in this analysis are that the  $\Delta t$  resolution function for the sample of flavor-eigenstate modes is the same as that for  $CP$  events, and that the event-by-event vertex errors provide a good measure of the relative uncertainty on the  $\Delta z$  measurement from event to event. In this section, we describe several studies that have been done to validate these assumptions. We compare various distributions for the  $CP$  and flavor-eigenstate samples, in both data and Monte Carlo simulation. We take advantage of the small vertical size of the beam to measure the resolution for the  $B_{\text{rec}}$  and the  $B_{\text{tag}}$  vertices in the vertical direction.

We also study the vertex resolution for a sample of  $D^{*+}$  candidates from  $c\bar{c}$  events and for continuum events in data and Monte Carlo simulation.

### 1. Comparison of flavor-eigenstate and CP samples

In Fig. 18, we compare various properties of the flavor-eigenstate sample with the combined  $\eta_{CP} = -1$  and  $J/\psi K^{*0}$  samples. These include the  $\chi^2$  probability for the vertex fits, the number of tracks used in the  $B_{\text{tag}}$  vertex, and the momentum in the  $\Upsilon(4S)$  rest frame and polar angle in the laboratory frame of tracks used in the  $B_{\text{tag}}$  vertex. Good agreement in all variables is observed between the two data samples.

A similar comparison of the momentum and polar-angle distribution of tracks in data and Monte Carlo simulation also shows good agreement. However, there are modest discrepancies for the  $\chi^2$  probability for the vertex fits and the number of tracks used in the  $B_{\text{tag}}$  vertex. The agreement improves when we include residual misalignments between the SVT silicon modules in the Monte Carlo simulation. Systematic uncertainties due to residual SVT misalignments in data are discussed in Sections VII B 1 and VIII B.

As expected, there are no significant differences observed in comparisons between the  $CP$  modes used in the  $\sin 2\beta$  analysis. However, comparisons between the  $CP$  and flavor-eigenstate samples, in data as well as in the Monte Carlo simulation, show that the  $CP$  events have a slightly better  $\Delta z$  resolution. For example, in Monte Carlo simulation the most probable value for  $\sigma_{\Delta t}$  is about 0.017 ps (3%) worse for the  $B_{\text{flav}}$  sample, as can be seen by comparing the distributions in Figures 17a and b. This is due to the fact that the  $B_{CP}$  vertex is better determined because tracks in the lower-multiplicity  $CP$  final states generally have higher momentum. We account for this effect in the likelihood fit by using the calculated event-by-event errors, as described in Section V D. Indeed, for Monte Carlo simulation, the pull distributions for  $\sigma_{\Delta t}$  (defined as the difference between the fitted and generated value divided by the calculated error) are nearly Gaussian with unit width for both the  $B_{CP}$  and  $B_{\text{flav}}$  samples. Any residual effect due to differences in the observed scale factors in data is included as a systematic uncertainty (see Section VIII B) and found to be negligible.

### 2. Vertex resolution in vertical direction

Since the size of the PEP-II beam is only about  $10 \mu\text{m}$  in the vertical ( $y$ ) direction, the measured distance  $\Delta y$  between the  $B_{\text{rec}}$  or  $B_{\text{tag}}$  vertex and the nominal beam spot position in the  $y$  direction can be used to compare the resolution for the  $CP$  and flavor-eigenstate samples, and to evaluate the accuracy of the event-by-event errors  $\sigma(\Delta y)$ . The average beam-spot  $y$  position is determined

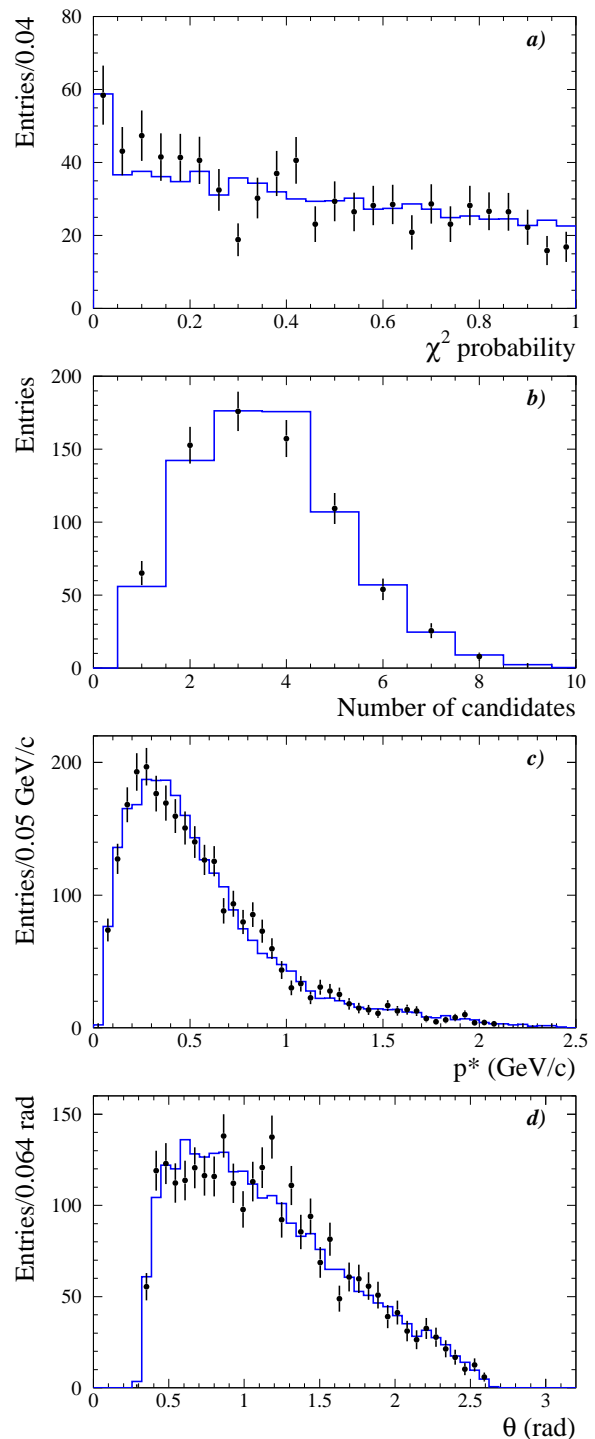


FIG. 18: Distributions of a)  $\chi^2$  probability of the  $B_{\text{tag}}$  vertex fit, b) number of charged tracks and  $V^0$  candidates used in the  $B_{\text{tag}}$  vertex, c) momentum in the center-of-mass frame, and d) polar angle in the laboratory frame for tracks in the  $B_{\text{tag}}$  vertex, for the flavor-eigenstate (histograms) and the combined  $\eta_{CP} = -1$  and  $J/\psi K^{*0}$  (points with error bars) data samples. All distributions have been background-subtracted with events from the  $m_{ES}$  sideband. The flavor-eigenstate distributions have been normalized to the same area as the distributions from the combined  $\eta_{CP} = -1$  and  $J/\psi K^{*0}$  samples.

with a precision of better than a few microns with two-track events for each data run (approximately one hour of recorded data). There is a non-negligible contribution to  $\Delta y$  of  $\approx 25 \mu\text{m}$  (RMS) due to the  $B$  lifetime and the transverse momentum of the  $B$ .

The distance in  $y$  between the  $B_{\text{tag}}$  vertex and the beam spot is used to measure the  $B_{\text{tag}}$  vertex resolution and bias in  $y$ . In Fig. 19, we show the distribution of  $\Delta y/\sigma(\Delta y)$  for the  $B_{\text{tag}}$  vertex for the flavor-eigenstate and  $CP$  samples, in data and Monte Carlo simulation. The RMS of the  $\Delta y/\sigma(\Delta y)$  distribution is 1.3 and 1.4 for Monte Carlo simulation and data, respectively. No statistically significant biases are observed.

Similar results are obtained for the  $B_{\text{rec}}$  vertex resolution. In addition, good agreement in the resolution on the  $y$  position is observed between the flavor-eigenstate sample and the  $CP$  sample. The resolution is about 5% worse in data than in Monte Carlo simulation.

### 3. Vertex resolution in continuum events

Two samples have been used to cross-check the reliability of the resolution function extracted from the likelihood fit as well as the discrepancies between data and Monte Carlo simulation: a sample of 109,000  $D^{*+}$  candidates from  $c\bar{c}$  events and a sample of off-resonance data.

For the first sample, we reconstruct high-momentum  $D^{*+}$  candidates in the mode  $D^{*+} \rightarrow D^0\pi^+$ , followed by  $D^0 \rightarrow K^-\pi^+$ ,  $K^-\pi^+\pi^0$ , or  $K^-\pi^+\pi^-\pi^+$ , and then use the remainder of the charged tracks in the event (fragmentation particles and recoil charm decay products) to determine a vertex position with the standard  $B_{\text{tag}}$  vertex algorithm. Since position information for the  $D^{*+}$  vertex is poor, due to scattering of the slow pion, and the  $D^{*+}$  decay point coincides with the  $e^+e^-$  interaction point, a beam-spot constraint is used for the  $D^{*+}$ . In Fig. 20, we show the distribution of the distance along the  $z$  axis between the  $D^{*+}$  vertex and the vertex formed from the rest of the tracks in the event  $\Delta z$ , as well as  $\Delta z$  divided by the event-by-event error on  $\Delta z$ , for both data and Monte Carlo simulation.

In Monte Carlo simulation, the resolution on  $z$  for the  $D^{*+}$  candidate is  $\approx 90 \mu\text{m}$ , very similar to that for  $B_{\text{rec}}$  vertices. However, the momentum spectrum of fragmentation tracks in  $c\bar{c}$  events is softer than that for tracks from  $B$  decays, while  $D$  mesons are more energetic in the  $D^{*+}$  control sample than in  $B$  decays. Therefore, a slightly more asymmetric resolution function is expected for the  $D^{*+}$  control sample compared to that for  $B$  events, as shown in Fig. 20a. Comparison of distributions of several sensitive variables (such as the number of tracks used in the vertex, and the momentum and polar angle of the tracks) shows small differences between  $D^{*+}$  and  $B$  events.

The RMS of the distance between the  $D^{*+}$  vertex and the vertex formed from the rest of the tracks in the events is about  $220 \mu\text{m}$  in the Monte Carlo simulation. Fitting

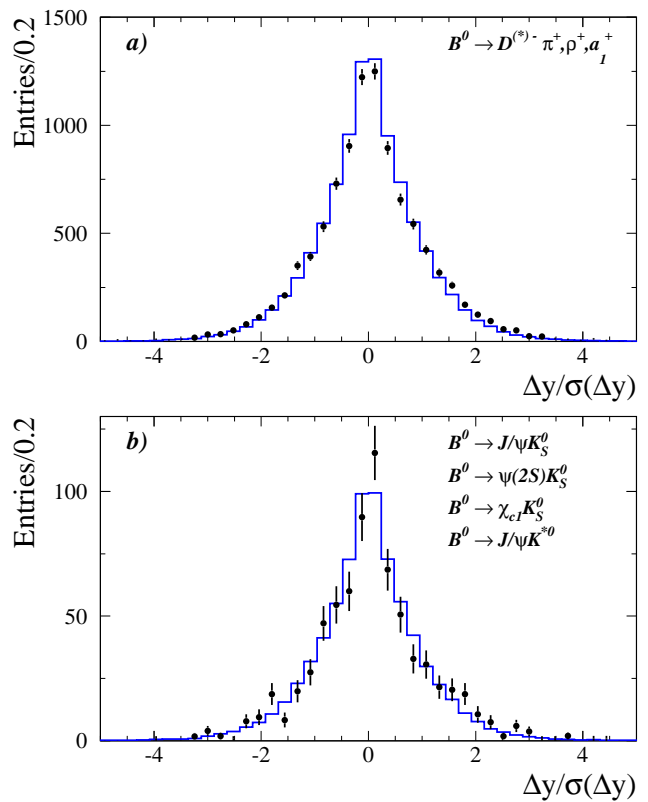


FIG. 19: Distributions of the measured distance in the vertical direction  $\Delta y$  between the  $B_{\text{tag}}$  vertex and the beam spot position, divided by the event-by-event error on the measured distance  $\sigma(\Delta y)$  for each event: a) Monte Carlo simulation (histogram) and data (points with error bars) for the flavor-eigenstate sample; b) flavor-eigenstate (histogram), and  $\eta_{CP} = -1$  and  $J/\psi K^{*0}$  (points with error bars) samples in data. All distributions have been background-subtracted with events from the  $m_{\text{ES}}$  sideband. In a), the data distribution has been normalized to the same area as the Monte Carlo simulation distribution; in b) the combined  $\eta_{CP} = -1$  and  $J/\psi K^{*0}$  data distribution has been normalized to the same area as the flavor-eigenstate distribution.

this distribution to the sum of three Gaussians, we find a resolution of about  $140 \mu\text{m}$  for 97% of the events, compared to  $150 \mu\text{m}$  for 99% of the  $B^0\bar{B}^0$  events. Only small differences are observed in the distribution of  $\Delta z/\sigma(\Delta z)$ , as illustrated in Fig. 20b. Therefore, the sample can be used to confirm the resolution and scale factors extracted from the likelihood fit, as well as to compare how well the Monte Carlo simulation reproduces the data.

The distributions are fit to the sum of three Gaussian distributions with different widths and means. The width of the third Gaussian is fixed to  $2.0\text{mm}$ . From the fit results, we come to the following conclusions:

- The event-by-event errors on  $\Delta z$  are underestimated by about 10% in data (Fig. 20b).
- The bias in the resolution function due to charm

decay products that is observed in data is well reproduced by the Monte Carlo simulation as shown in Fig. 20a and b.

- The resolution measured in the data is about 5% worse than that predicted by the Monte Carlo simulation (Fig. 20a).

These results will be compared with those obtained from the likelihood fit to the  $B$  events, described in Section VIII A.

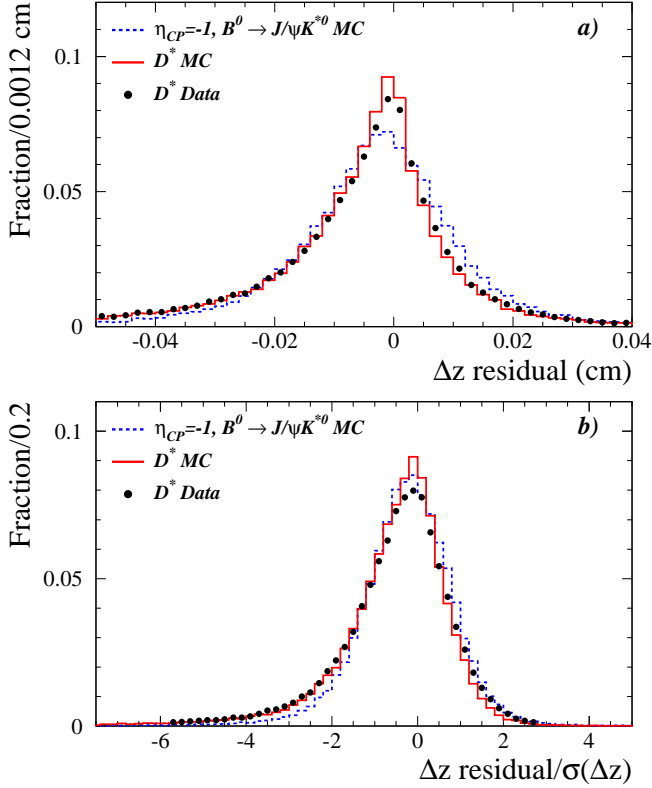


FIG. 20: a)  $\Delta z$  and b)  $\Delta z/\sigma(\Delta z)$  distributions for the  $D^{*+}$  control sample in data (points with error bars) and Monte Carlo simulation (solid histogram). For comparison, the difference between the measured  $\Delta z$  and true  $\Delta z$  for  $\eta_{CP} = -1$  and  $J/\psi K^{*0}$  events in Monte Carlo simulation is also shown (dashed histogram). All distributions are normalized to unit area.

The second control sample is obtained from off-resonance data alone. Charged tracks from these continuum events are randomly split into two sets, and the vertex of each set is found with the same algorithm used to determine the  $B_{\text{tag}}$  vertex. In this case the  $B_{\text{tag}}$  vertex reconstruction strategy is applied to both vertices in the event, so that this sample provides an unbiased estimation of the resolution, suitable for comparisons between data and Monte Carlo simulation. Results from this study are compatible with those reported above.

## F. Comparison of 1999-2000 and 2001 performance

The internal alignment of the SVT has improved significantly for the reconstruction of the 2001 data set (Run 2) compared to 1999-2000 (Run 1). Therefore, we expect better resolution and event-by-event errors on  $\Delta t$  for Run 2, which requires the use of separate resolution functions for the two data sets.

The differences in resolution and event-by-event errors for Run 1 and Run 2 are illustrated in Fig. 21, where a comparison of the distributions for  $\Delta z$  and  $\Delta z/\sigma(\Delta z)$  in the  $D^{*+}$  control sample described in Section VE 3 is shown. From the separate analysis of the two data sets, we conclude the following:

- The event-by-event errors on  $\Delta z$  are underestimated by 15% (5%) for the Run 1 (Run 2) data set (Fig. 21b).
- There is no statistically significant difference in the bias between the two data sets.
- The resolution for the Run 1 data set is about 15% worse than for that for Run 2 (Fig. 21a).

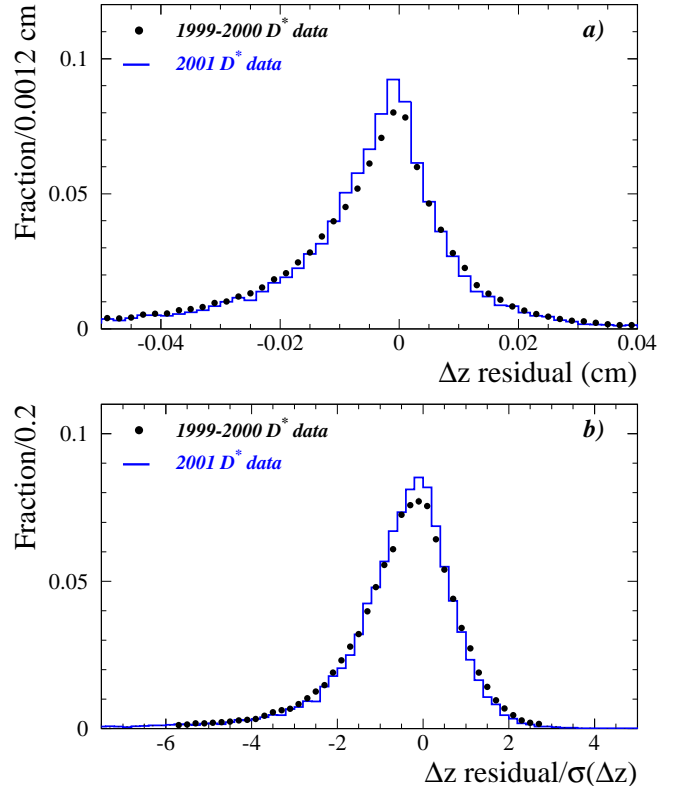


FIG. 21: Comparison of the distributions of a)  $\Delta z$  and b)  $\Delta z/\sigma(\Delta z)$  for the  $D^{*+}$  control sample (described in Section VE 3, for Run 1 (points) and Run 2 (histogram) data). All distributions are normalized to unit area.



The improved quality of the event-by-event errors in Run 2 is also illustrated in Fig. 22, where we compare the distributions of  $\chi^2$  probability for the  $B_{\text{tag}}$  vertex fit with the flavor-eigenstate data sample selected from the two different data periods.

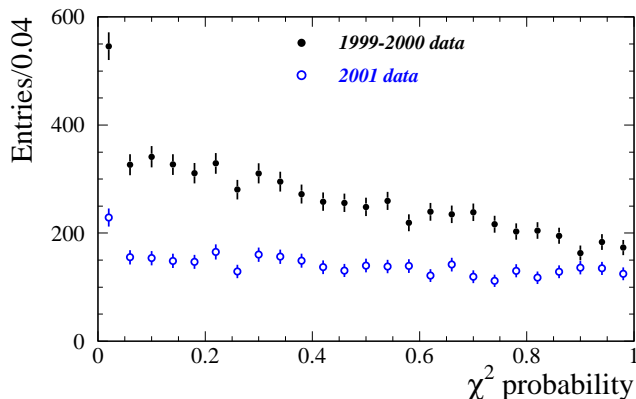


FIG. 22: Comparison of the  $\chi^2$  probability distributions of the  $B_{\text{tag}}$  vertex fit for the flavor-eigenstate data samples in Run 1 and Run 2. The distributions have been background-subtracted with events from the  $m_{\text{ES}}$  sideband. The area of each distribution equals the total number of events in the corresponding sample.

## VI. LIKELIHOOD FIT METHOD

The value of  $\sin 2\beta$  is extracted from the tagged  $B_{CP}$  sample with an unbinned maximum-likelihood technique based on  $\ln \mathcal{L}_{CP}$  and the probability density functions  $\mathcal{F}_{\pm}$  of Eq. 10. However, the dilutions  $\mathcal{D}_i$  and  $\Delta z$  resolution parameters  $\hat{a}_i$  are also needed for the measurement. Assuming that mistag rates and vertex resolutions do not depend on the particular channel used to reconstruct the  $B$  meson, these parameters are best determined with the much larger mixing sample, since they also appear in  $\mathcal{L}_{\text{mix}}$ . In order to properly incorporate the correlations between these parameters and  $\sin 2\beta$ , the fit is performed by simultaneously maximizing the sum

$$\ln \mathcal{L}_{CP} + \ln \mathcal{L}_{\text{mix}} \quad (23)$$

for the combined tagged  $B_{\text{flav}}$  and  $B_{CP}$  samples. The values of  $B^0$  lifetime and  $\Delta m_d$  are kept fixed in extracting  $\sin 2\beta$ .

The value of  $\Delta m_d$  is obtained with an unbinned maximum-likelihood fit to the tagged  $B_{\text{flav}}$  sample alone, where the log-likelihood  $\ln \mathcal{L}_{\text{mix}}$  is maximized while keeping the  $B^0$  lifetime fixed.

### A. Mistag asymmetries

The probabilities of mistagging a  $B^0$  or  $\bar{B}^0$  meson are expected to be very nearly, but not exactly, equal. For

example, the response of the detector to positive pions and kaons differs from its response to negative pions and kaons due to differences in total and charge-exchange cross sections. To account for any possible mistag differences, we introduce separate mistag probabilities  $w$  for  $B^0$  and  $\bar{w}$  for  $\bar{B}^0$  with the conventions

$$\begin{aligned} \langle w \rangle &= \frac{1}{2}(w + \bar{w}); & \Delta w &= (w - \bar{w}) \\ \mathcal{D} &= 1 - 2w; & \bar{\mathcal{D}} &= 1 - 2\bar{w} \\ \langle \mathcal{D} \rangle &= \frac{1}{2}(\mathcal{D} + \bar{\mathcal{D}}); & \Delta \mathcal{D} &= (\mathcal{D} - \bar{\mathcal{D}}) \end{aligned}$$

The time distributions for the mixing and  $CP$  samples will thus depend on whether the tag was identified as a  $B^0$  or a  $\bar{B}^0$ , resulting in modifications to the expressions for mixing time development (Eq. 3)

$$\begin{aligned} h_{\pm, \text{tag}=B^0} &\propto [(1 + \frac{1}{2}\Delta \mathcal{D}) \pm \langle \mathcal{D} \rangle \cos \Delta m_d \Delta t] \\ h_{\pm, \text{tag}=\bar{B}^0} &\propto [(1 - \frac{1}{2}\Delta \mathcal{D}) \pm \langle \mathcal{D} \rangle \cos \Delta m_d \Delta t], \quad (24) \end{aligned}$$

where the  $\pm$  in the index refers to mixed ( $-$ ) and unmixed ( $+$ ) events as before, and for  $CP$  violation time development (Eq. 7)

$$f_{\pm} \propto [(1 \pm \frac{1}{2}\Delta \mathcal{D}) \mp \langle \mathcal{D} \rangle \eta_{CP} \sin 2\beta \sin \Delta m_d \Delta t], \quad (25)$$

where the  $\pm$  in the index refers to events where  $B_{\text{tag}}$  is a  $B^0$  ( $+$ ) and  $\bar{B}^0$  ( $-$ ) and we have taken  $|\lambda| = 1$ .

### B. Background modeling

In the presence of backgrounds, the probability distribution functions  $\mathcal{H}_{\pm}$  of Eq. 4 and  $\mathcal{F}_{\pm}$  of Eq. 10 must be extended to include a term for each significant background source. The backgrounds for the flavor eigenstates and  $\eta_{CP} = -1$  modes are quite small and are mostly combinatoric in nature. However, for the  $B^0 \rightarrow J/\psi K_L^0$  and  $B^0 \rightarrow J/\psi K^{*0}$  channels the backgrounds are substantial and originate mainly from other  $B \rightarrow J/\psi X$  modes that have, to a very good approximation, the same flavor tagging and  $\Delta t$  resolution properties as the signal. The background properties of the flavor eigenstates,  $\eta_{CP} = -1$  modes, and the non- $J/\psi$  background in the  $B^0 \rightarrow J/\psi K_L^0$  channel are determined empirically from sideband events in the data.

#### 1. Background formulation for flavor eigenstates and $\eta_{CP} = -1$ modes

The background parameterizations are allowed to differ for each tagging category. Each event belongs to a particular tagging category  $i$ . In addition, the event is classified as either mixed ( $-$ ) or unmixed ( $+$ ) for a flavor-eigenstate or by whether  $B_{\text{tag}}$  was a  $B^0$  ( $+$ ) or a  $\bar{B}^0$  ( $-$ )

for a  $CP$ -eigenstate. Thus background distributions  $j$  must be specified for each possibility  $(+/-, i)$ , so that

---


$$\mathcal{H}_{\pm, i} = f_{i, \text{sig}}^{\text{flav}} \mathcal{H}_{\pm}(\Delta t; \Gamma, \Delta m_d, w_i, \hat{a}_i) + f_{i, \text{peak}}^{\text{flav}} \mathcal{B}_{\pm, i, \text{peak}}^{\text{flav}}(\Delta t; \hat{a}_i) + \sum_{j=\text{bkgd}} f_{i, j}^{\text{flav}} \mathcal{B}_{\pm, i, j}^{\text{flav}}(\Delta t; \hat{b}_i) \quad (26)$$

for flavor-eigenstates, and

$$\mathcal{F}_{\pm, i} = f_{i, \text{sig}}^{CP} \mathcal{F}_{\pm}(\Delta t; \Gamma, \Delta m_d, w_i, \sin 2\beta, \hat{a}_i) + f_{i, \text{peak}}^{CP} \mathcal{B}_{\pm, i, \text{peak}}^{CP}(\Delta t; \hat{a}_i) + \sum_{j=\text{bkgd}} f_{i, j}^{CP} \mathcal{B}_{\pm, i, j}^{CP}(\Delta t; \hat{b}_i) \quad (27)$$

for  $CP$ -eigenstates.

The fraction of background events for each source and tagging category is a function of  $m_{\text{ES}}$  and is given by  $f_{i, j}$ . The peaking and combinatorial background PDFs,  $\mathcal{B}_{\pm, i, \text{peak}}$  and  $\mathcal{B}_{\pm, i, j}$ , provide an empirical description of the  $\Delta t$  distribution of the background events in the sample, including a resolution function parameterized by  $\hat{a}_i$  and  $\hat{b}_i$ , respectively. These distributions are normalized such that, for each  $i$  and  $j$ ,

$$\int_{-\infty}^{\infty} (\mathcal{B}_{+, i, j} + \mathcal{B}_{-, i, j}) d\Delta t = 1. \quad (28)$$

The probability that a  $B^0$  candidate is a signal or a background event is determined from a separate fit to the observed  $m_{\text{ES}}$  distributions of  $B_{\text{flav}}$  or  $B_{CP}$  candidates with  $\eta_{CP} = -1$ . We describe the  $m_{\text{ES}}$  shape with a single Gaussian distribution  $\mathcal{S}(m_{\text{ES}})$  for the signal and an ARGUS parameterization  $\mathcal{A}(m_{\text{ES}})$  for the background (Eq. 16). Based on this fit, the event-by-event signal and background probabilities that appear as the relative weights for the various signal and background terms in Eq. 26 and 27 are given by

$$\begin{aligned} f_{i, \text{sig}}(m_{\text{ES}}) &= \frac{(1 - \delta_{\text{peak}}) \mathcal{S}(m_{\text{ES}})}{\mathcal{S}(m_{\text{ES}}) + \mathcal{A}(m_{\text{ES}})} \\ f_{i, \text{peak}}(m_{\text{ES}}) &= \frac{\delta_{\text{peak}} \mathcal{S}(m_{\text{ES}})}{\mathcal{S}(m_{\text{ES}}) + \mathcal{A}(m_{\text{ES}})} \\ \sum_{j=\text{bkgd}} f_{i, j}(m_{\text{ES}}) &= \frac{\mathcal{A}(m_{\text{ES}})}{\mathcal{S}(m_{\text{ES}}) + \mathcal{A}(m_{\text{ES}})} \end{aligned} \quad (29)$$

The fraction  $\delta_{\text{peak}}$  of the signal Gaussian distribution that is due to peaking backgrounds is determined from Monte Carlo simulation.

Backgrounds arise from many different sources. Rather than attempting to determine the various physics contributions we use an empirical description in the likelihood fit, allowing for background components with various time dependencies. For the  $B_{\text{flav}}$  sample, the background time distributions considered, each with its own effective dilution factor  $\mathcal{D}_i$  and either a common resolution function  $\mathcal{R}(\Delta t; \hat{b}_i)$  or the signal resolution function

the full likelihood function becomes

---

$\mathcal{R}(\delta_t = \Delta t - \Delta t_{\text{true}}; \hat{a}_i)$ , are

$$\begin{aligned} \mathcal{B}_{\pm, i, 1}^{\text{flav}} &= \frac{1}{2} (1 \pm \mathcal{D}_{i, 1}^{\text{flav}}) \delta(\Delta t_{\text{true}}) \otimes \mathcal{R}(\delta_t; \hat{b}_i), \\ \mathcal{B}_{\pm, i, 2}^{\text{flav}} &= \frac{1}{4} \Gamma_{i, 2}^{\text{flav}} (1 \pm \mathcal{D}_{i, 2}^{\text{flav}}) \times \\ &\quad e^{-\Gamma_{i, 2}^{\text{flav}} |\Delta t_{\text{true}}|} \otimes \mathcal{R}(\delta_t; \hat{b}_i), \\ \mathcal{B}_{\pm, i, 3}^{\text{flav}} &= \frac{1}{4} \Gamma_{i, 3}^{\text{flav}} (1 \pm \mathcal{D}_{i, 3}^{\text{flav}} \cos \Delta m_{i, 3} \Delta t_{\text{true}}) \times \\ &\quad e^{-\Gamma_{i, 3}^{\text{flav}} |\Delta t_{\text{true}}|} \otimes \mathcal{R}(\delta_t; \hat{b}_i), \\ \mathcal{B}_{\pm, i, \text{peak}}^{\text{flav}} &= \frac{1}{4} \Gamma_{i, \text{peak}} (1 \pm \mathcal{D}_{i, \text{peak}}^{\text{flav}} \cos \Delta m_{i, \text{peak}} \Delta t_{\text{true}}) \times \\ &\quad e^{-\Gamma_{i, \text{peak}}^{\text{flav}} |\Delta t_{\text{true}}|} \otimes \mathcal{R}(\delta_t; \hat{a}_i), \end{aligned} \quad (30)$$

corresponding to prompt, non-prompt, and mixing background components, as well as a peaking contribution. For the  $\eta_{CP} = -1$  sample, the possible background contributions are

$$\begin{aligned} \mathcal{B}_{\pm, i, 1}^{CP} &= \frac{1}{2} \delta(\Delta t) \otimes \mathcal{R}(\delta_t; \hat{b}_i), \\ \mathcal{B}_{\pm, i, 2}^{CP} &= \frac{1}{4} \Gamma_{i, 2} (1 \pm \mathcal{D}_{i, 2}^{CP} \sin \Delta m_d \Delta t) \times \\ &\quad e^{-\Gamma_{i, 2}^{CP} |\Delta t|} \otimes \mathcal{R}(\delta_t; \hat{b}_i), \\ \mathcal{B}_{\pm, i, \text{peak}}^{CP} &= \frac{1}{4} \Gamma_{i, \text{peak}} (1 \pm \mathcal{D}_{i, \text{peak}}^{CP} \sin \Delta m_d \Delta t) \times \\ &\quad e^{-\Gamma_{i, \text{peak}}^{CP} |\Delta t|} \otimes \mathcal{R}(\delta_t; \hat{a}_i), \end{aligned} \quad (31)$$

corresponding to prompt and  $CP$  background components, as well as a peaking contribution. The background resolution function parameters  $\hat{b}_i$  are common with the background resolution function of the  $B_{\text{flav}}$  sample. The likelihood fit includes as free parameters the fraction of each time component, as well as apparent lifetimes, resolutions, mixing frequencies and dilutions that best describe the events with high weights for being background. These parameters are described in Section VID below, along with additional assumptions.

TABLE IX: Parameters of the probability distribution function for the non- $J/\psi$  background contribution in the  $B^0 \rightarrow J/\psi K_L^0$  channel.

Parameter	Fit result
$F_{\tau=0}$	$0.16 \pm 0.49$
$\Gamma_{i,2}$ [ps $^{-1}$ ]	$1.25 \pm 0.45$
$S_1$	$1.12 \pm 0.26$
$b_1$	$-0.11 \pm 0.20$
$S_2$	$3.9 \pm 0.8$
$b_2$	$-1.2 \pm 1.0$
$f_2$	$0.23 \pm 0.14$
$f_3$	0.005 (fixed)

## 2. Background formulation for $B^0 \rightarrow J/\psi K_L^0$

The higher background level in the  $B^0 \rightarrow J/\psi K_L^0$  channel requires a more extensive treatment of its properties.

---


$$\mathcal{F}_{\pm,i} = f_{i,k,\text{sig}}(\Delta E) \mathcal{F}_{\pm}(\Delta t; \Gamma, \Delta m_d, w_i, \sin 2\beta, \hat{a}_i) + \sum_{\alpha=J/\psi X} f_{i,k,\alpha}(\Delta E) \mathcal{F}_{\pm}(\Delta t; \Gamma, \Delta m_d, \eta_{CP,\alpha}, w_i, \sin 2\beta, \hat{a}_i) + f_{i,k,\text{non-}J/\psi}(\Delta E) \mathcal{B}_{\pm}^{KL}(\Delta t; \hat{b}). \quad (32)$$


---

Each event is classified according to its flavor tagging category ( $i$ ), flavor tag value ( $\pm$ ), and the  $K_L^0$  reconstruction category ( $k$ ), which is either EMC or IFR. The signal fraction  $f_{i,k,\text{sig}}$  and background fractions  $f_{i,k,\alpha}$  and  $f_{i,k,\text{non-}J/\psi}$  are determined as a function of  $\Delta E$  and are the same for all tagging categories. The shape of the signal and background  $\Delta E$  functions are determined either from data (non- $J/\psi$  contribution) or from Monte Carlo samples (signal and  $J/\psi X$  background). The normalizations  $\int_{-10 \text{ MeV}}^{10 \text{ MeV}} f d(\Delta E)$  are determined from Tables VI and VII so that

$$\int_{-10 \text{ MeV}}^{10 \text{ MeV}} [f_{i,k,\text{sig}}(\Delta E) + f_{i,k,\text{non-}J/\psi}(\Delta E) + \sum_{J/\psi X} f_{i,k,\alpha}(\Delta E)] d(\Delta E) = 1. \quad (33)$$

The non- $J/\psi$  background PDF is given by

$$\mathcal{B}_{\pm}^{KL} = F_{\tau=0} \mathcal{B}_{\pm,i,1}^{CP} + (1 - F_{\tau=0}) \mathcal{B}_{\pm,i,2}^{CP} \quad (34)$$

where the dilutions  $\mathcal{D}_{i,2}^{CP} = 0$  and the prompt fraction  $F_{\tau=0}$ , effective decay width  $\Gamma_{i,2}$ , and  $\Delta t$  resolutions parameters  $\hat{b}$  are fixed to values obtained from an external fit to the  $m(\ell\ell)$  sideband events as given in Table IX. The resolution function  $\mathcal{R}(\Delta t; \hat{b})$  is defined in Eq. 22 with  $f_3 = 0.005$  and with core bias  $\delta_1$  equal for all tagging categories.

As discussed in Section IIID, the data are used to determine the relative fraction of signal, background from  $B \rightarrow J/\psi X$  events, and events with a misreconstructed  $J/\psi \rightarrow \ell\ell$  candidate. Along with a Monte Carlo simulation of the channels that contribute to the  $B \rightarrow J/\psi X$  background, this information is used to formulate the PDF model. In addition, some of the  $J/\psi X$  background modes, such as  $B^0 \rightarrow J/\psi K^{*0}$  and  $B^0 \rightarrow J/\psi K_s^0$ , have a non-zero  $CP$  asymmetry ( $\eta_{CP}$ ), as given in Table VI. The value of the asymmetry in  $B^0 \rightarrow J/\psi K^{*0}(K_L^0 \pi^0)$  is taken from the measurement of  $R_{\perp} = 0.160 \pm 0.032 \pm 0.014$  in Ref. [13]. The probability density functions  $\mathcal{F}_{\pm}$  of Eq. 10 are modified to include contributions for each of the  $B \rightarrow J/\psi X$  channels  $\alpha$  specified in Table VI and the non- $J/\psi$  background component. The complete PDF is given by

The  $J/\psi K_L^0$  sample has significant background, primarily from other  $J/\psi$  modes. The Monte Carlo simulation is used to check the flavor tagging efficiency of the inclusive  $J/\psi$  background relative to the signal for the  $K_L^0$  mode. The inclusive  $J/\psi$  background fraction in the simulation is consistent across the flavor tagging categories to within a few percent. The flavor tagging efficiency for the fake- $J/\psi$  background, determined from the  $J/\psi$  sideband, is also roughly consistent with signal. The composition of the  $J/\psi K_L^0$  sample is determined from a fit of the  $\Delta E$  spectrum before flavor tagging. We assume the inclusive  $J/\psi$  and fake- $J/\psi$  background fractions are independent of flavor tag in the nominal fit and adjust the fractions as a function of tagging category, based on the Monte Carlo simulation and  $J/\psi$  sideband, in order to determine systematic errors.

Some of the decay modes in the inclusive  $J/\psi$  background, such as  $J/\psi K^{*0}$  and  $J/\psi K_s^0$ , have an expected  $CP$  asymmetry. The mistag fractions for all  $CP$  modes in the inclusive  $J/\psi$  background are determined with the Monte Carlo simulation and found to be consistent with the values for the signal. We assume that the signal mistag fractions apply to the  $CP$  modes in the inclusive  $J/\psi$  background.

The  $\Delta t$  resolution for the  $B \rightarrow J/\psi X$  background should be very similar to the signal resolution. However, extra tracks associated with  $B^+ \rightarrow J/\psi X^+$  decay, such

as the charged  $\pi$  from the  $K^{*+}$  decay in  $B^+ \rightarrow J/\psi K^{*+}$ , could bias the measurement of  $\Delta t$  since they are not associated with the  $B_{CP}$  vertex and therefore can be used in the  $B_{\text{tag}}$  vertex. In the Monte Carlo simulation, we find that extra tracks in the  $B \rightarrow J/\psi X$  decay modes have a negligible effect on the  $\Delta t$  resolution. Therefore, we assume that all  $B \rightarrow J/\psi X$  background has the same resolution as the signal.

The  $\Delta t$  resolution of the non- $J/\psi$  background is measured with the  $J/\psi$  sideband sample. The non- $J/\psi$   $\Delta t$  resolution parameters are varied by their statistical uncertainties to estimate the systematic uncertainty.

### 3. Background formulation for $B^0 \rightarrow J/\psi K^{*0}(K_S^0\pi^0)$

Monte Carlo simulation is used to construct the probability density function for the  $B^0 \rightarrow J/\psi K^{*0}(K_S^0\pi^0)$

channel. As shown in Table V, the background for this channel is due to true  $B \rightarrow J/\psi X$  decays. Thus, we assume that the background has the same resolution function and tagging performance as the signal. The probability density functions  $\mathcal{F}_{\pm}$  of Eq. 10 are modified to include contributions for each of the  $B \rightarrow J/\psi X$  channels  $\alpha$  specified in Table V. The complete PDF is given by

$$\mathcal{F}_{\pm,i} = f_{\text{sig}}\mathcal{F}_{\pm}(\Delta t; \Gamma, \Delta m_d, \eta_{CP,\text{signal}}, w_i, \sin 2\beta, \hat{a}_i) + \sum_{\alpha=\text{bkgd}} f_{\alpha} \mathcal{F}_{\pm}(\Delta t; \Gamma, \Delta m_d, \eta_{f,\alpha}, w_i, \sin 2\beta, \hat{a}_i), \quad (35)$$

where each event is classified according to its flavor tagging category ( $i$ ) and flavor tag value ( $\pm$ ). The signal and background fractions as well as  $\eta_{CP}$  are taken from Table V.

### C. Extensions for direct $CP$ search

While the main likelihood fits are performed with the Standard Model expectation that  $|\lambda| = 1$ , a search for the effects of direct  $CP$  violation is also made. Such a measurement is also particularly sensitive to possible differ-

ences in the fraction of  $B^0$  or  $\bar{B}^0$  meson that are tagged. Defining  $\epsilon_{\text{tag}}$  and  $\bar{\epsilon}_{\text{tag}}$  as the tagging efficiencies for  $B^0$  and  $\bar{B}^0$ , and  $\epsilon_r$  and  $\bar{\epsilon}_r$  as the reconstruction efficiencies for  $B^0$  and  $\bar{B}^0$  in the  $B_{\text{flav}}$  sample, it is useful to construct

$$\mu_i = \frac{\epsilon_{\text{tag},i} - \bar{\epsilon}_{\text{tag},i}}{\epsilon_{\text{tag},i} + \bar{\epsilon}_{\text{tag},i}}, \quad \langle \epsilon_{\text{tag}} \rangle_i = \frac{\epsilon_{\text{tag},i} + \bar{\epsilon}_{\text{tag},i}}{2} \quad (36)$$

$$\nu_i = \frac{\epsilon_{r,i} - \bar{\epsilon}_{r,i}}{\epsilon_{r,i} + \bar{\epsilon}_{r,i}}, \quad \langle \epsilon_r \rangle_i = \frac{\epsilon_{r,i} + \bar{\epsilon}_{r,i}}{2}. \quad (37)$$

For the  $B_{CP}$  sample, the time-dependent decay rate (Eq. 9) becomes

$$f_{\pm,i}(\Delta t) = \frac{\Gamma}{4} e^{-\Gamma|\Delta t|} \left[ \frac{(1 + |\lambda|^2)(1 \pm X_i)}{1 + |\lambda|^2 + \xi_i} + (\mu_i \pm X'_i) \left( \frac{2Im\lambda}{1 + |\lambda|^2 + \xi_i} \sin \Delta m_d \Delta t - \frac{1 - |\lambda|^2}{1 + |\lambda|^2 + \xi_i} \cos \Delta m_d \Delta t \right) \right], \quad (38)$$

where  $\xi_i = \mu_i(|\lambda|^2 - 1)/(1 + x_d^2)$ ,  $X_i = \mu_i \langle \mathcal{D} \rangle_i + \Delta \mathcal{D}_i/2$ , and  $X'_i = \langle \mathcal{D} \rangle_i + \mu_i \Delta \mathcal{D}_i/2$ . Likewise, for the  $B_{\text{flav}}$  sample the time-dependent decay rate (Eq. 3) becomes

$$h(\Delta t) = \frac{\Gamma}{4} e^{-\Gamma|\Delta t|} \frac{1 + s_1 \nu_i}{\left[ 1 - \frac{\mu_i \nu_i}{1 + x_d^2} \right]} [1 + s_2 X_i - s_1(\mu_i + s_2 X'_i) \cos \Delta m_d \Delta t] \quad (39)$$

where

$$\begin{aligned} s_1 &= 1(-1) \text{ if the reconstructed } B \text{ is a } B^0(\bar{B}^0) \\ s_2 &= 1(-1) \text{ for a } B^0(\bar{B}^0) \text{ tag.} \end{aligned}$$

The parameters  $\nu_i$ ,  $\langle \epsilon_{\text{tag}} \rangle_i$ , and  $\mu_i$  can be extracted from time-integrated numbers of events in the  $B_{\text{flav}}$  sam-

ple. Defining integrated samples of events by

$$\begin{aligned} N_i^{\text{tag}} &= N(B^0/\bar{B}^0 \text{ tag in } i^{\text{th}} \text{ category}, B_{\text{flav}} = B^0) \\ \bar{N}_i^{\text{tag}} &= N(B^0/\bar{B}^0 \text{ tag in } i^{\text{th}} \text{ category}, B_{\text{flav}} = \bar{B}^0) \\ N_i^{\text{no tag}} &= N(\text{no tag in } i^{\text{th}} \text{ category}, B_{\text{flav}} = B^0) \\ \bar{N}_i^{\text{no tag}} &= N(\text{no tag in } i^{\text{th}} \text{ category}, B_{\text{flav}} = \bar{B}^0), \end{aligned} \quad (40)$$

it can be shown that

$$\begin{aligned} \nu_i &= \frac{N_i^{\text{tag}} - \bar{N}_i^{\text{tag}} + N_i^{\text{no tag}} - \bar{N}_i^{\text{no tag}}}{N_i^{\text{tag}} + \bar{N}_i^{\text{tag}} + N_i^{\text{no tag}} + \bar{N}_i^{\text{no tag}}} \quad (41) \\ \langle \epsilon_{\text{tag}} \rangle_i &= \frac{2N_i^{\text{tag}}\bar{N}_i^{\text{tag}} + \bar{N}_i^{\text{tag}}N_i^{\text{no tag}} + N_i^{\text{tag}}\bar{N}_i^{\text{no tag}}}{2(N_i^{\text{tag}} + N_i^{\text{no tag}})(\bar{N}_i^{\text{tag}} + \bar{N}_i^{\text{no tag}})} \\ \mu_i &= \frac{(1 + x_d^2)(\bar{N}_i^{\text{tag}}N_i^{\text{no tag}} - N_i^{\text{tag}}\bar{N}_i^{\text{no tag}})}{2N_i^{\text{tag}}\bar{N}_i^{\text{tag}} + \bar{N}_i^{\text{tag}}N_i^{\text{no tag}} + N_i^{\text{tag}}\bar{N}_i^{\text{no tag}}} \end{aligned}$$

under the assumption that nearly all  $B$  mesons decay to final states that can be reached from either  $B^0$  or  $\bar{B}^0$ , but not both. The results for  $\langle \epsilon_{\text{tag}} \rangle_i$  and  $\mu_i$  are shown in Table X. The value of  $\nu_i$ , averaged over all four tagging categories, is  $0.004 \pm 0.012$ . While there is no statistically significant difference in the tagging efficiencies or the reconstruction efficiencies given by  $\mu_i$  and  $\nu_i$ , we use the central values obtained from the  $B_{\text{flav}}$  sample in performing the fit for  $|\lambda|$ .

TABLE X: Values of  $\langle \epsilon_{\text{tag}} \rangle_i$  and  $\mu_i$  for the four tagging categories, as determined by counting numbers of tagged and untagged events in the  $B_{\text{flav}}$  sample.

Tagging category	$\langle \epsilon_{\text{tag}} \rangle_i$	$\mu_i$
Lepton	$0.095 \pm 0.002$	$0.069 \pm 0.032$
Kaon	$0.358 \pm 0.003$	$-0.005 \pm 0.014$
NT1	$0.080 \pm 0.002$	$0.061 \pm 0.035$
NT2	$0.139 \pm 0.002$	$0.017 \pm 0.026$

TABLE XI: Average mistag fractions  $\langle w_i \rangle$  and mistag differences  $\Delta w_i$  for each tagging category  $i$  from a maximum-likelihood fit to the distribution for the  $B^+$  control sample.

Tagging category	$\langle w_i \rangle$ [%]	$\Delta w_i$ [%]
Lepton	$4.6 \pm 0.6$	$1.1 \pm 1.2$
Kaon	$11.8 \pm 0.5$	$-0.3 \pm 1.0$
NT1	$21.3 \pm 1.6$	$-5.9 \pm 3.2$
NT2	$37.2 \pm 1.3$	$-0.7 \pm 2.7$

#### D. Free parameters for the $\sin 2\beta$ and $\Delta m_d$ fits

The unbinned likelihood fit for  $\sin 2\beta$  has a total of 45 free parameters:

- **Value of  $\sin 2\beta$**

- **Signal resolution function:** Sixteen parameters  $\hat{a}_i$  to describe the resolution function for the signal. Due to improvements in the reconstruction algorithms, the Run 1 and Run 2 resolution functions are found to be different, as described in Section V F. Thus, we allow for separate resolution function parameters for these data samples, each with eight free parameters, being a scale factor  $S_1$  for the event-by-event  $\Delta z$  resolution errors of the core Gaussian components, individual core bias scale factors  $b_{1,i}$  for the four tagging categories and a common tail bias  $b_2$ , and the tail  $f_2$  and outlier  $f_3$  fractions; the scale factor of the tail component is fixed to 3.0 and the width of the outlier component is fixed to 8 ps with zero bias.

- **Signal dilutions:** Eight parameters to describe the measured average dilutions  $\langle \mathcal{D} \rangle_i$  and dilution differences  $\Delta \mathcal{D}_i$  in each tagging category.

- **Background resolution function:** Six parameters are used to describe a common resolution function for all non-peaking backgrounds. As with the signal resolution function, we include separate resolution function parameters for the Run 1 and Run 2 data samples. The resolution function is taken as a single Gaussian distribution with a scale factor  $S_1$  for the event-by-event  $\Delta z$  errors and a common bias scale factor  $b_1$ , and an outlier fraction  $f_3$ ; the width of the outlier component is taken to be a fixed 8 ps with zero bias.

- **$B_{\text{flav}}$  background composition parameters:** A total of 13 parameters describe the  $B_{\text{flav}}$  background composition. We make several assumptions to simplify the parameterization shown in Eq. 30, such as removing the mixing background contribution by setting  $f_{i,3}^{\text{flav}} = 0$ , and assign a corresponding systematic uncertainty. The size of the peaking background is determined from Monte Carlo simulation to be  $\delta_{\text{peak}}^{\text{flav}} = (1.5 \pm 0.5)\%$  of the signal contribution in each tagging category. This contribution is predominately from  $B^+$  events, so  $\Delta m_{i,\text{peak}} = 0$ ,  $\Gamma_{i,\text{peak}}^{\text{flav}} = \Gamma_{B^+}$  and  $D_{i,\text{peak}}^{\text{flav}}$  are taken from the  $B^+$  data sample (Table XI). The effective dilutions for the prompt ( $D_{i,1}^{\text{flav}}$ , 4 parameters) and non-prompt ( $D_{i,2}^{\text{flav}}$ , 4 parameters) contributions are allowed to vary. The relative amount of these two contributions is allowed to vary independently in each tagging category (4 parameters). For the non-prompt contribution,  $\Gamma_{i,2}^{\text{flav}}$  is assumed to be the same for all tagging categories, giving one free parameter.

- **$CP$  background composition parameters:** One parameter, the fraction of prompt relative to non-prompt background, assumed to be the same for each tagging category, is allowed to float to describe the  $CP$  background properties. The effective dilutions of the non-prompt and peaking contribu-

tion are set to zero ( $D_{i,2}^{CP} = D_{i,\text{peak}}^{CP} = 0$ ), corresponding to no  $CP$ -asymmetry in the background. The size and parameters of the peaking background are determined from Monte Carlo simulation. The fraction of peaking background is  $\delta_{\text{peak}}^{CP} = (1 \pm 1)\%$  of the signal contribution, independent of tagging category. This contribution is assumed to have lifetime parameters in common with the signal. Finally, the lifetime of the non-prompt background is assumed to be  $\tau_{B^0}$  in all tagging categories.

The unbinned likelihood fit for  $\Delta m_d$  has 44 free parameters, removing  $\sin 2\beta$  and the parameter for fraction of prompt background in the  $CP$  sample and leaving  $\Delta m_d$  to float.

### E. Blind analysis

A blind analysis technique was adopted for the extraction of  $\sin 2\beta$  and  $\Delta m_d$  in order to eliminate possible experimenter's bias. We used a method that hides not only the central value for these parameters from the unbinned maximum-likelihood fit, but also the visual  $CP$  asymmetry in the  $\Delta t$  distribution. The error on both the asymmetry and  $\Delta m_d$  is not hidden.

The amplitude of the asymmetry  $\mathcal{A}_{CP}(\Delta t)$  from the fit was hidden by a one-time choice of sign flip and arbitrary offset based on a user-specified key word. The sign flip hides whether a change in the analysis increases or decreases the resulting asymmetry. However, the magnitude of the change is not hidden. The visual  $CP$  asymmetry in the  $\Delta t$  distribution is hidden by multiplying  $\Delta t$  by the sign of the tag and adding an arbitrary offset.

With these techniques, systematic studies can be performed while keeping the numerical value of  $\sin 2\beta$  or  $\Delta m_d$  hidden. In particular, we can check that the hidden  $\Delta t$  distributions are consistent for  $B^0$  and  $\bar{B}^0$  tagged events. The same is true for all the other checks concerning tagging, vertex resolution and the correlations between them. For instance, fit results in the different tagging categories can be compared to each other, since each fit is hidden in the same way. The analysis procedure for extracting  $\sin 2\beta$  and  $\Delta m_d$  were frozen prior to unblinding.

## VII. $B^0$ FLAVOR OSCILLATIONS AND MISTAG RATES

### A. Likelihood fit results for $\Delta m_d$

We extract  $\Delta m_d$ , the dilution factors  $\mathcal{D}_i$ , the  $\Delta t$  resolution parameters  $\hat{a}_i$ , and the background  $\Delta t$  parameterization by fitting the  $\Delta t$  distributions of the flavor-eigenstate  $B^0$  sample with  $m_{\text{ES}} > 5.2 \text{ GeV}/c^2$  with the likelihood function described in Section VI. The selection of the  $B_{\text{flav}}$  data sample is described in Section III C 1.

We also demand a valid tag and  $\Delta t$  determination for the event, based on the algorithms described in Sections IV and V. The more restrictive requirements  $|\Delta t| < 20 \text{ ps}$  and  $\sigma_{\Delta t} < 1.4 \text{ ps}$  are applied to the proper time-difference measurement. In addition, identified kaons in the  $B_{\text{tag}}$  decay are rejected in the reconstruction of the tagging vertex. These requirements are intended to reduce systematic errors on the precision  $\Delta m_d$  measurement. The final sample consists of 12310 fully-reconstructed and tagged  $B^0$  candidates with  $m_{\text{ES}} > 5.2 \text{ GeV}/c^2$ , of which 7399 are in the signal region  $m_{\text{ES}} > 5.27 \text{ GeV}/c^2$ .

The breakdown of this mixing  $B_{\text{flav}}$  sample into individual tagging categories is shown in Fig. 23 as a function of  $m_{\text{ES}}$ . Superimposed on the observed mass spectra are the results of the fits with a Gaussian distribution for the signal and the ARGUS background function for the background. The tagging efficiency and signal purity for the individual tagging categories in data are extracted from fits to the  $m_{\text{ES}}$  distributions and are listed in Table XII. The efficiency for each tagging category is defined as the ratio of the number of signal events for each tag over the total number of signal events after imposition of vertex cuts.

TABLE XII: Tagging efficiencies for hadronic  $B^0$  decays and signal purities in data, shown separately for the four tagging categories. Signal purities are estimated for  $m_{\text{ES}} > 5.27 \text{ GeV}/c^2$ .

Tagging Category	Efficiency [%]	Signal	Purity [%]
Lepton	$11.8 \pm 0.3$	$1097 \pm 34$	$96.0 \pm 0.7$
Kaon	$33.9 \pm 0.5$	$3156 \pm 63$	$84.6 \pm 0.7$
NT1	$8.6 \pm 0.3$	$798 \pm 31$	$88.9 \pm 1.2$
NT2	$13.9 \pm 0.4$	$1293 \pm 43$	$79.4 \pm 1.3$
Full sample	$68.1 \pm 0.4$	$6347 \pm 89$	$85.8 \pm 0.5$

The results from the likelihood fit to the mixing sample are summarized in Table XIII. The probability to obtain a likelihood smaller than the observed value, evaluated with fast parameterized Monte Carlo simulation of a large number of similar experiments, is  $(44 \pm 1)\%$ . The  $\Delta t$  distributions of the signal ( $m_{\text{ES}} > 5.27 \text{ GeV}/c^2$ ) and background ( $m_{\text{ES}} < 5.27 \text{ GeV}/c^2$ ) candidates, overlaid with the projection of the likelihood fit, are shown in Fig. 24. In Fig. 25 the mixing asymmetry of Eq. 2 is plotted; the time-dependence of the mixing probability is clearly visible.

The tagging separation  $Q = \epsilon_{\text{tag}}(1 - 2w)^2$  is calculated from the efficiencies and the mistag rates quoted in Tables XII and XIII respectively. Summing over all tagging categories, we measure a combined effective tagging efficiency  $Q \approx 27\%$ .

Two small corrections, which are described in more detail in Sections VII B 2 and VII B 4 together with their assigned systematic errors, are applied to the output of the fit. The value of  $\Delta m_d$  obtained after applying these

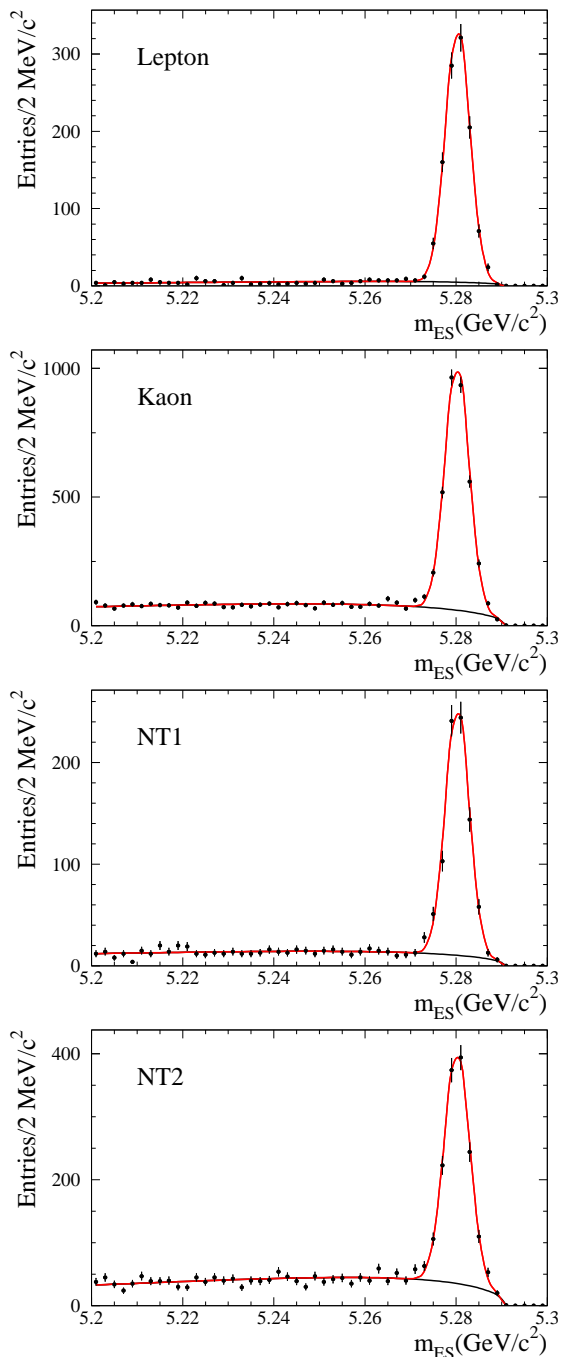


FIG. 23: Distribution of  $m_{ES}$  for mixing  $B_{\text{flav}}$  candidates in separate tagging categories (**Lepton**, **Kaon**, **NT1** and **NT2**), overlaid with the result of a fit with a Gaussian distribution for the signal and an ARGUS function for the background.

corrections is

$$\Delta m_d = 0.516 \pm 0.016 \pm 0.010 \text{ ps}^{-1},$$

where the first error is statistical and the second systematic.

We have also examined the fitted value for  $\Delta m_d$  with

various subsamples of the full data set, including individual  $B$  decay channels, separate tagging categories, the state of the reconstructed  $B_{\text{rec}}$  or tagging  $B_{\text{tag}}$ , and different time periods. As can be seen from Table XIV, the values obtained from the subsample fits are all consistent with the global result for  $\Delta m_d$ .

## B. Systematic error estimation

Systematic errors can be grouped into four categories: signal properties and description, background properties and description, fixed external parameters and statistical limitations of Monte Carlo validation tests of the fitting procedure. A summary of these sources for the hadronic  $B^0$  sample is shown in Table XV. In the following, the individual contributions are referenced by the lettered lines in this table.

### 1. Signal properties and description

For the signal events, the use of a double Gaussian plus outlier model for re-scaling the event-by-event  $\Delta t$  errors as part of the likelihood fit means that uncertainties in the vertex resolution are incorporated into the statistical error on  $\Delta m_d$ , including proper treatment of all correlations. Assuming that this model is sufficiently flexible to accommodate the observed distribution in data, no additional systematic error need be assigned. The contribution to the total statistical error due to the vertex resolution can be extracted by fitting the data twice: once holding all parameters except  $\Delta m_d$  fixed, and once allowing the resolution function parameters to vary in addition to  $\Delta m_d$ . Subtracting in quadrature the respective errors on  $\Delta m_d$  from the two fits shows that  $\pm 0.005 \text{ ps}^{-1}$  of the statistical error can be attributed to the resolution parameters.

To determine the systematic error due to the assumed parameterization of the resolution model, we apply a number of possible misalignment scenarios to a sample of simulated events. By comparing the value of  $\Delta m_d$  derived from these misaligned samples to the case of perfect alignment, we derive a systematic uncertainty of  $\pm 0.004 \text{ ps}^{-1}$  (a).

An additional systematic error is attributed to uncertainties in the treatment of the small fraction of  $\Delta t$  outliers that are the result of misreconstructed vertices. The stability of the  $\Delta m_d$  result is examined under variation of the width of the third Gaussian component in the resolution function between 6 and 18 ps, and through replacement of the third Gaussian with a uniform distribution and varying the width between 8 and 40 ps. On this basis, we attribute a systematic uncertainty of  $\pm 0.002 \text{ ps}^{-1}$  to the outlier treatment (b).

As described in detail in Section V A, the beamspot position is an integral part of the determination of  $\Delta t$ .

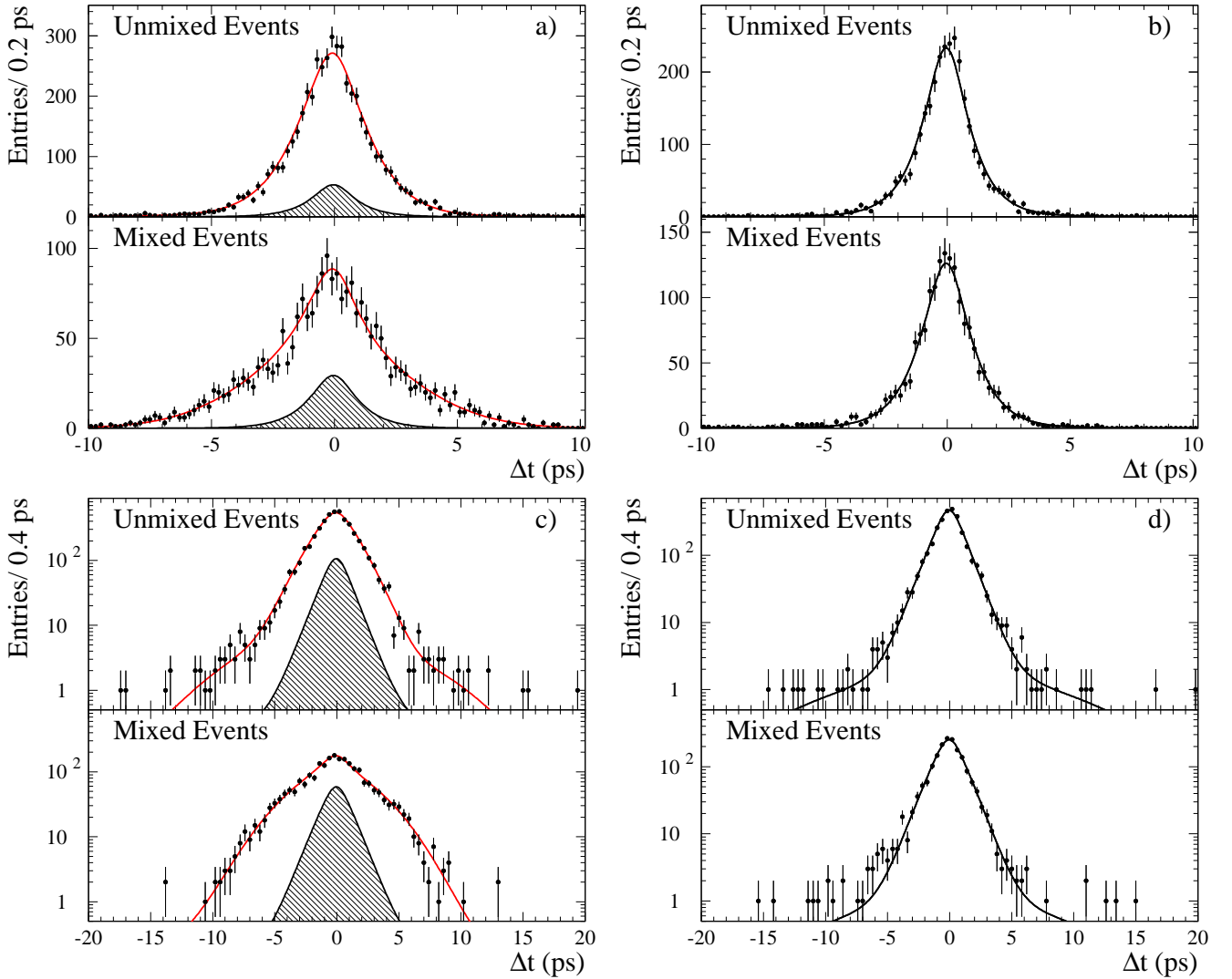


FIG. 24: Distributions of  $\Delta t$  for unmixed (upper panel) and mixed (lower panel) events in the hadronic  $B$  sample, divided into a signal region  $m_{ES} > 5.27 \text{ GeV}/c^2$  with a) a linear and c) logarithmic scale, and a sideband region  $m_{ES} < 5.27 \text{ GeV}/c^2$  with b) a linear and d) logarithmic scale. In all cases, the data points are overlaid with the result from the global unbinned likelihood fit, projected on the basis of the individual signal and background probabilities, and event-by-event  $\Delta t$  resolutions, for candidates in the respective samples. In a) and c), the  $\Delta t$  distributions obtained from the likelihood fit to the full sample are overlaid, along with the simultaneously determined background distribution shown as the curve in b) and d).

Increasing its vertical size by up to  $80 \mu\text{m}$ , and systematically biasing its vertical position by up to  $80 \mu\text{m}$ , results in a corresponding variation of  $\Delta m_d$  by less than  $0.001 \text{ ps}^{-1}$  (c).

The requirement on the maximum allowed value of  $\sigma_{\Delta t}$  is varied between 1 and  $2.4 \text{ ps}$ , and the observed variation of  $0.003 \text{ ps}^{-1}$  in  $\Delta m_d$  is assigned as a systematic uncertainty (d). The observed dependence is mainly due to correlations between tagging and vertexing, as described in Sec. VII B 4.

## 2. Background properties

A systematic uncertainty in  $\Delta m_d$  arises from our ability to separate signal from background as a function of  $m_{ES}$ . We estimate this uncertainty by varying the width and height of the fitted Gaussian peak in  $m_{ES}$ , the slope parameter of the ARGUS background shape, and the normalizations of the signal and backgrounds by one standard deviation around their central values, resulting in an uncertainty of  $\pm 0.002 \text{ ps}^{-1}$  in  $\Delta m_d$  (e).

As discussed in Sec. VIB 1, the  $\Delta t$  distribution of the background is described by the combination of a prompt component and a lifetime component. To estimate the



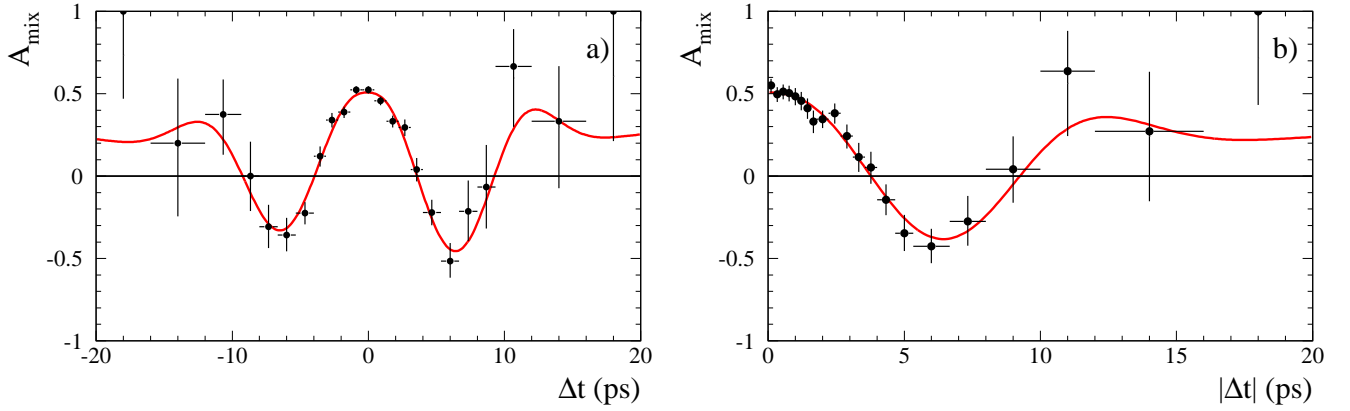


FIG. 25: Time-dependent asymmetry  $\mathcal{A}(\Delta t)$  between unmixed and mixed events for hadronic  $B$  candidates with  $m_{\text{ES}} > 5.27 \text{ GeV}/c^2$ , a) as a function of  $\Delta t$ ; and b) folded as a function of  $|\Delta t|$ . The asymmetry in a) is due to the fitted bias in the  $\Delta t$  resolution function.

systematic uncertainty due to this choice, we add an additional component, with its own separate lifetime, that is allowed to mix; the observed value of  $\Delta m_d$  changes by  $0.001 \text{ ps}^{-1}$  (f). Similarly, adding an additional Gaussian distribution to the  $\Delta t$  background resolution function changes  $\Delta m_d$  by no more than  $0.001 \text{ ps}^{-1}$  (g).

Finally, the composition of the background changes slightly as a function of  $m_{\text{ES}}$ , since the fraction of background due to continuum production slowly decreases towards the  $B$  mass. As a result, the  $\Delta t$  structure of the background could change as well. To study this dependence, we split the  $m_{\text{ES}}$  sideband region into seven mutually exclusive,  $10 \text{ MeV}/c^2$ -wide intervals, and repeat the  $\Delta m_d$  fit with each of these slices in turn. The variation of  $\Delta m_d$  is then extrapolated as a function of the position of the sideband slice relative to the  $B$  mass. We correct the value of  $\Delta m_d$  by  $-0.002 \text{ ps}^{-1}$  obtained from this extrapolation, and assign the statistical uncertainty of  $0.002 \text{ ps}^{-1}$  of this procedure as a systematic error on  $\Delta m_d$  (h).

A small fraction (about 1.5%) of the events attributed to the  $B^0$  signal by the fit to the  $m_{\text{ES}}$  distribution consists of  $B^+$  events, mainly due to the swapping of a soft  $\pi^0$  with a charged pion as described in Section III C 1. The uncertainty on this peaking fraction is propagated to  $\Delta m_d$ , yielding a systematic error of  $0.002 \text{ ps}^{-1}$  (i).

### 3. External parameters

An error in the boost of the  $\Upsilon(4S)$  system (0.1%) or in the knowledge of the  $z$  scale of the detector, as described in Section V A, could bias the  $\Delta m_d$  measurement because these parameters are used to reconstruct the decay length difference  $\Delta z$  and to convert it to the decay time difference  $\Delta t$ . The uncertainties on these quantities are propagated to  $\Delta m_d$  and lead to systematic uncertainties of  $0.001 \text{ ps}^{-1}$  (l) and less than  $0.002 \text{ ps}^{-1}$  (j), respec-

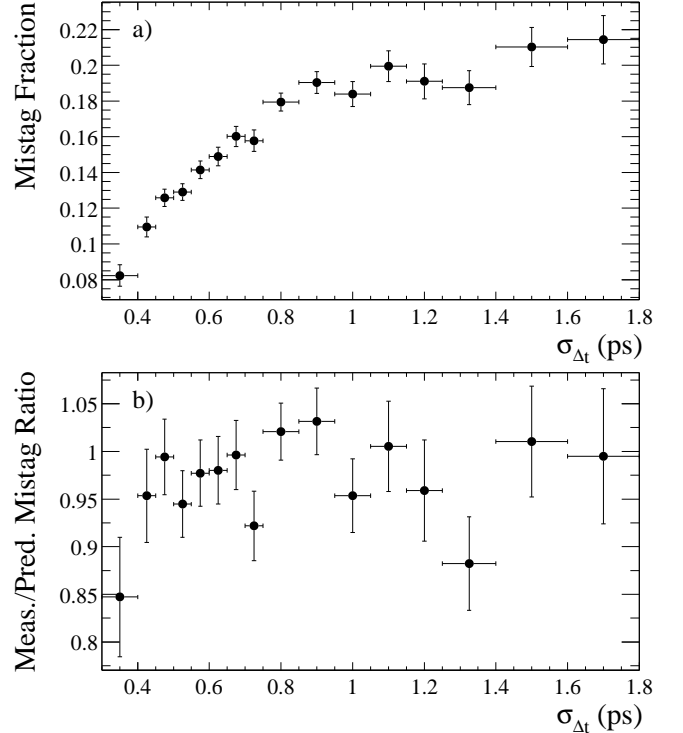


FIG. 26: a) Correlation between the event-by-event error on  $\Delta t$  ( $\sigma_{\Delta t}$ ) and the mistag rate in the Kaon category from Monte Carlo simulation; b) Dependence of mistag rate on  $\sigma_{\Delta t}$  after scaling the mistag rate by  $\sqrt{\sum p_i^2}$ .

tively. In addition to these, we assign the difference of  $0.001 \text{ ps}^{-1}$  (k) in the value of  $\Delta m_d$  obtained by using the  $\Delta z$  to  $\Delta t$  conversion described in Eq. 20 instead of Eq. 21 as a systematic error. Finally, in the likelihood fit, we fix the  $B^0$  lifetime to the PDG value [11]. The present uncertainty on this value of  $\pm 0.032 \text{ ps}$  leads to a systematic error of  $\mp 0.006 \text{ ps}^{-1}$  (m).

TABLE XIII: Results from the likelihood fit to the  $\Delta t$  distributions of the hadronic  $B^0$  decays. The value for  $\Delta m_d$  includes small corrections as described in the text. The first major column contains the fit results, while the second major column contains the correlation coefficients with respect to  $\Delta m_d$  for each fit parameter.

Parameter	Fit Result		Correlation	
	Run 1	Run 2	Run 1	Run 2
$\Delta m_d$ [ps <sup>-1</sup> ]	0.516 ± 0.016			
Signal Resolution Function				
$S_1$ (core)	1.37 ± 0.09	1.18 ± 0.11	0.25	0.16
$b_1(\Delta t)$ lepton (core)	0.06 ± 0.13	-0.04 ± 0.16	0.08	0.00
$b_1(\Delta t)$ kaon (core)	-0.22 ± 0.08	-0.25 ± 0.09	0.03	0.00
$b_1(\Delta t)$ NT1 (core)	-0.07 ± 0.15	-0.45 ± 0.21	-0.00	0.00
$b_1(\Delta t)$ NT2 (core)	-0.46 ± 0.12	-0.20 ± 0.16	0.01	0.03
$b_2(\Delta t)$ (tail)	-5.0 ± 4.2	-7.5 ± 2.4	0.04	0.06
$f_2$ (tail)	0.014 ± 0.020	0.015 ± 0.010	0.06	0.07
$f_3$ (outlier)	0.008 ± 0.004	0.000 ± 0.014	-0.09	0.01
Signal dilutions				
$\langle D \rangle$ , lepton	0.842 ± 0.028		0.24	
$\langle D \rangle$ , kaon	0.669 ± 0.023		0.30	
$\langle D \rangle$ , NT1	0.563 ± 0.044		0.11	
$\langle D \rangle$ , NT2	0.313 ± 0.041		0.11	
$\Delta D$ , lepton	-0.006 ± 0.045		0.02	
$\Delta D$ , kaon	0.024 ± 0.033		0.01	
$\Delta D$ , NT1	-0.086 ± 0.068		0.00	
$\Delta D$ , NT2	0.100 ± 0.060		0.00	
Background properties				
$\tau$ , mixing bkgd [ps]	0.853 ± 0.036		-0.01	
$f(\tau = 0)$ , mixing bkgd, lepton	0.05 ± 0.10		0.01	
$f(\tau = 0)$ , mixing bkgd, kaon	0.42 ± 0.05		0.01	
$f(\tau = 0)$ , mixing bkgd, NT1	0.33 ± 0.08		0.01	
$f(\tau = 0)$ , mixing bkgd, NT2	0.32 ± 0.08		0.01	
Background resolution function				
$S_1$ (core)	1.211 ± 0.043	1.131 ± 0.046	-0.00	0.00
$b_1(\Delta t)$ (core)	-0.135 ± 0.031	-0.015 ± 0.038	-0.00	-0.00
$f_3$ (outlier)	0.022 ± 0.004	0.036 ± 0.007	-0.01	0.02
Background dilutions				
$\langle D \rangle$ , lepton, $\tau = 0$	0.0 ± 2.9		-0.02	
$\langle D \rangle$ , kaon, $\tau = 0$	0.52 ± 0.08		-0.03	
$\langle D \rangle$ , NT1, $\tau = 0$	0.67 ± 0.27		-0.01	
$\langle D \rangle$ , NT2, $\tau = 0$	-0.05 ± 0.13		-0.00	
$\langle D \rangle$ , lepton, $\tau > 0$	0.34 ± 0.13		0.02	
$\langle D \rangle$ , kaon, $\tau > 0$	0.26 ± 0.06		0.04	
$\langle D \rangle$ , NT1, $\tau > 0$	-0.13 ± 0.11		0.01	
$\langle D \rangle$ , NT2, $\tau > 0$	0.12 ± 0.031		0.01	

#### 4. Monte Carlo validation of measurement technique

Candidate selection criteria, or the analysis and fitting procedure, could potentially cause systematic biases in the measurement of  $\Delta m_d$ . These potential biases are estimated by repeating the analysis with a large sample of Monte Carlo events, which are generated with the full GEANT3 [27] detector simulation. In the Monte Carlo sample, the fitted result for  $\Delta m_d$  is shifted by  $+0.007 \pm 0.003$  ps<sup>-1</sup> from the input value. A corresponding correction with this central value is applied to the fitted result with data, and the uncertainty is assigned as a systematic error (n).

The main cause of this bias is a small correlation be-

tween the mistag rate and the  $\Delta t$  resolution that is not modeled in the likelihood function. This correlation is seen most readily in data for Kaon tags and is shown for simulation in Fig. 26a. We find that both the mistag rate for kaon tags and the event-by-event error  $\sigma_{\Delta t}$  depend inversely on  $\sqrt{\sum p_t^2}$ , where  $p_t$  is the transverse momentum with respect to the  $z$  axis of tracks from the  $B_{\text{tag}}$  decay. Correcting for this dependence of the mistag rate removes most of the correlation between the mistag rate and  $\sigma_{\Delta t}$ , as can be seen in Fig. 26b. The mistag rate dependence originates from the kinematics of the physics sources for wrong-charge kaons. The three major sources of mistags are wrong-sign  $D^0$  mesons from  $B$  decays to double charm, wrong-sign kaons from  $D^+$  decays, and

TABLE XIV: Result of fitting for  $\Delta m_d$  in the entire  $B_{\text{flav}}$  sample and in various subsamples. The difference in the fitted value of  $\Delta m_d$  versus the result from the fit to the full  $B_{\text{flav}}$  sample are reported.

Sample	$\Delta m_d - \Delta m_d(\text{all})$
<b>Decay mode</b>	
$D^{*-}\pi^+$	$-0.029 \pm 0.030$
$D^{*-}\rho^+$	$+0.017 \pm 0.039$
$D^{*-}a_1^+$	$+0.066 \pm 0.063$
$D^-\pi^+$	$+0.022 \pm 0.030$
$D^-\rho^+$	$-0.031 \pm 0.038$
$D^-a_1^+$	$-0.033 \pm 0.041$
$D^{*-}X$	$+0.000 \pm 0.025$
$D^-X$	$-0.005 \pm 0.023$
<b>Tagging category</b>	
<b>Lepton</b>	$+0.005 \pm 0.026$
<b>Kaon</b>	$+0.002 \pm 0.023$
<b>NT1</b>	$-0.032 \pm 0.044$
<b>NT2</b>	$+0.12 \pm 0.10$
<b><math>B_{\text{rec}}</math> state</b>	
$B_{\text{rec}} = \bar{B}^0$	$+0.015 \pm 0.023$
$B_{\text{rec}} = B^0$	$-0.003 \pm 0.023$
<b><math>B_{\text{tag}}</math> state</b>	
$B_{\text{tag}} = \bar{B}^0$	$+0.019 \pm 0.023$
$B_{\text{tag}} = B^0$	$-0.007 \pm 0.022$
<b>Data sample</b>	
Run 1	$-0.012 \pm 0.022$
Run 2	$+0.019 \pm 0.025$

kaons produced directly in  $B$  decays. All these sources produce a spectrum of charged tracks that have smaller  $\sqrt{\sum p_t^2}$  than  $B$  decays that produce a correct tag. The  $\Delta t$  resolution dependence originates from the  $1/p_t^2$  dependence of  $\sigma_z$  for the individual contributing tracks.

Since the effect is small and well described by the Monte Carlo simulation, we have chosen to treat the impact of this correlation as a correction, rather than building the effect into the likelihood function. We include additional systematic errors related to the tag-side properties that could affect the accuracy of the description of this correlation in the simulation. In particular, the  $D^0$ ,  $D^+$ , and  $D_s^+$  meson branching fractions, the  $D$  meson lifetimes, and the wrong-sign kaon production rates in  $B$  meson decays are all varied. These studies lead to an assigned systematic error of  $\pm 0.001 \text{ ps}^{-1}$  (o).

In addition, we consider the possibility that correctly and incorrectly tagged events could have different resolution functions. Based on Monte Carlo studies of the variation in the fitted value for  $\Delta m_d$  with and without allowing for independent resolution functions for correctly and incorrectly tagged events, an uncertainty of  $\pm 0.001 \text{ ps}^{-1}$  is assigned to this source (p).

TABLE XV: Systematic uncertainties and contributions to statistical errors for  $\Delta m_d$  obtained with the likelihood fit to the hadronic  $B^0$  sample.

Source	$\sigma(\Delta m_d)$ [ps <sup>-1</sup> ]
<b>Signal properties</b>	
(a) SVT alignment	0.004
(b) $\Delta t$ outlier description	0.002
(c) Beamspot position/size	0.001
(d) $\sigma_{\Delta t}$ requirement	0.003
<b>Background properties</b>	
(e) Background fraction	0.002
(f) Background $\Delta t$ structure	0.001
(g) Background $\Delta t$ resolution	0.001
(h) Sideband extrapolation	0.002
(i) Peaking $B^+$ background	0.002
<b>External parameters</b>	
(j) $z$ scale	<0.002
(k) $z$ boost (parameters)	0.001
(l) $z$ boost (method)	0.001
(m) $B^0$ lifetime	0.006
<b>Monte Carlo studies</b>	
(n) Signal MC statistics	0.003
(o) Tag-side $D$ composition & lifetime	0.001
(p) Right/wrong tag resolution differences	0.001
Total systematic error	0.010
Statistical error	0.016
Contribution due to resolution function	0.005
Contribution due to mistag rate	0.005
<b>Total error</b>	<b>0.019</b>

## C. Validation studies and cross checks

### 1. Monte Carlo studies

A high-precision test of the fitting procedure was performed with fast parameterized Monte Carlo simulations, where 2000 experiments were generated with sample size and composition corresponding to that obtained from the actual data. The mistag rates and  $\Delta t$  distributions were generated according to the model used in the likelihood fit. The full fit was then performed on each of these experiments. The resulting distribution of pulls (defined as the difference between the fitted and generated value of a parameter divided by the statistical error as obtained from the likelihood fit) has a mean  $-0.038 \pm 0.022$  and standard deviation  $1.012 \pm 0.023$ , consistent with no measurement bias in either the value of  $\Delta m_d$  or its estimated error.

### 2. Simple counting experiment

If the mistag rate is known, the time-integrated fraction  $\chi_d = \frac{1}{2}x_d/(1+x_d^2)$  of mixed events can be determined from the  $B_{\text{flav}}$  sample by counting mixed and unmixed

events. The value for  $\chi_d$  obtained by this means, after correcting for the mistag rates obtained from the full time-dependent fit and assuming the PDG value for the  $B^0$  lifetime, leads to a value of  $\Delta m_d = x_d/\tau_{B^0}$  that differs from the likelihood-fit result by  $-0.003 \pm 0.013 \text{ ps}^{-1}$ , where the quoted error is the difference in quadrature of the statistical errors of both measurements.

Due to the choice for normalization of the likelihood  $\mathcal{L}_{\text{mix}}$ , the time-integrated ratio of the number of mixed to unmixed events contributes to our measurement of  $\Delta m_d$ . Alternatively, it is possible to normalize the likelihoods of mixed and unmixed events individually, in which case  $\Delta m_d$  is determined solely from the shape of  $\Delta t$  distributions. The value of  $\Delta m_d$  determined by the  $\Delta t$  distributions alone differs from the full measurement by  $0.003 \pm 0.015 \text{ ps}^{-1}$ , where the quoted error is given by the difference in quadrature of the statistical errors of the two measurements.

### 3. Cross check with $\tau_{B^0}$

If we allow the value of  $\tau_{B^0}$  to float in the  $\Delta m_d$  fit the value of  $\Delta m_d$  increases by  $0.008 \pm 0.007 \text{ ps}^{-1}$ , and the lifetime is found to be  $1.51 \pm 0.03 \text{ ps}$ , consistent with our recent measurement [17]. We have also performed a series of fits with fixed values for  $\Delta m_d$  and  $\tau_{B^0}$  in order to determine the dependence of  $\Delta m_d$  on  $\tau_{B^0}$ , which is found to be

$$\Delta m_d = \left[ 0.516 - 0.279 \left( \frac{\tau_{B^0}}{1.548 \text{ ps}} - 1 \right) \right] \text{ ps}^{-1}. \quad (42)$$

## VIII. CP VIOLATION IN NEUTRAL B DECAYS

### A. Likelihood fit results for $\sin 2\beta$

The value of  $\sin 2\beta$ , the dilution factors  $\mathcal{D}_i$ , the  $\Delta t$  resolution parameters  $\hat{a}_i$ , and the background fractions and time distribution parameters are extracted with an unbinned maximum-likelihood fit to the flavor-eigenstate  $B_{\text{flav}}$  and  $B_{CP}$  samples as described in Section VI. We also demand a valid tag and  $\Delta t$  determination for the event, based on the algorithms described in Sections IV and V. The looser requirements  $|\Delta t| < 20 \text{ ps}$  and  $\sigma_{\Delta t} < 2.4 \text{ ps}$  are applied to the proper time difference measurement. The fit results are summarized in Table XVI together with the correlation of the parameters with  $\sin 2\beta$ . The mistag fractions and vertex parameters are predominantly determined by the  $B_{\text{flav}}$  sample. The  $CP$  asymmetry and parameters describing the background for the  $CP$  events are determined by the  $CP$  sample. The value of  $\sin 2\beta$  obtained from the combined  $\eta_{CP} = -1$ ,  $\eta_{CP} = +1$ , and  $J/\psi K^{*0}$   $CP$  samples is

$$\sin 2\beta = 0.59 \pm 0.14 \pm 0.05,$$

where the first error is statistical and the second systematic.

The  $m_{ES}$  distribution for events in  $\eta_{CP} = -1$  modes, separated into tagging categories, is shown in Fig. 27. The signal probability  $f_{i,\text{sig}}^{CP}(m_{ES})$  for the  $\eta_{CP} = -1$  sample is determined from these fits as described in Section VIB 1.

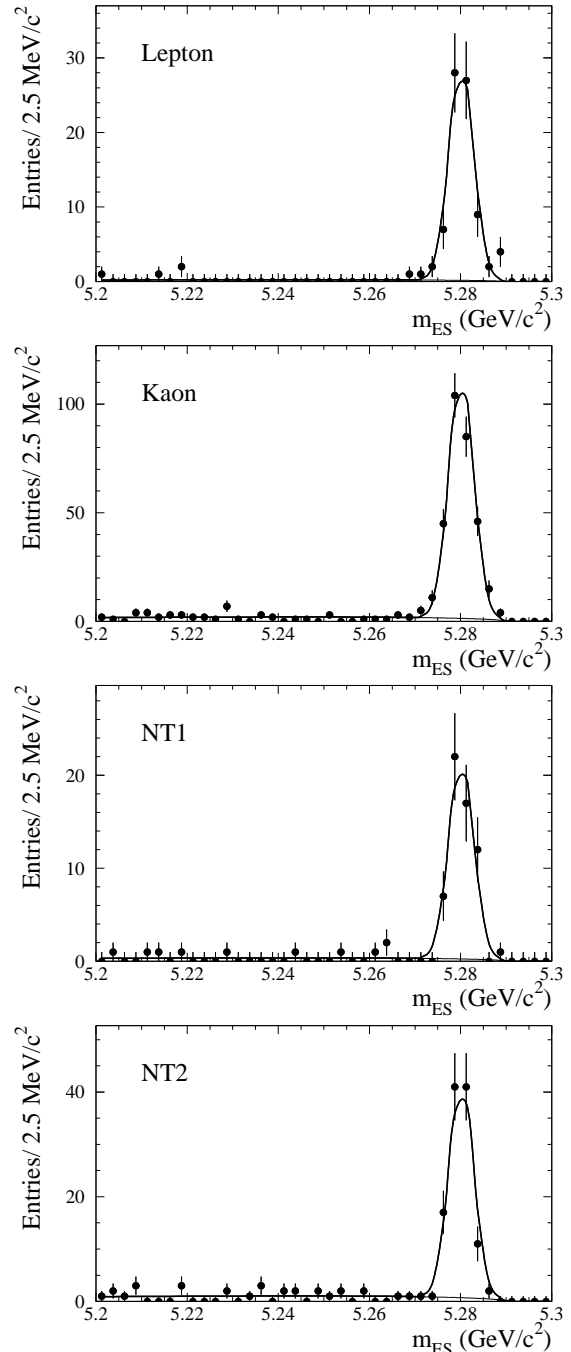


FIG. 27: Distribution of  $m_{ES}$  for  $\eta_{CP} = -1$  candidates in separate tagging categories (Lepton, Kaon, NT1 and NT2), overlaid with the result of a fit with a Gaussian distribution for the signal and an ARGUS function for the background.

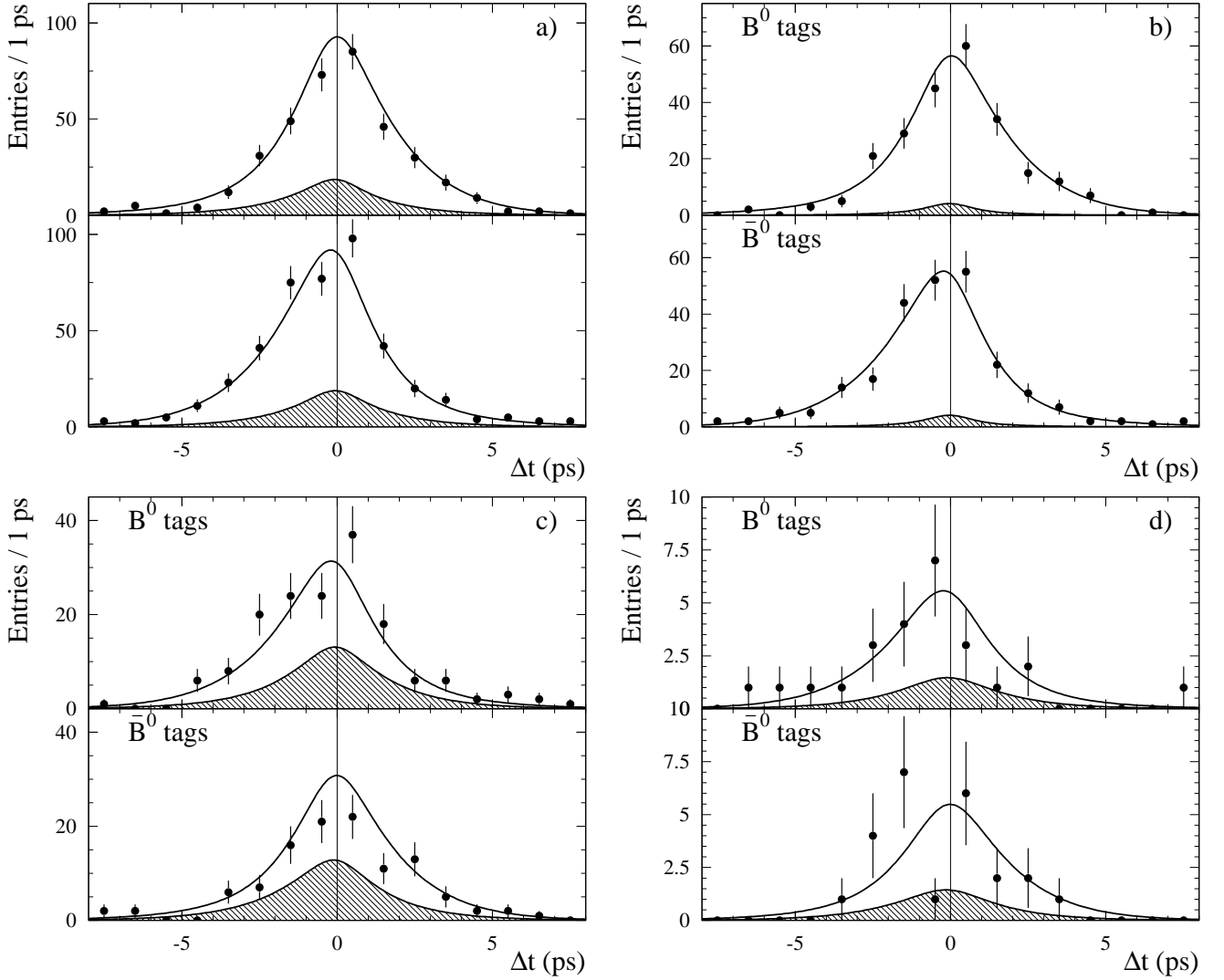


FIG. 28: a) Distribution of  $\Delta t$  for tagged events in the full  $CP$  sample. The upper (lower) panel is the sum of  $B^0$  ( $\bar{B}^0$ )-tagged events in the  $\eta_{CP} = -1$  and  $J/\psi K^{*0}$  samples, combined with the  $\bar{B}^0$  ( $B^0$ )-tagged events in the  $J/\psi K_L^0$  sample. Corresponding  $B^0$ - (lower panel) and  $\bar{B}^0$ -tagged (upper panel) distributions for the b)  $\eta_{CP} = -1$ , c)  $J/\psi K_L^0$ , and d)  $J/\psi K^{*0}$  samples are also shown. In all cases, the data points are overlaid with the result from the global unbinned likelihood fit, projected on the basis of the individual signal and background probabilities, and event-by-event  $\Delta t$  resolutions, for candidates in the respective samples. Therefore, the curves correspond to  $\sin 2\beta = 0.59$ , rather than the fitted value obtained with the individual subsample. The probability-weighted  $\Delta t$  spectra of the background candidates obtained from the fit are indicated by the shaded areas.

Table XVII summarizes the event yields and  $\sin 2\beta$  values determined for the full  $CP$  sample and various subsamples. Results are provided by  $CP$  channel, tagging category,  $B^0$  versus  $\bar{B}^0$  tag,  $J/\psi$  decay mode and data-taking period. The consistency between the six  $CP$  modes is satisfactory, the probability of finding a worse agreement being 8%. The large observed asymmetry in  $B^0 \rightarrow \chi_{c1} K_S^0$  causes the likelihood for this channel to become negative in certain regions of  $\Delta t$ . The likelihood of each of the selected candidates is of course positive. Fast parameterized Monte Carlo studies show that  $\sin 2\beta$  is unbiased if the likelihood is not required to be positive for all values of  $\Delta t$  and that the probability to measure

such a large asymmetry is about 1%. The observed asymmetry in the number of  $B^0$  (160) and  $\bar{B}^0$  (113) tags in the  $J/\psi K_L^0$  sample has no impact on the  $\sin 2\beta$  measurement. The results obtained with the full  $B_{CP}$  samples for Run 1 and Run 2 are consistent at the 1.8 sigma level. The yields and fitted values for  $\sin 2\beta$  are also listed in Table XVII for the high purity  $\eta_{CP} = -1$  sample alone, along with a similar breakdown into subsamples; again, no significant variation is seen.

The distribution of events as a function of  $\Delta t$  for  $B^0$  and  $\bar{B}^0$  tags is shown in Fig. 28a for the full  $CP$  sample. For this purpose, only those events with  $m_{ES} > 5.27 \text{ GeV}/c^2$  in the  $\eta_{CP} = -1$  and  $J/\psi K^{*0}$  samples or

$\Delta E < 10$  MeV in the  $\eta_{CP} = +1$  sample are included. Overlaid on the data are the projections of the signal and background  $\Delta t$  distributions obtained from the fit, where the latter is normalized to the projected background level. Figure 28b-d shows the corresponding  $\Delta t$  distributions for the  $\eta_{CP} = -1$ ,  $\eta_{CP} = +1$  samples and  $B^0 \rightarrow J/\psi K^{*0}$  ( $K^{*0} \rightarrow K_s^0 \pi^0$ ,  $K_s^0 \rightarrow \pi^+ \pi^-$ ). The superimposed likelihood curves show the quality of the fit for each subsample. The value of  $\sin 2\beta$  obtained by fixing all other parameters to results obtained with the full  $CP$  sample and then fitting for  $\sin 2\beta$  in bins of  $\Delta t$  is shown in Fig. 29a. The values obtained for  $\sin 2\beta$  are all consistent, demonstrating that the oscillation as a function of  $\Delta t$  has the expected behavior. The observed asymmetry  $\mathcal{A}(\Delta t)$  is shown in Fig. 29b and c for the  $\eta_{CP} = -1$  and  $\eta_{CP} = +1$  samples respectively, along with the projections from the fit results.

The average dilutions and dilution differences for  $B^0$  and  $\bar{B}^0$  tags obtained from the fit to the  $B^0$  flavor eigenstate and full  $CP$  sample, and the corresponding tagging efficiencies, are summarized in Table XVIII. We find a total tagging efficiency of  $(68.4 \pm 0.7)\%$  (statistical error only). The lepton categories have the lowest mistag fractions, but also have low efficiency. The Kaon category, despite having a larger mistag fraction (17.6%), has a higher effective tagging efficiency; one-third of events are assigned to this category. Altogether, lepton and kaon categories have an effective tagging efficiency  $Q \approx 22.4\%$ . The neural network categories increase the effective tagging efficiency by  $\sim 4\%$  to an overall  $Q = (26.1 \pm 1.2)\%$  (statistical error only). These mistag fractions are very similar to the mistag fraction that are obtained from the  $B_{\text{flav}}$  sample alone (see Table XIII). The small differences are due to the correlation between the mistag fractions and the  $\Delta t$  resolution function parameters.

Based on a large number of fast parameterized Monte Carlo experiments with the same number of events as our full  $B_{CP}$  and  $B_{\text{flav}}$  data samples, we estimate a probability of 27% for finding a value of the maximum likelihood lower than that observed. These same studies, based on samples with the size and composition of the data, show that the expected statistical error is 0.132 with a spread of 0.005, in very good agreement with the observed error of 0.137.

## B. Systematic error estimation

Just as for the  $\Delta m_d$  measurement, systematic errors can usefully be grouped into signal description, including detector reconstruction effects, background description, fixed external parameters, and statistical limitations of Monte Carlo validation tests for the fitting procedure (discussed in Section VIII C 1). A summary of these sources of systematic error is shown in Table XIX for the various  $CP$  samples. In the following, the individual contributions are referenced by the lettered lines in this table.

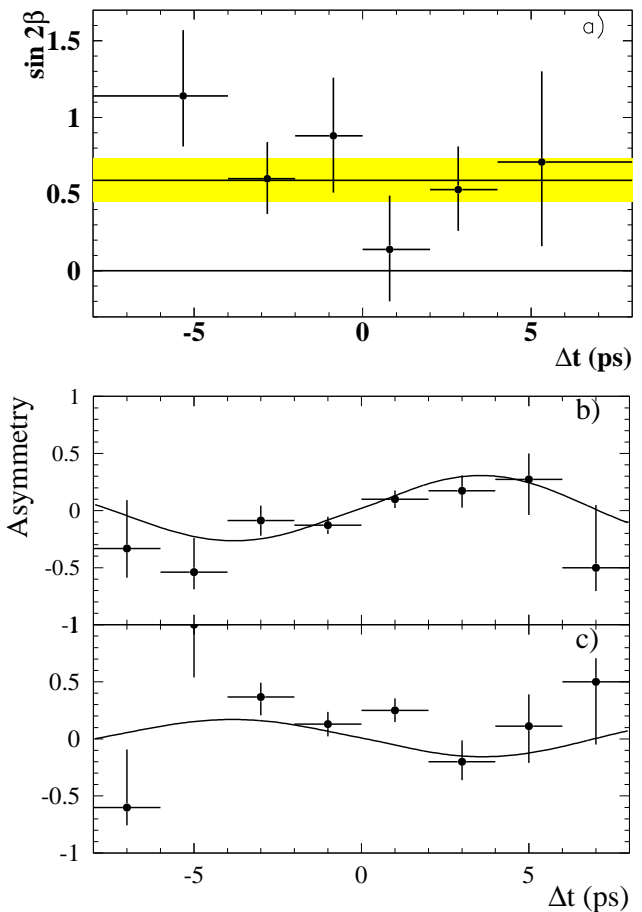


FIG. 29: a) Fitted value of  $\sin 2\beta$  obtained in bins of  $\Delta t$  by fixing all other parameters to the values obtained with the full  $CP$  sample; Raw asymmetry in the number of  $B^0$  and  $\bar{B}^0$  tags in the signal region,  $(N_{B^0} - N_{\bar{B}^0})/(N_{B^0} + N_{\bar{B}^0})$ , with asymmetric binomial errors, as a function of  $\Delta t$  for b)  $\eta_{CP} = -1$  and c)  $J/\psi K_L^0$  samples. The data points are overlaid with the separate fit results for the two samples.

### 1. Signal properties and description

The parameters of the  $\Delta t$  resolution function, the dilutions and dilution differences are determined from the data sample itself with the likelihood fit. Thus, they do not contribute to the systematic error, but rather are incorporated into the statistical uncertainty at a level determined by the size of the data sample itself. Their overall contribution to the total error on  $\sin 2\beta$  is 0.02, as determined from the difference in quadrature between the statistical error on  $\sin 2\beta$  from the full likelihood fit and from a fit with only  $\sin 2\beta$  allowed to vary.

While the bulk of the uncertainties from these sources is thus incorporated into the statistical error, we assign additional systematic uncertainties due to the fixed form of the parameterization for the  $\Delta t$  resolution function. This form may not be flexible enough to account for all

TABLE XVI: Parameters for the combined likelihood fit to the  $B_{CP}$  and  $B_{\text{flav}}$  samples. The first major column contains the fit results, while the second major column contains the correlation coefficients with respect to  $\sin 2\beta$  for each fit parameter.

Parameter	Fit Result		Correlation	
	Run 1	Run 2	Run 1	Run 2
$\sin 2\beta$	$0.59 \pm 0.14$			
Signal Resolution Function				
$S_1$ (core)	$1.2 \pm 0.1$	$1.1 \pm 0.1$	0.018	0.020
$b_1(\Delta t)$ lepton (core)	$0.07 \pm 0.12$	$0.04 \pm 0.16$	0.008	0.045
$b_1(\Delta t)$ kaon (core)	$-0.26 \pm 0.08$	$-0.18 \pm 0.09$	0.002	0.021
$b_1(\Delta t)$ NT1 (core)	$-0.21 \pm 0.15$	$-0.33 \pm 0.21$	0.004	0.001
$b_1(\Delta t)$ NT2 (core)	$-0.31 \pm 0.11$	$-0.17 \pm 0.15$	-0.001	-0.002
$b_2(\Delta t)$ (tail)	$-1.7 \pm 1.5$	$-3.3 \pm 2.8$	0.001	0.006
$f_2(\text{tail})$	$0.08 \pm 0.06$	$0.04 \pm 0.04$	0.009	0.005
$f_3(\text{outlier})$	$0.005 \pm 0.003$	$0.000 \pm 0.001$	-0.001	0.000
Signal dilutions				
$\langle D \rangle$ , lepton	$0.82 \pm 0.03$		-0.042	
$\langle D \rangle$ , kaon	$0.65 \pm 0.02$		-0.083	
$\langle D \rangle$ , NT1	$0.56 \pm 0.04$		-0.015	
$\langle D \rangle$ , NT2	$0.30 \pm 0.04$		-0.032	
$\Delta D$ , lepton	$-0.02 \pm 0.04$		0.010	
$\Delta D$ , kaon	$0.04 \pm 0.03$		0.005	
$\Delta D$ , NT1	$-0.11 \pm 0.06$		0.014	
$\Delta D$ , NT2	$0.12 \pm 0.05$		-0.008	
Background properties				
$\tau$ , mixing bkgd [ps]	$1.3 \pm 0.1$		-0.001	
$f(\tau = 0)$ , CP bkgd	$0.60 \pm 0.12$		-0.011	
$f(\tau = 0)$ , mixing bkgd, lepton	$0.31 \pm 0.10$		-0.001	
$f(\tau = 0)$ , mixing bkgd, kaon	$0.65 \pm 0.04$		-0.001	
$f(\tau = 0)$ , mixing bkgd, NT1	$0.62 \pm 0.06$		-0.001	
$f(\tau = 0)$ , mixing bkgd, NT2	$0.64 \pm 0.04$		-0.001	
Background resolution function				
$S_1$ (core)	$1.5 \pm 0.1$	$1.3 \pm 0.1$	0.004	-0.003
$b_1(\Delta t)$ core [ps]	$-0.16 \pm 0.03$	$0.02 \pm 0.04$	0.000	-0.001
$f_2(\text{outlier})$	$0.016 \pm 0.004$	$0.017 \pm 0.005$	-0.001	0.000
Background dilutions				
$\langle D \rangle$ , lepton, $\tau = 0$	$0.33 \pm 0.27$		0.003	
$\langle D \rangle$ , kaon, $\tau = 0$	$0.45 \pm 0.03$		0.008	
$\langle D \rangle$ , NT1, $\tau = 0$	$0.25 \pm 0.10$		0.002	
$\langle D \rangle$ , NT2, $\tau = 0$	$0.11 \pm 0.06$		0.003	
$\langle D \rangle$ , lepton, $\tau > 0$	$0.33 \pm 0.14$		0.000	
$\langle D \rangle$ , kaon, $\tau > 0$	$0.24 \pm 0.06$		0.000	
$\langle D \rangle$ , NT1, $\tau > 0$	$0.05 \pm 0.14$		-0.001	
$\langle D \rangle$ , NT2, $\tau > 0$	$0.09 \pm 0.09$		0.000	

possible effects. In addition, tests of the assumption that the resolution function and dilution parameters are the same for the  $B_{\text{flav}}$  and  $B_{CP}$  samples are limited in precision by the size of the available Monte Carlo samples.

The resolution function, described in Section VD, is one of several possible functional forms. In order to test possible biases induced by this particular choice, an alternative model has been considered where a Gaussian distribution is convolved with an exponential, with the effective lifetime in the exponential depending on the tagging category. No difference between the fit results with the two models is observed in Monte Carlo simulation. We assign as a systematic uncertainty the difference in the fit results observed in the data (Table XIX, line a).

The largest systematic uncertainties from the  $\Delta t$  behavior arises from possible effects that our model of the resolution function cannot accommodate or completely parameterize. These include residual uncertainties in the SVT alignment (b) and possible differences in the  $\Delta t$  determination for correctly and incorrectly tagged events (c). An additional uncertainty is assigned due to the treatment of the  $\Delta t$  outliers (d). Fits with Monte Carlo samples of  $B_{\text{flav}}$  and  $B_{CP}$  signal events show no significant difference between resolution function parameters for the two samples. We assign a systematic uncertainty of  $\pm 0.003$  due to the residual shift in  $\sin 2\beta$  between the two sets of fitted  $\Delta t$  resolution parameters (e).

An underlying assumption of the global fit is that di-

TABLE XVII: Result of fitting for  $CP$  asymmetries in the entire  $CP$  sample and in various subsamples. The yields are obtained with likelihood fits and are therefore background subtracted.

Sample	$N_{\text{tag}}$	Purity (%)	$\sin 2\beta$	$Im\lambda/ \lambda $	$ \lambda $
<b><math>CP</math> sample</b>	803	80	<b><math>0.59 \pm 0.14</math></b>		
$J/\psi K_S^0 (K_S^0 \rightarrow \pi^+ \pi^-)$	316	98	$0.45 \pm 0.18$	$0.45 \pm 0.18$	$0.91 \pm 0.11$
$J/\psi K_S^0 (K_S^0 \rightarrow \pi^0 \pi^0)$	64	94	$0.70 \pm 0.50$	$0.71 \pm 0.50$	$0.95 \pm 0.27$
$\psi(2S)K_S^0 (K_S^0 \rightarrow \pi^+ \pi^-)$	67	98	$0.47 \pm 0.42$	$0.48 \pm 0.45$	$1.22 \pm 0.33$
$\chi_{c1}K_S^0 (K_S^0 \rightarrow \pi^+ \pi^-)$	33	97	$2.59 \pm_{0.67}^{0.55}$	$2.67 \pm 0.59$	$0.71 \pm 0.23$
$J/\psi K_L^0$	273	51	$0.70 \pm 0.34$		
$J/\psi K^{*0} (K^{*0} \rightarrow K_S^0 \pi^0, K_S^0 \rightarrow \pi^+ \pi^-)$	50	74	$0.82 \pm 1.00$		
<b>Lepton</b>	130	82	$0.54 \pm 0.26$		
<b>Kaon</b>	438	79	$0.58 \pm 0.18$		
<b>NT1</b>	79	74	$0.89 \pm 0.30$		
<b>NT2</b>	156	80	$0.40 \pm 0.65$		
$B^0$	420	79	$0.54 \pm 0.19$		
$\bar{B}^0$	383	78	$0.64 \pm 0.20$		
$J/\psi \rightarrow e^+ e^-$	385	78	$0.49 \pm 0.20$		
$J/\psi \rightarrow \mu^+ \mu^-$	418	84	$0.70 \pm 0.18$		
Run 1	533	80	$0.49 \pm 0.20$		
Run 2	270	84	$0.82 \pm 0.22$		
<b><math>\eta_{CP} = -1</math> sample</b>	480	96	$0.56 \pm 0.15$	$0.56 \pm 0.15$	$0.93 \pm 0.09$
<b>Lepton</b>	74	100	$0.54 \pm 0.29$	$0.57 \pm 0.29$	$0.77 \pm 0.14$
<b>Kaon</b>	271	98	$0.59 \pm 0.20$	$0.59 \pm 0.20$	$0.98 \pm 0.12$
<b>NT1</b>	46	97	$0.67 \pm 0.45$	$0.57 \pm 0.46$	$0.73 \pm 0.29$
<b>NT2</b>	89	95	$0.10 \pm 0.74$	$0.28 \pm 1.29$	$2.95 \pm 3.83$
$B^0$	234	98	$0.50 \pm 0.22$		
$\bar{B}^0$	246	97	$0.61 \pm 0.22$		
$J/\psi \rightarrow e^+ e^-$	219	94	$0.54 \pm 0.22$	$0.52 \pm 0.22$	$1.00 \pm 0.15$
$J/\psi \rightarrow \mu^+ \mu^-$	261	98	$0.60 \pm 0.21$	$0.63 \pm 0.21$	$0.87 \pm 0.11$
Run 1	310	95	$0.37 \pm 0.20$	$0.37 \pm 0.20$	$1.16 \pm 0.15$
Run 2	170	98	$0.86 \pm 0.24$	$0.96 \pm 0.26$	$0.66_{+0.12}^{-0.11}$
<b>Control samples</b>					
$B^0 \rightarrow D^{(*)-} \pi^+ / \rho^+ / a_1^+$	7579	84	$0.00 \pm 0.04$		
$B^+ \rightarrow \bar{D}^{(*)0} \pi^+$	6800	86	$-0.02 \pm 0.04$		
$B^0 \rightarrow J/\psi K^{*0} (K^{*0} \rightarrow K^+ \pi^-)$	705	95	$0.12 \pm 0.12$		
$B^+ \rightarrow J/\psi K^{(*)+}, \psi(2S)K^+$	2031	94	$0.07 \pm 0.07$		

TABLE XVIII: Average mistag fractions  $w_i$  and mistag differences  $\Delta w_i = w_i(B^0) - w_i(\bar{B}^0)$  extracted for each tagging category  $i$  from the maximum-likelihood fit to the time distribution for the fully-reconstructed  $B^0$  sample ( $B_{\text{flav}} + B_{CP}$ ). The figure of merit for tagging is the effective tagging efficiency  $Q_i = \varepsilon_i(1 - 2w_i)^2$ , where  $\varepsilon_i$  is the fraction of events with a reconstructed tag vertex that are assigned to the  $i^{\text{th}}$  category.  $\varepsilon_i$  is computed for the  $\eta_{CP} = \pm 1$  samples as well as the combined  $B_{CP}$  and  $B_{\text{flav}}$  samples. Uncertainties are statistical only. The statistical error on  $\sin 2\beta$  is proportional to  $1/\sqrt{Q}$ , where  $Q = \sum Q_i$ .

Category	$\eta_{CP} = -1$	$\eta_{CP} = +1$	$B_{\text{flav}} + B_{CP}$			
	$\varepsilon$ [%]	$\varepsilon$ [%]	$\varepsilon$ [%]	$w$ [%]	$\Delta w$ [%]	$Q$ [%]
<b>Lepton</b>	$11.0 \pm 1.2$	$10.4 \pm 3.0$	$10.9 \pm 0.3$	$9.0 \pm 1.4$	$0.9 \pm 2.2$	$7.4 \pm 0.5$
<b>Kaon</b>	$38.9 \pm 1.9$	$28.3 \pm 4.5$	$35.8 \pm 1.0$	$17.6 \pm 1.0$	$-1.9 \pm 1.5$	$15.0 \pm 0.9$
<b>NT1</b>	$6.9 \pm 0.9$	$4.8 \pm 2.3$	$7.8 \pm 0.3$	$22.0 \pm 2.1$	$5.6 \pm 3.2$	$2.5 \pm 0.4$
<b>NT2</b>	$13.0 \pm 0.4$	$13.9 \pm 3.3$	$13.8 \pm 0.3$	$35.1 \pm 1.9$	$-5.9 \pm 2.7$	$1.2 \pm 0.3$
<b>All</b>	$69.8 \pm 2.7$	$57.4 \pm 6.7$	$68.4 \pm 0.7$			$26.1 \pm 1.2$

lutions and dilution differences are the same for the  $B_{\text{flav}}$  and  $B_{CP}$  samples. We assign the full difference as seen in Monte Carlo simulation as systematic error,  $\pm 0.027$  (f). In addition, the  $B^\pm$  data sample was used to study

any possible dependence of the dilutions on  $\Delta t$ . No significant effect was observed. However, a dependence of the dilutions on  $\sigma_{\Delta t}$  has been seen, both in data and the Monte Carlo simulation (see Section VII B 4). Finally, it



TABLE XIX: Summary of contributions to the systematic error on  $\sin 2\beta$ ,  $Im\lambda/|\lambda|$  and  $|\lambda|$ . Note that the last two measurements use only the  $\eta_{CP} = -1$  sample.

Source	CP Sample					
	$\eta_{CP} = -1$	$J/\psi K_L^0$	$J/\psi K^{*0}$	Full	$Im\lambda/ \lambda $	$ \lambda $
Signal parameters						
(a) $\Delta t$ signal resolution model	$\pm 0.009$	$\pm 0.01$	$\pm 0.07$	$\pm 0.009$	$\pm 0.003$	$\pm 0.003$
(b) SVT alignment	$\pm 0.027$					$\pm 0.012$
(c) $\Delta t$ for right/wrong tagged events	$\pm 0.012$				$\pm 0.011$	$\pm 0.003$
(d) $\Delta t$ signal resolution outliers	$\pm 0.002$	$\pm 0.018$	$\pm 0.03$	$\pm 0.002$	$\pm 0.003$	$\pm 0.002$
(e) $\Delta t$ signal resolution	$\pm 0.003$					$\pm 0.009$
(f) Signal dilutions for CP vs. $B_{flav}$	$\pm 0.027$					$\pm 0.011$
(g) Tagging Efficiencies	$\pm 0.003$				$\pm 0.004$	$\pm 0.012$
Background properties: $\eta_{CP} = -1$						
(h) Background fraction	$\pm 0.006$	—	—	$\pm 0.005$	$\pm 0.006$	$\pm 0.004$
(i) CP bkgd peaking component	$\pm 0.004$	—	—	$\pm 0.003$	$\pm 0.005$	$\pm 0.001$
(j) CP bkgd CP content (ARGUS)	$\pm 0.015$	—	—	$\pm 0.015$	$\pm 0.015$	$\pm 0.001$
(k) CP bkgd CP content (Peak)	$\pm 0.004$	—	—	$\pm 0.004$	$\pm 0.004$	$\pm 0.001$
(l) CP bkgd effective lifetime	0	—	—	0	0	0
(m) CP bkgd resolution	$\pm 0.002$	—	—	$\pm 0.002$	$\pm 0.002$	$\pm 0.001$
Background properties: $J/\psi K_L^0$						
(n) Background fraction	—	$\pm 0.075$	—	$\pm 0.01$	—	—
(o) $\Delta E$ distribution	—	$\pm 0.04$	—	$\pm 0.007$	—	—
(p) Effective CP of backgrounds	—	$\pm 0.020$	—	$\pm 0.001$	—	—
(q) Background composition	—	$\pm 0.014$	—	$\pm 0.002$	—	—
(r) Background $\Delta t$ and dilution	—	$\pm 0.023$	—	$\pm 0.003$	—	—
Background properties: $J/\psi K^{*0}$						
(s) Sample composition	—	—	$\pm 0.08$	$\pm 0.001$	—	—
(t) $R_{\perp}$	—	—	$\pm 0.08$	$\pm 0.001$	—	—
Background properties: $B_{flav}$						
(u) Background fraction	$\pm 0.001$	$\pm 0.008$	$\pm 0.003$	$\pm 0.002$	$\pm 0.002$	$\pm 0.001$
(v) $B_{flav}$ bkgd mixing contrib.	$\pm 0.001$	$\pm 0.002$	$\pm 0.001$	$\pm 0.002$	$\pm 0.001$	0
(w) $B_{flav}$ bkgd peaking component	0	$\pm 0.001$	$\pm 0.001$	0	0	0
External parameters						
(x) z scale and boost	$\pm 0.003$					$\pm 0.001$
(y) Beam spot	$\pm 0.002$					$\pm 0.006$
(z) $B^0$ lifetime	$\pm 0.008$	$\pm 0.011$	$\pm 0.022$	$\pm 0.009$	$\pm 0.009$	$\pm 0.012$
(aa) $\Delta m_d$	$\pm 0.015$	$\pm 0.012$	$\pm 0.082$	$\pm 0.013$	$\pm 0.015$	$\pm 0.001$
Monte Carlo studies						
(bb) Monte Carlo statistics	$\pm 0.012$					$\pm 0.007$
Total systematic error	$\pm 0.05$	$\pm 0.10$	$\pm 0.16$	$\pm 0.05$	$\pm 0.05$	$\pm 0.02$
Statistical error	$\pm 0.15$	$\pm 0.34$	$\pm 1.01$	$\pm 0.14$	$\pm 0.15$	$\pm 0.09$

is possible that tagging efficiencies could be different for  $B^0$  and  $\bar{B}^0$  mesons. A separate study of the relative tagging efficiencies is described in Section VIII D, since the relative efficiencies form an important part of the direct CP violation search. The systematic error on  $\sin 2\beta$  due to this effect is estimated to be  $\pm 0.003$  (g).

## 2. Background properties

The fraction of background events in the  $\eta_{CP} = -1$  sample is estimated from fits to the  $m_{ES}$  distribution. Varying this fraction within the stated errors and changing the signal probability as a function of  $m_{ES}$  results in a systematic error of  $\pm 0.005$  on  $\sin 2\beta$  (h). The uncer-

tainty on the fraction of peaking background contributes a systematic error of  $\pm 0.003$  (i). Varying the effective  $\sin 2\beta$  assumed for the ARGUS ( $\mathcal{A}$  in Section VIB 1) and peaking ( $\delta_{peak}$  in Section VIB 1) backgrounds in the CP sample from  $-1$  to  $+1$  contributes a systematic error of  $\pm 0.015$  (j) and  $\pm 0.004$  (k), respectively. In addition, the contributions due to the uncertainty of the  $\Delta t$  resolution model ( $\pm 0.002$ ), and the effective lifetime (negligible) of the CP background, have been evaluated (l-m).

For the  $B^0 \rightarrow J/\psi K_L^0$  channel, the signal and non- $J/\psi$  background fractions are varied within their statistical uncertainties ( $\pm 1\sigma$ ) as obtained with the fit to the  $\Delta E$  distribution of the sample. This contributes a systematic error of  $\pm 0.075$  to the  $B^0 \rightarrow J/\psi K_L^0$   $\sin 2\beta$  result and  $\pm 0.01$  to the final result (n). We also vary back-

ground parameters for the  $B^0 \rightarrow J/\psi K_L^0$  sample, including the  $J/\psi X$  branching fractions according to Table VI, the assumed  $\eta_{CP}$ , the mistag rates and efficiencies, the  $\Delta t$  resolution function, and  $\Delta E$  shape (o-r). The total  $B^0 \rightarrow J/\psi K_L^0$  background systematic error, summing these contributions in quadrature, is  $\pm 0.09$  for the  $\sin 2\beta$  fit to the  $B^0 \rightarrow J/\psi K_L^0$  sample alone and  $\pm 0.013$  for the full sample.

For the  $B^0 \rightarrow J/\psi K^{*0}$  ( $K_S^0 \pi^0$ ) sample, the value of  $R_\perp$  as well as the sample composition are varied (s-t) according to Table V.

The effect of the uncertainty on background component in the  $B_{\text{flav}}$  sample on  $\sin 2\beta$  has also been evaluated. The only significant sources of uncertainty are the fraction of background that mixes (v) and the signal probability distribution as a function of  $m_{\text{ES}}$  (u,w).

### 3. External parameters

The residual uncertainty on the physical  $z$  scale (x) and the boost parameters of the  $\Upsilon(4S)$  center of mass (y) contribute systematic uncertainties. We fix the  $B^0$  lifetime to the current world average values  $\tau_{B^0} = 1.548$  ps and  $\Delta m_d = 0.472$  ps $^{-1}$  [11]. The errors on  $\sin 2\beta$  due to uncertainties in  $\tau_{B^0}$  and  $\Delta m_d$  are  $\pm 0.009$  and  $\pm 0.013$ , respectively (z-aa).

### 4. Monte Carlo validation of measurement technique

The analysis method has been studied with a high-statistics Monte Carlo sample. A fit result that is consistent with the generated value for  $\sin 2\beta$  was found. We assign a  $\pm 0.012$  systematic error due to the statistical limitation of the Monte Carlo sample size (bb). Section VIII C 1 describes this study in more detail.

## C. Validation studies and cross checks

We have used data and Monte Carlo samples to perform validation studies of the analysis technique. These tests include studies with parameterized Monte Carlo samples, full GEANT3 [27] simulation samples, as well as data samples where no  $CP$  asymmetry is expected.

### 1. Monte Carlo studies

The highest precision test of the fitting procedure was performed with fast parameterized Monte Carlo simulation, where 1000 experiments were generated with sample sizes corresponding to the observed  $B_{\text{flav}}$  and  $B_{CP}$  events in data, including mistag rates,  $\Delta t$  resolutions, and background fractions and time dependence. The full fit is performed on each of these experiments. The resulting pull distribution (defined as the difference between the fitted

and generated value of a parameter divided by the statistical error as obtained from the likelihood fit) has a mean  $-0.029 \pm 0.032$  and standard deviation  $1.007 \pm 0.022$ , consistent with no measurement bias in either the value of  $\sin 2\beta$  or its estimated error.

In addition, large samples of signal and background Monte Carlo events generated with a GEANT3 [27] detector simulation are used to validate the measurement. For these tests, we obtained the resolution function parameters as well as the dilutions from a Monte Carlo sample of  $B_{\text{flav}}$  events. Using these parameters, we fit for  $\sin 2\beta$  in Monte Carlo samples of  $CP$  signal events that correspond in number to the reconstructed data sample. These Monte Carlo events are generated with various values of  $\sin 2\beta$  (0.1 to 0.9) and different  $CP$ -eigenstate modes, corresponding to those used in the measurement with data. The mean and spread of the pull distribution for these Monte Carlo samples can be used to check for any measurement bias and to confirm the validity of the reported error. We find that the mean pull is consistent with zero and the spread is consistent with the reported error. A systematic error of  $\pm 0.012$  is assigned to  $\sin 2\beta$  due to the limited Monte Carlo statistics for this test.

The effect of background has been evaluated by adding an appropriate fraction of background events to our signal Monte Carlo sample and performing the likelihood fit. The background samples are obtained either from simulated  $B \rightarrow J/\psi X$  events or  $\Delta E$  sidebands in data ( $|\Delta E| < 120$  MeV but outside the signal region). We find no significant bias for  $\sin 2\beta$  with the addition of either source of background.

### 2. Cross checks with $\tau_{B^0}$ and $\Delta m_d$

Table XX shows results for  $\sin 2\beta$  if  $\Delta m_d$  and  $\tau_{B^0}$  are allowed to float in the combined fit to the  $CP$  and  $B_{\text{flav}}$  samples. The fitted value of  $\Delta m_d$  is somewhat larger than that reported in Section VII. However, with no kaon veto applied to the tagging vertex, the correction for the bias introduced by known correlations between mistag rates and the  $\Delta t$  resolution is also larger. Taking this into account, the two results are consistent within the independent statistical errors. Likewise the lifetime is found to be consistent with our recent measurement [17]. We have also performed fits with  $\Delta m_d$  and  $\tau_{B^0}$  fixed to a series of values around the world average in order to determine the dependence of  $\sin 2\beta$  on these two parameters, thereby finding that

$$\sin 2\beta = \left[ 0.59 - 0.35 \left( \frac{\Delta m_d}{0.472 \text{ ps}^{-1}} - 1 \right) - 0.45 \left( \frac{\tau_{B^0}}{1.548 \text{ ps}} - 1 \right) \right]. \quad (43)$$

TABLE XX: Results when  $\Delta m_d$  and (or)  $\tau_{B^0}$  are floated in the  $\sin 2\beta$  fit to the full  $CP$  sample and the  $\eta_{CP} = -1$  sub-sample alone.

Fit	$\sin 2\beta$	$\Delta m_d$ ( $\text{ps}^{-1}$ )	$\tau_{B^0}$ (ps)
All $CP$ modes			
Nominal fit	$0.59 \pm 0.14$	0.472	1.548
Float $\Delta m_d$	$0.55 \pm 0.13$	$0.533 \pm 0.015$	1.548
Float $\tau_{B^0}$	$0.60 \pm 0.14$	0.472	$1.53 \pm 0.03$
Float $\Delta m_d$ and $\tau_{B^0}$	$0.56 \pm 0.13$	$0.542 \pm 0.016$	$1.50 \pm 0.03$
$\eta_{CP} = -1$ modes			
Nominal fit	$0.56 \pm 0.15$	0.472	1.548
Float $\Delta m_d$	$0.51 \pm 0.15$	$0.531 \pm 0.015$	1.548
Float $\tau_{B^0}$	$0.57 \pm 0.15$	0.472	$1.53 \pm 0.03$
Float $\Delta m_d$ and $\tau_{B^0}$	$0.52 \pm 0.15$	$0.540 \pm 0.016$	$1.50 \pm 0.03$

### 3. Asymmetries in data control samples

Control samples in data where the reconstructed  $B^0$  and  $B^+$  meson decays to a flavor-eigenstate mode with a  $D^{(*)}$  or charmonium meson in the final state can be used to validate the  $\sin 2\beta$  measurement, since the asymmetry is expected to be zero in this case. For these samples, the  $\Delta t$  resolution function parameters and the dilutions are fixed to the values obtained with the  $B_{\text{flav}}$  sample. The  $CP$  asymmetry and the fraction of prompt background (identical for each tagging category, as is the case for the fit to the  $CP$  data sample) are allowed to float. The measured asymmetries are all consistent with zero, as shown in Table XVII. The observed  $\Delta t$  distributions for the  $B^0$ - and  $\bar{B}^0$ -tagged events in the  $B_{\text{flav}}$  sample is shown in Fig. 30a, where good agreement is clearly visible. Figure 30b demonstrates that there is no visible asymmetry as a function of  $\Delta t$ .

Control samples are also used to check the assumption that the  $\Delta t$  resolution function, which is primarily determined by the  $B_{\text{flav}}$  sample, can be applied to the charmonium decay modes in the  $CP$  sample. Figure 31 graphically compares the fitted  $\Delta t$  resolution function for the  $B^+ \rightarrow D^{(*)}X$  control sample with that of the  $B^+ \rightarrow c\bar{c}X$  control sample. A  $1\sigma$  error envelope encompasses the fit to the  $B^+ \rightarrow c\bar{c}X$  sample, which has five times fewer events. The level of agreement is acceptable. The same comparison between the  $B^0 \rightarrow D^{(*)}X$  and  $B^0 \rightarrow c\bar{c}X$  samples was inconclusive due to the low statistics of the  $B^0 \rightarrow c\bar{c}X$  sample.

### 4. Time-integrated measurement of mistag rates

As described in Section I, a time-integrated technique can also be used to measure the mistag fractions in data, thereby providing a simple check of the likelihood fit method. The statistical precision of the time-integrated measurement is enhanced by restricting the sample to events in a single optimized  $\Delta t$  interval. Taking into account detector vertex resolution, the optimal interval is

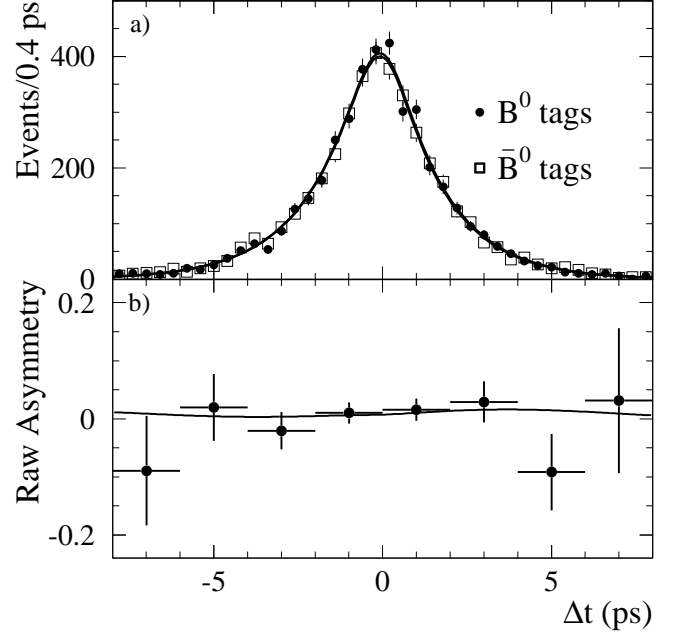


FIG. 30: a) Distribution in  $\Delta t$  for  $B^0$ - and  $\bar{B}^0$ -tagged and b) observed asymmetry for events in the flavor-eigenstate  $B^0$  sample. The projections of the likelihood fit for the  $B^0$ - and  $\bar{B}^0$ -tagged samples are shown in a) as the overlapping solid lines.

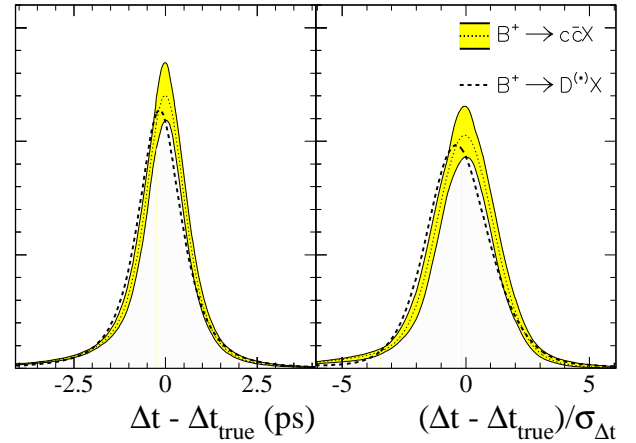


FIG. 31: Comparison of the fitted  $\Delta t$  resolution obtained with the data control samples  $B^+ \rightarrow D^{(*)}X$  and  $B^+ \rightarrow c\bar{c}X$ , showing the fitted distribution for a)  $\delta_t = \Delta t - \Delta t_{\text{true}}$  and b) the normalized difference  $\delta_t/\sigma_{\Delta t}$ . The one sigma error envelope from the fit to the  $B^+ \rightarrow c\bar{c}X$  sample (shaded region), overlaps the central value for the five-times larger  $B^+ \rightarrow D^{(*)}X$  sample (dashed line).

found to be  $|\Delta t| < 2.5$  ps. Events with  $|\Delta t| > 2.5$  ps have, on average, equal numbers of mixed and unmixed events due to flavor oscillations, and therefore contribute nothing to the determination of the mistag rate. We refer

to this time-integrated technique using a single optimized  $\Delta t$  interval as the “single-bin” method and apply it to both the  $B_{\text{flav}}$  sample described in Section III C 1 and the semileptonic  $B^0$  sample described in Section III E.

To correct for the presence of backgrounds, a term is added to Eq. 14 to account for the contribution of each background source to the fraction of mixed events in the sample:

$$\chi_{\text{obs}} = f_{\text{sig}}(\chi_d + (1 - 2\chi_d)w) + \sum_{\beta} f_{\beta}\chi_{\beta}, \quad (44)$$

where  $f_{\text{sig}}$  and  $f_{\beta}$  are the fraction of signal and background source  $\beta$ , respectively,  $\chi_{\beta}$  is the fraction of mixed events in each background source, and  $\chi_{\text{obs}}$  is the observed fraction of mixed events. In this expression,  $\chi_d$  must also be modified to represent the integrated mixing probability for  $|\Delta t| < 2.5$  ps. Using the world-average values for  $\Delta m_d$  and  $\tau_{B^0}$  [11], and taking into account the  $\Delta t$  resolution function  $\mathcal{R}(\Delta t)$ , we find

$$\chi'_d = \frac{1}{2} \left[ 1 - \int e^{-|\Delta t|/\tau} \cos(\Delta m_d \Delta t) \otimes \mathcal{R}(\Delta t) d(\Delta t) / \int e^{-|\Delta t|/\tau} \otimes \mathcal{R}(\Delta t) d(\Delta t) \right] = 0.079, \quad (45)$$

where the integral is performed over the range  $|\Delta t| < 2.5$  ps and  $\mathcal{R}(\Delta t)$  is modeled by a double-Gaussian distribution with five parameters (one fraction, two biases and two widths) determined directly from data using the hadronic sample. Solving Eq. 44 for  $w$ , and using the calculated value for  $\chi'_d$ , the mistag rates are obtained:

$$w = \frac{\chi_{\text{obs}} - f_{\text{sig}}\chi'_d - \sum_{\beta} f_{\beta}\chi_{\beta}}{f_{\text{sig}}(1 - 2\chi'_d)}. \quad (46)$$

TABLE XXI: Yields, efficiencies, mistag rates  $w$ , and tagging separation  $Q = \epsilon_{\text{tag}}(1 - 2w)^2$  as measured by the single-bin method in the hadronic  $B_{\text{flav}}$  event sample. A comparison of the mistag rates measured in the same sample with the single-bin method,  $w_{\text{sb}}$ , and the likelihood fit,  $w_{\text{like}}$  (Table XVIII), are reported as the differences  $\Delta_{\text{like}} = w_{\text{sb}} - w_{\text{like}}$  between the two extraction techniques, normalized to the uncorrelated statistical and systematic errors.

Category	Yield	Efficiency [%]	Mistag rate $w$ [%]	$Q$ [%]	$\Delta_{\text{like}}$ [ $\sigma$ ]
Lepton	1128	$11.0 \pm 0.3$	$9.5 \pm 1.5 \pm 0.6$	7.2	-0.8
Kaon	3687	$35.8 \pm 0.5$	$17.8 \pm 1.0 \pm 0.7$	14.8	-0.4
NT1	819	$7.9 \pm 0.3$	$22.0 \pm 2.2 \pm 0.9$	2.5	+0.0
NT2	1428	$13.9 \pm 0.3$	$34.3 \pm 1.9 \pm 1.1$	1.4	+0.8

All tagged events in the  $B_{\text{flav}}$  sample with  $|\Delta t| < 2.5$  ps are used for a single-bin study. The combinatorial background fraction in the signal sample is determined from a fit to the  $m_{\text{ES}}$  distribution as described in Section VII. The signal region is defined as events

with  $m_{\text{ES}} > 5.27$  GeV/ $c^2$ . The  $B^+$  peaking background in this signal is estimated to be  $(1.3 \pm 0.8)\%$ . The fraction of mixed events in the combinatorial background is determined by tagging category with the sideband control sample,  $5.20 < m_{\text{ES}} < 5.27$  GeV/ $c^2$ , and the mistag fraction associated with the  $B^+$  peaking background has been measured directly in data. The number of tagged events in each category is summarized in Table XXI.

TABLE XXII: Yields, efficiencies, mistag rate  $w$ , and tagging separation  $Q = \epsilon_{\text{tag}}(1 - 2w)^2$  as measured by the single-bin method in the semileptonic  $B^0$  event sample. A comparison of the mistag rates measured with the single-bin method are reported as the differences  $\Delta_{\text{sample}} = w_{\text{flav}} - w_{\text{sl}}$  between the mistag rates in the  $B_{\text{flav}}$  sample,  $w_{\text{flav}}$  (Table XXI), and semileptonic  $B^0$  samples,  $w_{\text{sl}}$ , normalized to the quadratic sum of statistical and uncorrelated systematic errors.

Category	Yield	Efficiency [%]	Mistag rate $w$ [%]	$Q$ [%]	$\Delta_{\text{sample}}$ [ $\sigma$ ]
Lepton	3046	$11.9 \pm 0.4$	$8.7 \pm 0.9 \pm 1.4$	8.1	+0.4
Kaon	10270	$36.2 \pm 1.9$	$19.5 \pm 0.7 \pm 1.2$	13.5	-1.1
NT1	2127	$8.1 \pm 0.4$	$22.3 \pm 1.4 \pm 1.2$	2.5	-0.1
NT2	3967	$13.5 \pm 0.9$	$36.0 \pm 1.2 \pm 1.3$	1.1	-0.7

A separate single-bin analysis is also performed with the sample of  $B^0 \rightarrow D^{*-}\ell^+\bar{\nu}$  events described in Section III E. We use tagged events with  $|\Delta t| < 2.5$  ps and evaluate the backgrounds for events in this time interval. The backgrounds and mixed-event fractions are evaluated separately for each tagging category. Backgrounds are larger for the semileptonic modes than for the hadronic modes and originate from a variety of sources. In the case of the combinatorial background, the estimate is obtained from the  $m(\bar{D}^0\pi^-) - m(\bar{D}^0)$  sideband. For the continuum background, off-resonance data is used after correction for the combinatorial component. The mixed-event fraction for  $B\bar{B}$  background is estimated with generic  $B\bar{B}$  Monte Carlo simulation. The mistag fraction of the last background component, the decay  $B^+ \rightarrow D^*X\ell\bar{\nu}$ , has been determined with data. The estimates of the contributions of the various backgrounds are described in Section III E. The number of tagged events in each category are summarized in Table XXII.

We use Eq. 46 to obtain the mistag rates in each tagging category shown in Table XXI for the  $B_{\text{flav}}$  sample and Table XXII for the  $B^0$  semileptonic sample. The sources of systematic error on these results are summarized in Tables XXIII and XXIV respectively.

Three sources of systematic uncertainties are common to both the hadronic and semileptonic samples. The first is the uncertainty due to the errors on the world-average values for the  $B^0$  lifetime and  $\Delta m_d$  values. The second is due to the  $\Delta t$  resolution function, whose fit parameters in data are varied within errors. The third common uncertainty is related to the possibility that wrong tags have worse  $\Delta t$  resolution than correct tags. This effect has

TABLE XXIII: Sources of systematic error for the mistag measurement on the  $B_{\text{flav}}$  sample in the single-bin method.

Type	Variation	Lepton	Kaon	NT1	NT2
$\tau(B^0), \Delta m_d$	$\pm 1\sigma$	0.005	0.004	0.003	0.002
Resolution	see text	0.002	0.002	0.001	0.001
Wrong-tag resolution	see text	0.003	0.006	0.007	0.009
Combinatorial bkgd	$\pm 1\sigma$	0.002	0.002	0.005	0.004
$B^\pm$ peaking bkgd	$\pm 1\sigma$	0.001	0.001	0.000	0.000
Total		0.006	0.007	0.009	0.011

TABLE XXIV: Sources of systematic error for the mistag measurement from the semileptonic  $B^0$  sample in the single-bin method.

Type	Variation	Lepton	Kaon	NT1	NT2
$\tau(B^0), \Delta m_d$	$\pm 1\sigma$	0.006	0.004	0.004	0.002
Resolution	see text	0.001	0.001	0.001	0.001
Wrong-tag resolution	see text	0.003	0.006	0.007	0.009
Combinatorial bkgd	$\pm 1\sigma$	0.001	0.006	0.004	0.004
Continuum bkgd	$\pm 1\sigma$	0.001	0.003	0.006	0.007
$B\bar{B}$ bkgd	$\pm 1\sigma$	0.011	0.005	0.005	0.004
$B^+ \rightarrow D^* X \ell \bar{\nu}$ bkgd	$\pm 1\sigma$	0.003	0.004	0.002	0.001
Total		0.014	0.012	0.012	0.013

been studied with Monte Carlo simulation, where we observe a slightly larger RMS width for events with wrong-sign tags. From this study, scale factors comparing the right and wrong-tag resolution functions have been extracted and then applied to the resolution function for wrong tags.

The systematic uncertainties unique to each sample are due to the background components. These are estimated by varying both the background fractions  $f_\beta$  and the fraction of mixed events associated with each background source,  $\chi_\beta$ , by one standard deviation in their uncertainty.

For the semileptonic sample, the systematic error due to backgrounds is the dominant source. The characterization of these various backgrounds is described in Section III E. For the combinatorial background fraction, a relative systematic uncertainty of 20% is added in quadrature to the statistical error to cover the range of results obtained with various  $m(\bar{D}^0\pi^-) - m(\bar{D}^0)$  fitting functions.

The systematic error due to the continuum background is determined by varying both the background level and the mixed fractions. The  $B\bar{B}$  background fraction uncertainty is obtained by combining the statistical uncertainty and the systematic error given in Section III E. The systematic errors introduced by uncertainties on the background from the decay  $B^+ \rightarrow D^* X \ell \bar{\nu}$  are obtained by varying the fraction described in Section III E as well as the mistag fraction of  $B^+$  mesons measured on data. Studies with Monte Carlo simulation have been

performed to verify that the mistag fractions are not affected by the presence of the extra pions in the decay  $B^+ \rightarrow D^* X \ell \bar{\nu}$ . An additional uncertainty due to the statistical precision of the Monte Carlo study has been added to the charged  $B$  mistag fractions measured with data.

Table XXI shows the difference  $\Delta_{\text{like}} = w_{\text{sb}} - w_{\text{like}}$  between the mistag rates measured with the single-bin method in the  $B_{\text{flav}}$  sample,  $w_{\text{sb}}$ , and the likelihood fit result,  $w_{\text{like}}$  (Table XVIII). The difference is reported in terms of the uncorrelated statistical and systematic errors for the two methods, when applied to the same data sample. The component of uncorrelated statistical error is estimated with a fast parameterized Monte Carlo simulation. It varies with category due to different event yields. The differences  $\Delta_{\text{sample}} = w_{\text{flav}} - w_{\text{sl}}$  in the mistag rates measured with the single-bin method in the  $B_{\text{flav}}$  sample,  $w_{\text{flav}}$ , and in the semileptonic  $B^0$  sample,  $w_{\text{sl}}$ , are reported in Table XXII. The quadratic sum of the statistical and uncorrelated systematic errors is used to estimate the consistency of the measurements.

### 5. Vertexing algorithm checks

In order to verify that the results are stable under variation of the vertexing algorithm that is used for the measurement of  $\Delta t$ , several less powerful alternatives to the default method have been considered:

- **Charmonium mass constraint for vertex fit:** The mass constraint on the charmonium daughter, used in the selection of the events, is also applied in the determination of the vertex.
- **No  $K_s^0$  mass constraint:** The mass constraint on the  $K_s^0$  candidate is not applied during the vertex reconstruction.
- **No Bremsstrahlung recovery:** Only events without an associated Bremsstrahlung photon for the  $J/\psi$  daughter electrons are considered in the likelihood fit.
- **Charmonium daughters only:** The vertex of the fully reconstructed  $B$  meson is reconstructed only with the tracks from the charmonium daughter.
- **No converted photon veto:** Pairs of tracks from gamma conversions are retained in the vertex fit.
- **$\sigma_{\Delta t}$  requirement:** Only events with  $\sigma_{\Delta t} < 1.4$  ps are retained, as is required in the mixing analysis.
- **Boost approximation:** The boost approximation (Eq. 20) is used to convert the  $\Delta z$  measurement into  $\Delta t$ .
- **Kaon veto:** The more restrictive requirement from the mixing analysis that no kaons participate in the tagging vertex is applied.

- **No  $\Upsilon(4S)$  constraint:** The algorithm described in section V A is simplified by dropping the  $\Upsilon(4S)$  momentum constraint.
- **Dilution dependence on  $\sigma_{\Delta t}$ :** Dilutions for the kaon category are parameterized as a function of the error on  $\Delta t$ .

A summary of the results obtained with these different configurations for the  $\Delta t$  determination is provided in Fig 32. In all cases the variation of the measured asymmetry is consistent with the error assigned to the parameterization of the resolution function.

### 6. $J/\psi K_L^0$ background cross checks

As a cross check, a likelihood fit was performed to  $J/\psi K_L^0$  candidates in a  $\Delta E$  sideband region ( $20 < \Delta E < 80$  MeV) treated entirely as signal events. This sample is actually a mixture of  $B$  decay modes with an expected average  $\eta_{CP}$  of +0.04. The true value for  $\sin 2\beta$  in the Monte Carlo simulation is 0.7 and consequently the expected result from the likelihood fit to the  $\Delta t$  distribution of the control sample is 0.03. The actual fits to sideband regions in data and Monte Carlo simulation find  $\sin 2\beta = 0.16 \pm 0.18$  and  $-0.03 \pm 0.10$  respectively, both of which are consistent with expectations.

As another cross check, a sample of  $J/\psi K_S^0$  events was selected in the data, where only the  $K_S^0$  direction information was used, thereby emulating the  $K_L^0$  selection. The purity and background composition of this control sample is very similar to that of the  $J/\psi K_L^0$  sample. However, in this case, the subset of true  $J/\psi K_S^0$  events can be identified with the normal  $J/\psi K_S^0$  selection criteria. A fit to the  $\Delta E$  distribution of the full control sample finds  $(49 \pm 3)\%$  signal, which is in good agreement with the fraction, 47%, observed for the cleanly identified  $J/\psi K_S^0$  subset. Likewise, a likelihood fit to the  $\Delta t$  distribution of the full control sample agrees well with the value of  $\sin 2\beta$  obtained with the true  $J/\psi K_S^0$  subsample.

### 7. Graphical display of the asymmetry

An elegant display of the  $CP$  asymmetry in the data can be obtained with the use of the so-called  $\mathcal{K}$ in variable, hereafter denoted as  $\mathcal{K}$ . It is also possible to verify directly the fitted value for  $\sin 2\beta$  from the ratio of appropriate weighted averages for  $\mathcal{K}$ . In particular,  $\mathcal{K}$  has a PDF with an asymmetry known to be linearly dependent with a slope given by  $\sin 2\beta$  regardless of the details of the analysis.

Writing the PDF  $\mathcal{F}_+(\mathcal{F}_-)$  for events with a  $B^0$  ( $\bar{B}^0$ ) tag in terms of the general functions  $F_1(\Delta t)$  and  $F_2(\Delta t)$

$$\mathcal{F}_\pm(\Delta t) = F_1(\Delta t) \pm \sin 2\beta F_2(\Delta t) \quad (47)$$

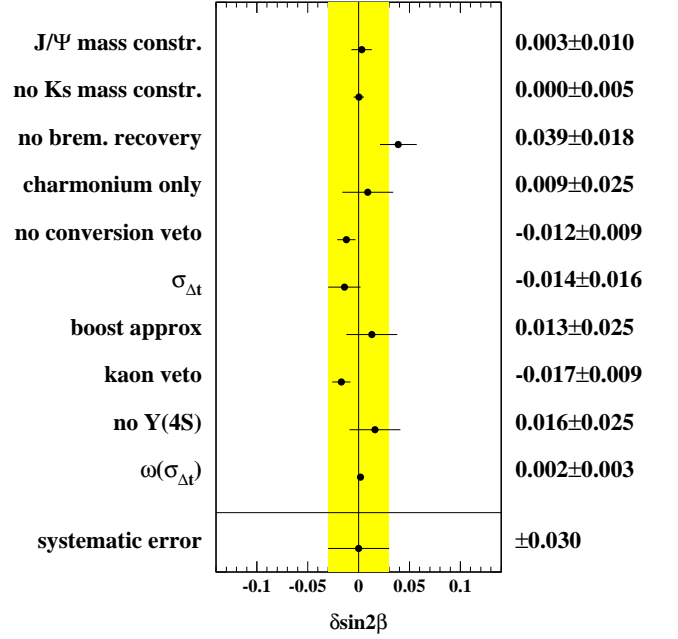


FIG. 32: Results obtained with several alternative variations on the vertexing algorithm that impact the  $\Delta t$  measurement. The shaded band is the systematic error assigned to the parameterization of the resolution function. The full range corresponds to one statistical standard deviation.

allows us to introduce

$$\mathcal{K}(\Delta t) = \pm F_2(\Delta t)/F_1(\Delta t), \quad (48)$$

where + applies to events with a  $B^0$  tag and - with a  $\bar{B}^0$  tag. Ignoring resolution effects, dilutions and background, the Standard Model expectation for the  $\Delta t$  distribution of tagged  $B^0$  decays into  $CP$  modes (Eq. 9) gives  $\mathcal{K}(\Delta t) = -\eta_{CP} \sin \Delta m_d \Delta t$ . When these effects are included, we can still write

$$\mathcal{F}_\pm(\Delta t) = F_1(\Delta t)(1 + \mathcal{K}(\Delta t) \sin 2\beta), \quad (49)$$

although  $\mathcal{K}$  will be a more complicated function of  $\Delta t$  and could depend on kinematic variables as well.

The distribution of events as a function of  $\mathcal{K}$  is

$$\begin{aligned} \frac{dN}{d\mathcal{K}} &= \int d\Delta t \left[ \mathcal{F}_+ \delta \left( \mathcal{K} - \frac{F_2}{F_1} \right) + \mathcal{F}_- \delta \left( \mathcal{K} + \frac{F_2}{F_1} \right) \right] \\ &= (1 + \mathcal{K} \sin 2\beta) \int d\Delta t \times \\ &\quad F_1 \left[ \delta \left( \mathcal{K} - \frac{F_2}{F_1} \right) + \delta \left( \mathcal{K} + \frac{F_2}{F_1} \right) \right] \\ &= (1 + \mathcal{K} \sin 2\beta) \Psi(\mathcal{K}), \end{aligned} \quad (50)$$

where  $\Psi(\mathcal{K})$  is an even function of  $\mathcal{K}$ . It follows that the ratio of the odd to the even part of the distribution for  $\mathcal{K}$  is a linear function of  $\mathcal{K}$  with coefficient  $\sin 2\beta$ . Thus, the distribution of  $\mathcal{K}$  can be used to test for the effect of

an  $CP$  violation simply by examining the dependence of the asymmetry

$$\mathcal{A}(\mathcal{K}) = \frac{dN_{\mathcal{K}>0}/d\mathcal{K} - dN_{\mathcal{K}<0}/d\mathcal{K}}{dN_{\mathcal{K}>0}/d\mathcal{K} + dN_{\mathcal{K}<0}/d\mathcal{K}}. \quad (51)$$

The observed asymmetry for the  $CP$  sample is shown in Fig. 33 as a function of  $\mathcal{K}$ , along with an overlay of the expected linear dependence. The data agree with this hypothesis at the 55% C.L.

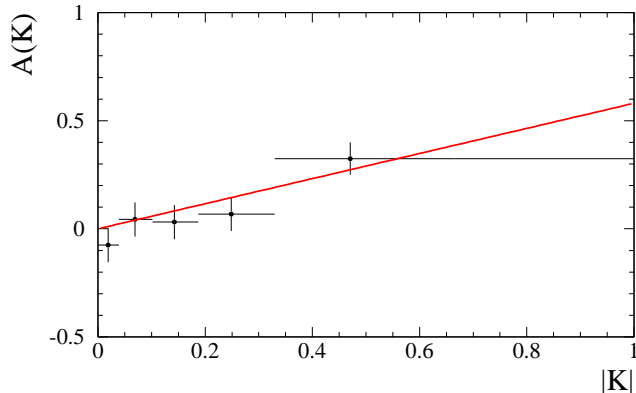


FIG. 33: Observed asymmetry  $\mathcal{A}(\mathcal{K})$  as a function of  $|\mathcal{K}|$ , with an overlay of the expected linear dependence superimposed.

From the expression in Eq. 50 we find

$$\sin 2\beta = \frac{\sum_i \mathcal{K}_i}{\sum_i \mathcal{K}_i^2} \pm \frac{1}{\sqrt{\sum_i \mathcal{K}_i^2}} \sqrt{1 - (\sin 2\beta)^2 \frac{\sum_i \mathcal{K}_i^4}{\sum_i \mathcal{K}_i^2}} \quad (52)$$

In averaging  $\mathcal{K}$  the even component of the  $\Psi(\mathcal{K})$  cancels out, while the odd component cancels in averaging  $\mathcal{K}^2$ . This offers a method of measuring  $\sin 2\beta$  that is mathematically equivalent to the result with the global likelihood fit. However, it can only be applied when  $\sin 2\beta$  is the one remaining free parameter. The moments of  $\mathcal{K}$  for the full  $CP$  sample give results that are numerically identical to the likelihood fit, thereby confirming the minimization procedure used for the fit.

The fact that the mean value of  $\mathcal{K}$  is proportional to  $\sin 2\beta$  also allows a visual representation of the  $CP$  asymmetry. Fig. 34 shows the distribution of  $\mathcal{K}$  in data, with events in the individual tagging categories indicated as well. The larger the value of  $\mathcal{K}$  for a given event, the larger the weight that this event carries in the measurement of  $\sin 2\beta$ . Again, the  $CP$  asymmetry in the data is clearly evident in the distribution of  $\mathcal{K}$ .

#### D. Fits results without assuming $|\lambda| = 1$

A more general description of the time evolution of neutral  $B$  decays to  $CP$  eigenstates contains a term proportional to  $\cos \Delta m_d \Delta t$  (Eq. 7). The coefficient of the

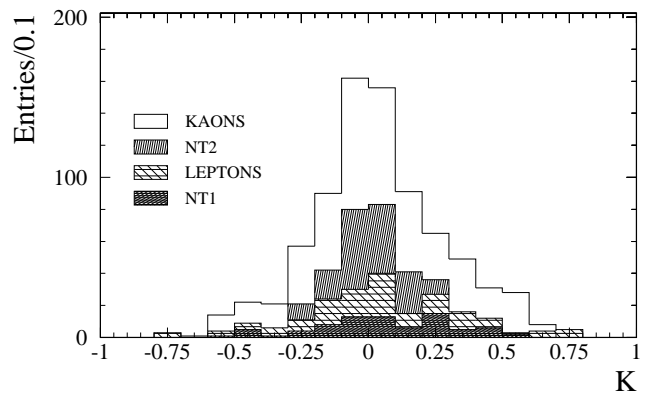


FIG. 34: Distribution of the observable  $\mathcal{K}$  for the individual tagging categories.

cosine term is expected to be negligible in the Standard Model, where  $|\lambda| = 1$ . In order to search for a non-Standard Model effect, we fit the  $\eta_{CP} = -1$  sample for  $|\lambda|$  and  $Im\lambda/|\lambda|$ . The latter is equal to  $\sin 2\beta$  if  $|\lambda| = 1$ . The  $\eta_{CP} = -1$  sample has the advantage of having very little background, while the other  $CP$  modes have backgrounds that are both significantly larger and dominated by other  $B$  decay modes with possible direct  $CP$  contributions.

The fitted values for  $|\lambda|$  and  $Im\lambda/|\lambda|$  with the  $CP = -1$  sample and various subsamples are listed in Table XVII. The two  $CP$  parameters are almost uncorrelated, with the coefficient between  $Im\lambda/|\lambda|$  and  $|\lambda|$  of  $-1.7\%$ . The same systematic error studies as described in detail in Section VIII B were repeated for the fit to the  $\eta_{CP} = -1$  sample for  $Im\lambda/|\lambda|$  and  $|\lambda|$ . The estimated uncertainties from these sources are listed in Table XIX.

We have also performed detailed cross checks, similar to those described in Section VIII C. In particular, large samples of parameterized simulation, as well as full Monte Carlo samples, have been used to verify the fitting procedure. The  $B_{flav}$  sample has also been used to demonstrate that no bias is introduced in the measurement. The relative normalization of the tagged events in the two flavors is in fact sensitive to the coefficient of the cosine term in Eq. 7, and therefore  $|\lambda|$ . The systematic error introduced by the uncertainty on the parameters  $\langle \epsilon_{tag} \rangle_i$  and  $\mu_i$  listed in Table X are uncorrelated between tagging categories. Therefore, they are added in quadrature to obtain the systematic error contribution listed in Table XIX(g).

The final result of the fit with the  $\eta_{CP} = -1$  sample is:

$$|\lambda| = 0.93 \pm 0.09 \pm 0.02 \quad \text{and} \\ Im\lambda/|\lambda| = 0.56 \pm 0.15 \pm 0.05. \quad (53)$$

Thus, we find no evidence for direct  $CP$  violation in the  $\eta_{CP} = -1$  sample and the value of  $Im\lambda/|\lambda|$  is consistent with the result from the nominal  $CP$  fit with  $|\lambda| = 1$ .

## IX. CONCLUSIONS AND PROSPECTS

In  $29.7\text{fb}^{-1}$  of  $e^+e^-$  annihilation data collected near the  $\Upsilon(4S)$  resonance, we have obtained a new measurement of the time-dependent  $B^0$ - $\bar{B}^0$  oscillation frequency with a sample of 6350 tagged flavor-eigenstate  $B^0$  meson decays that are fully-reconstructed in hadronic final states:

$$\Delta m_d = 0.516 \pm 0.016 (\text{stat}) \pm 0.010 (\text{syst}) \text{ ps}^{-1}.$$

This result is at a level of precision comparable to the most recent world average for  $\Delta m_d$  and lies about  $1.7\sigma$  above the combined value of  $0.472 \pm 0.017 \text{ ps}^{-1}$  [11]. It is also quite compatible with our own recent measurement [28] with a dilepton sample. The  $\Delta m_d$  study reported here confirms our understanding of  $B$  reconstruction, flavor tagging, and  $\Delta t$  resolution in our data sample. Our measurement contributes significantly to the precision of the determined value for  $\Delta m_d$ , one of the fundamental parameters constraining our knowledge of the CKM matrix, and remains dominated by statistical errors that will improve with more data.

We have presented a measurement of the  $CP$ -violating asymmetry parameter  $\sin 2\beta$  in the neutral  $B$  meson system:

$$\sin 2\beta = 0.59 \pm 0.14 (\text{stat}) \pm 0.05 (\text{syst}), \quad (54)$$

which establishes  $CP$  violation in the  $B^0$  system at the  $4.1\sigma$  level. This significance is computed from the sum in quadrature of the statistical and additive systematic errors. The probability of obtaining the observed value or higher in the absence of  $CP$  violation is less than  $3 \times 10^{-5}$ . The corresponding probability for the  $\eta_{CP} = -1$  sample alone is  $2 \times 10^{-4}$ . Our measurement is consistent at the  $1.9\sigma$  level with the recently reported result from Belle of  $\sin 2\beta = 0.99 \pm 0.14 (\text{stat}) \pm 0.06 (\text{syst})$  [29], and with previous measurements [30]. The observed value for  $\sin 2\beta$  is currently limited by the size of the  $CP$  sample, allowing for substantial improvement as more data is recorded in the next few years.

We have also used the  $\eta_{CP} = -1$  sample to search for possible direct  $CP$  violation through interference of decay amplitudes. The direct  $CP$  parameter  $\lambda$  is found to be:

$$|\lambda| = 0.93 \pm 0.09 (\text{stat}) \pm 0.02 (\text{syst}).$$

This result is consistent with the Standard Model expectation, where  $|\lambda| = 1$  and no significant direct  $CP$  violation should exist in charmonium decays.

As already noted in Section I, measurements of  $CP$  asymmetries in  $B$  decays to charmonium can be used to constrain, with little theoretical ambiguity, the parameters of the CKM matrix. In the Standard Model with three families, the CKM matrix  $V$  [3] incorporates three real parameters and one phase  $\delta$  generating  $CP$  violation if  $\delta \neq 0$  or  $\pi$ . The Wolfenstein parameterization [14] of  $V$  takes advantage of the observed hierarchy

in the matrix elements in terms of the expansion parameter  $\lambda_{CKM} = |V_{us}|$ . The remaining parameters in this representation are denoted  $A$ ,  $\rho$ , and  $\eta$ , where  $CP$  violation requires  $\eta \neq 0$ .

The parameter  $\lambda_{CKM}$  is determined from semileptonic kaon decays and nuclear  $\beta$  decays. Semileptonic  $B$  meson decays to charm are used to determine the parameter  $A$ . Constraints on  $\rho$  and  $\eta$  are obtained from  $CP$  violation in mixing in the kaon sector  $|\epsilon_K|$ , the ratio  $|V_{ub}/V_{cb}|$ , and the oscillation frequency  $\Delta m_d$  for  $B^0$ - $\bar{B}^0$  mixing. The oscillation frequency  $\Delta m_s$  has not been measured, since  $B_s^0$ - $\bar{B}_s^0$  mixing has not been observed yet. However, the observed amplitude spectrum  $\mathcal{A}(\Delta m_s)$  improves the constraints on  $\rho$  and  $\eta$ . Together, these measurements provide indirect constraints on  $\sin 2\beta$ .

Our overall knowledge of the CKM parameters is limited by the relatively large uncertainties in some of the theoretical quantities, mainly due to non-perturbative QCD effects. In particular, the constraints on  $\rho$  and  $\eta$  suffer from theoretical and systematic uncertainties in the determination of  $|V_{ub}/V_{cb}|$  and from theoretical uncertainties in QCD parameters entering the prediction of  $|\epsilon_K|$ ,  $\Delta m_d$ , and  $\Delta m_s$ . Recent analyses constraining the CKM matrix have been performed with different statistical approaches [34, 35, 36, 37, 38, 39, 40]. They mainly differ in the treatment of theoretical uncertainties and also in the choice of the input values and their errors.

Due to the four-fold ambiguity in the value of  $\beta$  obtained from the  $\sin 2\beta$  measurement, there are four allowed regions in the  $\rho$ - $\eta$  plane. One of these regions is found to be in agreement with the allowed  $\rho$ - $\eta$  region obtained from CKM fits within the Standard Model. Figure 35, taken from Ref. [34], shows our direct measurement and the indirect constraints in the  $\bar{\rho} - \bar{\eta}$  plane in terms of the renormalized parameters  $\bar{\rho} = \rho(1 - \lambda_{CKM}^2/2)$  and  $\bar{\eta} = \eta(1 - \lambda_{CKM}^2/2)$ . The contributions of the individual measurements  $|\epsilon_K|$ ,  $|V_{ub}/V_{cb}|$ ,  $\Delta m_d$ , and  $\Delta m_s$  [34] are indicated, as well as the allowed region if all the constraints are considered simultaneously. Overlaid as the diagonally-hatched area are the regions corresponding to one and two times the one-standard-deviation experimental uncertainty on our  $\sin 2\beta$  measurement.

It should be emphasized that, beyond being a direct constraint on  $\beta$ , the measurement of  $\sin 2\beta$  differs qualitatively in its interpretation from the indirect constraints on  $\beta$  obtained from  $|\epsilon_K|$ ,  $|V_{ub}/V_{cb}|$ ,  $\Delta m_d$ , and eventually  $\Delta m_s$ . For  $\sin 2\beta$ , the size of the allowed domain is determined by well-defined experimental uncertainties that are predominantly statistical in origin, while in contrast the region allowed by the indirect measurements is mostly defined by theoretical uncertainties, which makes a statistical interpretation difficult.

The current experimental uncertainty on  $\sin 2\beta$  has now reached a level of precision that offers significant constraint on the Standard Model. Over the next few years there will continue to be substantial improvements in precision of the  $\sin 2\beta$  determination, including measurements for other final states in which  $CP$ -violating



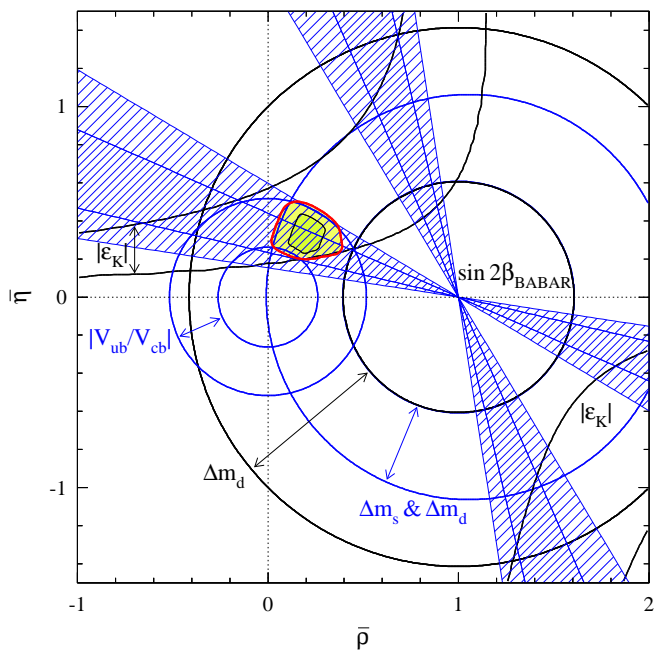


FIG. 35: Present indirect constraints on the position of the apex of the Unitarity Triangle in the  $(\bar{\rho}, \bar{\eta})$  plane, not including our measurement of  $\sin 2\beta$ . The fitting procedure is described in Ref [34]. Our result  $\sin 2\beta = 0.59 \pm 0.14$  (stat)  $\pm 0.05$  (syst) is represented by diagonally hatched regions, corresponding to one and two statistical standard deviations. The individual indirect constraints lie between the pairs of solid lines that are connected by the double-ended arrows with labels.

asymmetries are proportional to  $\sin 2\beta$ . Beyond this,

studies of time-dependent asymmetries in modes involving  $b \rightarrow u$  transitions have already begun [41] and may provide additional constraints, although here the interpretation in terms of  $\sin 2\alpha$  from the Unitarity Triangle is likely to be made difficult due to significant penguin contributions. Nevertheless, these measurements will be able to directly test the validity of the CKM picture as the origin for the observed  $CP$  violation in neutral  $B$  decays.

## X. ACKNOWLEDGMENTS

We are grateful for the extraordinary contributions of our PEP-II colleagues in achieving the excellent luminosity and machine conditions that have made this work possible. The collaborating institutions wish to thank SLAC for its support and the kind hospitality extended to them. This work is supported by the US Department of Energy and National Science Foundation, the Natural Sciences and Engineering Research Council (Canada), Institute of High Energy Physics (China), the Commissariat à l’Energie Atomique and Institut National de Physique Nucléaire et de Physique des Particules (France), the Bundesministerium für Bildung und Forschung (Germany), the Istituto Nazionale di Fisica Nucleare (Italy), the Research Council of Norway, the Ministry of Science and Technology of the Russian Federation, and the Particle Physics and Astronomy Research Council (United Kingdom). Individuals have received support from the Swiss National Science Foundation, the A. P. Sloan Foundation, the Research Corporation, and the Alexander von Humboldt Foundation.

- 
- [1] J.H. Christenson *et al.*, Phys. Rev. Lett. **13**, 138 (1964); NA31 Collaboration, G.D. Barr *et al.*, Phys. Lett. **317**, 233 (1993); E731 Collaboration, L.K. Gibbons *et al.*, Phys. Rev. Lett. **70**, 1203 (1993).
- [2] A.D. Sakhorov, Pisma Zh. Eksp. Teor. Fiz. **5**, 32 (1967); Translation JETP Lett. **5**, 24 (1967).
- [3] N. Cabibbo, Phys. Rev. Lett. **10**, 531 (1963); M. Kobayashi and T. Maskawa, Prog. Th. Phys. **49**, 652 (1973).
- [4] See, for instance, “Overall determinations of the CKM matrix”, Section 14 in “The BABAR physics book”, P. H. Harrison and H. R. Quinn, eds., SLAC-R-504 (1998), and references therein.
- [5] For an introduction to  $CP$  violation, see, for instance, “A  $CP$  violation primer”, Section 1 in “The BABAR physics book”, op. cit. [5], and references therein.
- [6] M.B. Gavela *et al.*, Mod. Phys. Lett. **A9**, 795 (1994) and Nucl. Phys. **B340**, 382 (1994); P. Huet and E. Sather, Phys. Rev. **D51**, 379 (1995).
- [7] C. Jarlskog, in *CP Violation*, C. Jarlskog ed., World Scientific, Singapore (1988).
- [8] “PEP-II: An Asymmetric  $B$  Factory”, Conceptual Design Report, SLAC-418, LBL-5379 (1993).
- [9] UA1 Collaboration, C. Albajar *et al.*, Phys. Lett. **B186**, 247 (1987).
- [10] ARGUS Collaboration, H. Albrecht *et al.*, Phys. Lett. **B192**, 245 (1987).
- [11] Particle Data Group, D. E. Groom *et al.*, Eur. Phys. Jour. C **15**, 1 (2000).
- [12] Throughout this paper, charged and neutral flavor-eigenstate decay modes imply also their charge conjugate.
- [13] BABAR Collaboration, B. Aubert *et al.*, Phys. Rev. Lett. **87**, 241801 (2001).
- [14] L. Wolfenstein, Phys. Rev. Lett. **51**, 1945 (1983).
- [15] BABAR Collaboration, B. Aubert *et al.* “Measurement of  $B^0 \bar{B}^0$ -flavor oscillations in hadronic  $B^0$  decays”, BABAR-PUB-01/02, SLAC-PUB-9061, hep-ex/0112044, submitted to Phys. Rev. Lett.
- [16] BABAR Collaboration, B. Aubert *et al.* Phys. Rev. Lett. **87**, 091801 (2001); Phys. Rev. Lett. **86**, 2515 (2001).
- [17] BABAR Collaboration, B. Aubert *et al.*, Phys. Rev. Lett. **87**, 201803 (2001).
- [18] BABAR Collaboration, B. Aubert *et al.*, “The BABAR

- detector”, *BABAR*-PUB-01/08, SLAC-PUB-8569, hep-ex/0105044, to appear in Nucl. Instr. and Methods **A**.
- [19] P. Billoir, Nucl. Instr. and Methods **A 225**, 225 (1984).
- [20] A. Drescher *et al.*, Nucl. Instr. and Methods **A237**, 464 (1985).
- [21] R. Sinkus and T. Voss, Nucl. Instr. and Methods **A 391**, 360 (1997).
- [22] G.C. Fox and S. Wolfram, Phys. Rev. Lett. **41**, 1581 (1978).
- [23] ARGUS Collaboration, H. Albrecht *et al.*, Phys. Lett. **B241**, 278 (1990).
- [24] *BABAR* Collaboration, B. Aubert *et al.*, “Measurement of branching fractions for exclusive  $B$  decays to charmonium final states”, *BABAR*-PUB-01/07, SLAC-PUB-8909, hep-ex/0107025, to appear in Phys. Rev. **D**.
- [25] The Crystal Ball function is given by
- $$f(x) = N \cdot \begin{cases} \exp\left(-\frac{(x-\bar{x})^2}{2\sigma^2}\right) & ; (x-\bar{x})/\sigma > \alpha \\ A \times \left(B - \frac{x-\bar{x}}{\sigma}\right)^{-n} & ; (x-\bar{x})/\sigma \leq \alpha \end{cases}$$
- where  $A \equiv \left(\frac{n}{|\alpha|}\right)^n \times \exp(-|\alpha|^2/2)$  and  $B \equiv \frac{n}{|\alpha|} - |\alpha|$ .  $N$  is a normalization factor,  $\bar{x}$  and  $\sigma$  are the fitted peak position and width of the Gaussian portion of the function, and  $\alpha$  and  $n$  are the fitted point at which the function transitions to the power function and the exponent of the power function, respectively. D. Antreasyan, Crystal Ball Note 321 (1983).
- [26] E687 Collaboration, P. L. Frabetti *et al.*, Phys. Lett. **B331**, 217 (1994).
- [27] “GEANT, Detector Description and Simulation Tool”, CERN program library long writeup W5013 (1994).
- [28] *BABAR* Collaboration, B. Aubert *et al.*, “Measurement of the  $B^0$ - $\bar{B}^0$  oscillation frequency with inclusive dilepton events”, *BABAR*-PUB-01/23, SLAC-PUB-9061, hep-ex/0112045, submitted to Phys. Rev. Lett. Both are somewhat higher, but consistent with, a recent dilepton result from the Belle Collaboration, K. Abe *et al.*, Phys. Rev. Lett. **86**, 3228 (2001).
- [29] Belle Collaboration, K. Abe *et al.*, Phys. Rev. Lett. **87**, 091802 (2001).
- [30] Other results have been reported by OPAL [31] ( $\sin 2\beta = 3.2_{-2.0}^{+1.8} \pm 0.5$ ) and CDF [32] ( $\sin 2\beta = 0.79_{-0.44}^{+0.41}$ ). See also ALEPH’s preliminary result [33]  $\sin 2\beta = 0.93_{-0.88}^{+0.64} +0.36_{-0.24}$ .
- [31] OPAL Collaboration, K. Ackerstaff *et al.*, Eur. Phys. Jour. C **5**, 379 (1998).
- [32] CDF Collaboration, T. Affolder *et al.*, Phys. Rev. **D61**, 072005 (2000).
- [33] ALEPH Collaboration, ALEPH 99-099 CONF 99-54 (1999).
- [34] A. Höcker, H. Lacker, S. Laplace and F. Le Diberder, Eur. Phys. Jour. C **21**, 225 (2001).
- [35] S. Plaszczynski, M.-H. Schune, “Overall determination of the CKM matrix,” LAL-99-67, hep-ph/9911280; “*BABAR* physics book,” Chapter 14, SLAC-R-504, 1998.
- [36] M. Ciuchini *et al.*, JHEP 0107:013 (2001).
- [37] M. Bargiotti *et al.*, Riv. Nuovo Cim. **23N3**, 1 (2000).
- [38] P. Faccioli, Nucl. Instr. and Methods **A 462**, 313 (2001).
- [39] D. Atwood and A. Soni, Phys. Lett. **B516**, 39 (2001).
- [40] A. Ali and D. London, Eur. Phys. Jour. C **18**, 665 (2001).
- [41] *BABAR* Collaboration, B. Aubert *et al.*, “Study of  $CP$ -violating asymmetries in  $B^0 \rightarrow \pi^+\pi^-$ ,  $K^+\pi^-$  decays”, *BABAR*-PUB-01/21, SLAC-PUB-9012, hep-ex/0110062, to appear in Phys. Rev. **D**.